UNIVERSITY OF OKLAHOMA

GRADUATE COLLEGE

EVALUATION OF 3D SEISMIC ATTRIBUTES AND POST STACK INVERSION METHODS: PENNSYLVANIAN GRANITE WASH RESERVOIR CHARACTERIZATION CASE STUDY, TEXAS

A THESIS

SUBMITTED TO THE GRADUATE FACULTY

in partial fulfillment of the requirements for the

Degree of

MASTER OF SCIENCE

By

ANA MARIELA MARTINS BATISTA
Norman, Oklahoma
2010

EVALUATION OF 3D SEISMIC ATTRIBUTES AND POST STACK INVERSION METHODS: PENNSYLVANIAN GRANITE WASH RESERVOIR CHARACTERIZATION CASE STUDY, TEXAS

A THESIS APPROVED FOR THE
CONOCO PHILLIPS SCHOOL OF GEOLOGY AND GEOPHYSICS

BY

Dr. Kurt Marfurt, Chair

Dr. Roger Slatt

Dr. J. Tim Kwiatkowski

ACKNOWLEDGEMENTS

I would like to thank my advisor Dr Kurt Marfurt for all his guidance and suggestions throughout this research and the numerous projects that we worked together. Special thanks to the thesis committee members Dr. Roger Slatt and Dr. J. Tim Kwiatkowski for their revisions and advice. I would also like to thank TameCat, especially Michael Burnett, for providing the survey used in this project.

I would like to thank Schlumberger Limited, for all the economical support and this big opportunity that the company gave me when they decided to send me to University of Oklahoma. Especially thanks to Bob Davis for his support during my Masters.

To all my friends that accompanied me through this time here in Norman, Oklahoma. Special thank to my family for all their support and their love. Finally, I would like to thanks my husband, Leonardo for his comprehension, patience, friendship and most important his love all these years with me.

TABLE OF CONTENTS

TABLE OF FIGURES

ABSTRACT

Seismic attributes and seismic inversion have become important for the determination of static reservoir properties. This study evaluates these methods trough a case study on a formation that has traditionally been difficult to characterize seismically, the Pennsylvanian Granite Wash of the Dalhart basin, Texas.

The seismic survey is one of the fisrt 3D land surveys acquired in the Texas panhandle during the early 1990s. As such it suffers from migration aliasing, strong acquisition footprint and relatively low vertical resolution. Subsequent passes of kx - ky footprint suppression followed by structure-oriented filtering significantly increased the signal-to-noise ratio of the data.

Coherent energy gradient, coherent energy, most positive and most negative curvature and Sobel filter similarity computed from post-stack seismic data delineated the Granite Wash deposit in the study area. Acoustic impedance computed from the seismic amplitude volume integrated with the sonic and density logs provided good images of reservoir heterogeneity. Previous wells are all drilled on the up-thrown block of a reverse fault system. Acoustic impedance indicates similar reservoir rock exists in the untested down-thrown block.

CHAPTER I

INTRODUCTION

General

Alluvial systems generally exhibit complex stratigraphy, such as the, complex reservoirs of the Pennsylvanian Granite Wash found in the subsurface of Oklahoma and Texas, which have been interpreted as fan delta complexes.

Dutton (1982) was one of the first workers to publish her study of the Granite Wash, reporting on the sedimentology and stratigraphy of the interbedded coarse grain sandstones and limestones in the Late Pennsylvanian (Missourian) Granite wash, Mobeetie, Field, Texas. Later Dutton and Goldstein (1989) discussed the Pennsylvanian fan-delta Granite Wash deposits as part of their larger study of the shelf margin evolution and the depositional system in the Palo Duro Basin, Texas.

Frost et al. (1982) reported on the mineralogy of the Granite Wash and discussed the limitations in a reservoir evaluation of the Granite Wash using the standard Gamma Ray tool versus the newer (at that time) Spectral Gamma Ray tool.

Lyday (1985) studied the structural influences and depositional environment on the Atokan Dolomite Wash, while Hendrickson et al. (2001) introduced the currently accepted nomenclature for the Granite Wash based on basin and mountain front correlations.

Poole (2005) conducted electrofacies, lithofacies and petrographic analysis of data from the Stiles Ranch, Britt Ranch and Elmore field, to depths including the depositional system of the Pennsylvanian Granite Wash located in the Anadarko Basin, Oklahoma and Texas.

In many areas, the Granite Wash formation has been difficult to characterize using seismic data due to limited seismic resolution. Burnett (2002) noted that such limitations impede the generation of an adequate depositional model and potential hydrocarbon reservoir compartments. Valerio (2006) applied spectral decomposition and spectral inversion on a Pennsylvanian Granite Wash, Texas, thereby extracting greater detail at the high end of the seismic spectrum.

In my thesis, I will extend the scientific understanding of the petrophysical and seismic expression of the granite wash as seen in the Granite Wash in Texas and Oklahoma. I will apply this work flow to a somewhat related alluvial system of conglomeratic beds in Chiapas-Tabasco basin in Mexico, where the very hard 'wash' serves as a drilling hazard to be avoided rather than hydrocarbon reservoir to be tapped. Primary tools are log analysis, seismic attributes, and post-stack impedance inversion.

General Objectives

The objective of this study is to evaluate the advantages of 3D seismic attribute technology and post-stack seismic inversion to characterize the Pennsylvanian Granite Wash reservoir located in Hartley Country, Texas.

Specific objectives

The specific objectives of this study are:

- Generate synthetic seismograms for the wells.
- Interpret seismic data generating traditional time-structure and thickness maps as well as attribute maps to aid in reservoir delineation.
- Apply seismic inversion to the 3D seismic data with the goal of mapping porosity and reservoir compartmentalization.
- Evaluate the reservoir within a seismic geomorphology and depositional environment context.

Location

TameCAT, an independent oil and consulting company based in Norman OK, has provided the information for this project. The data consist of a 3D Post-Stack seismic survey acquired in Hartley County (Figure 1.1 and 1.3), that falls within the Dalhart basin in the northwest corner of the Texas panhandle (Figure 1.2). The study area is 10 sq mi, which covers the north part of the Rehm field (Figure 1.4).

Figure 1.1. Location of Hartley County Texas.

(www.Google.com)

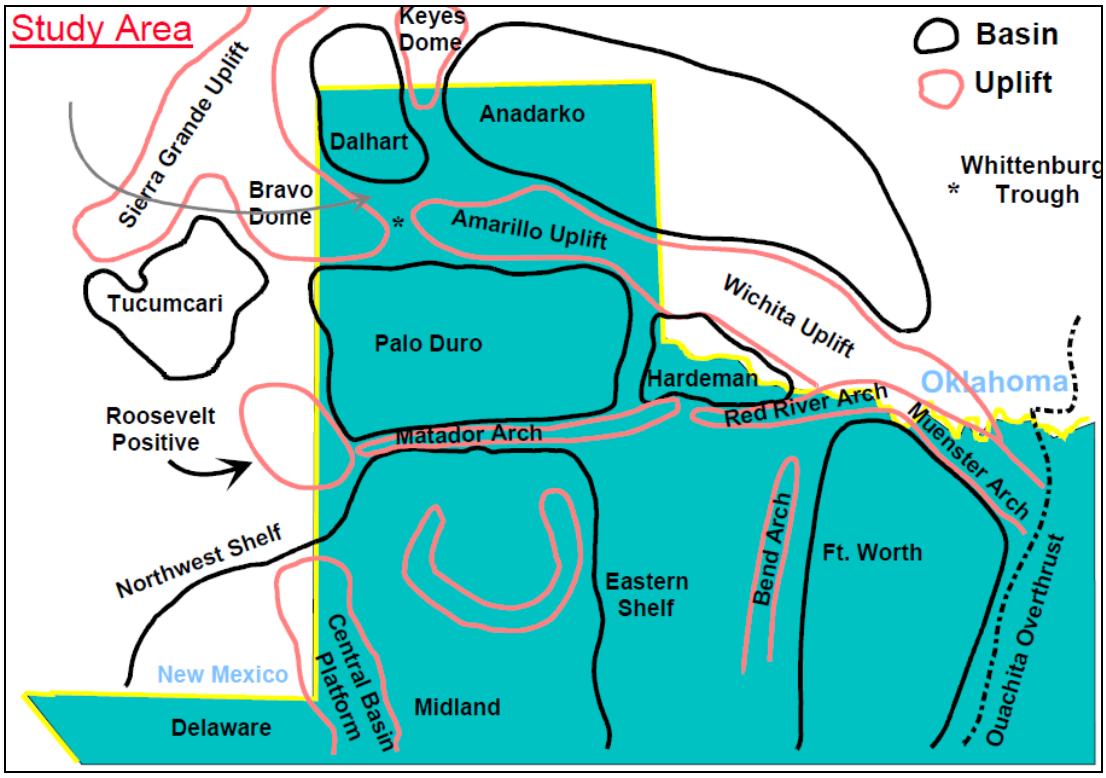

Figure 1.2 Structural features of North Texas.

(After Burnett, 2002). The area under study is located at the southern end of the Dalhart basin and the Whittenburg Trough, which separates the Dalhart basin from Palo Duro Basin.

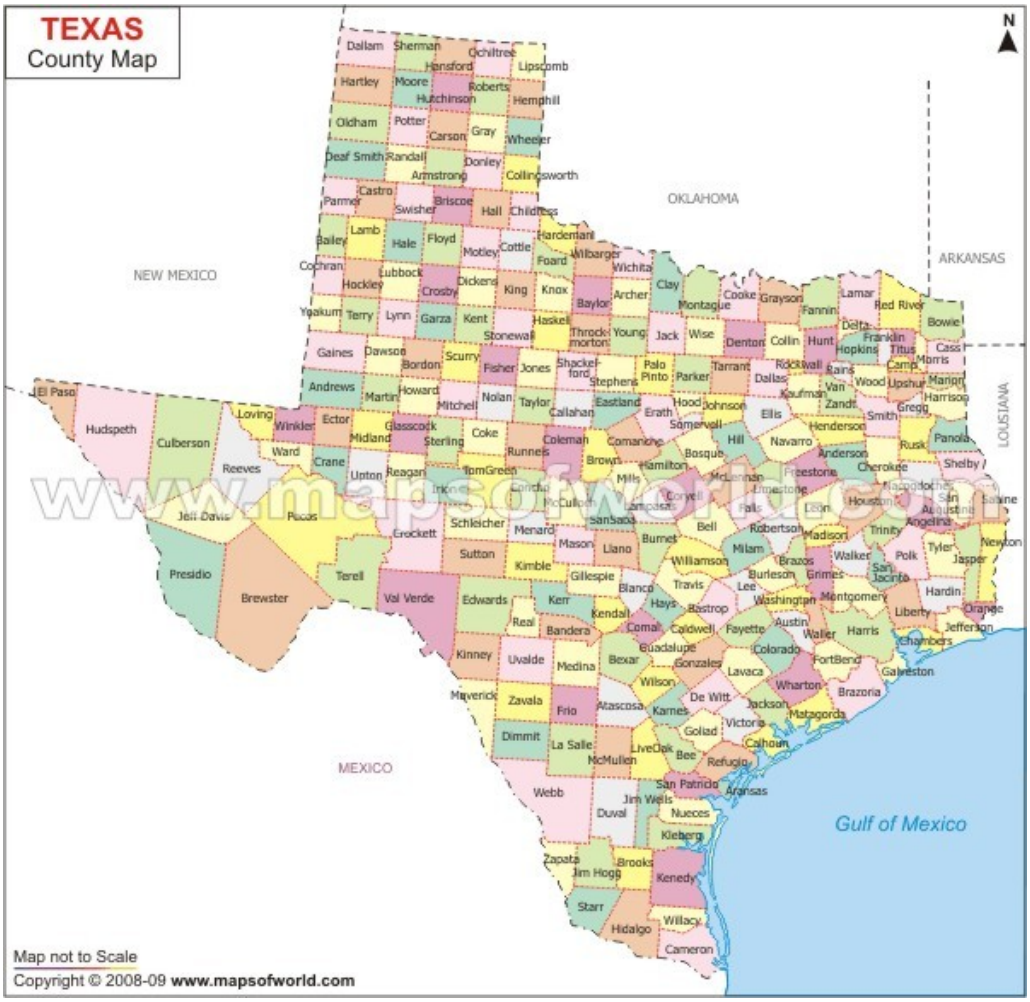

Figure 1.3. Map of Texas Counties.

(www.mapofworld.com)

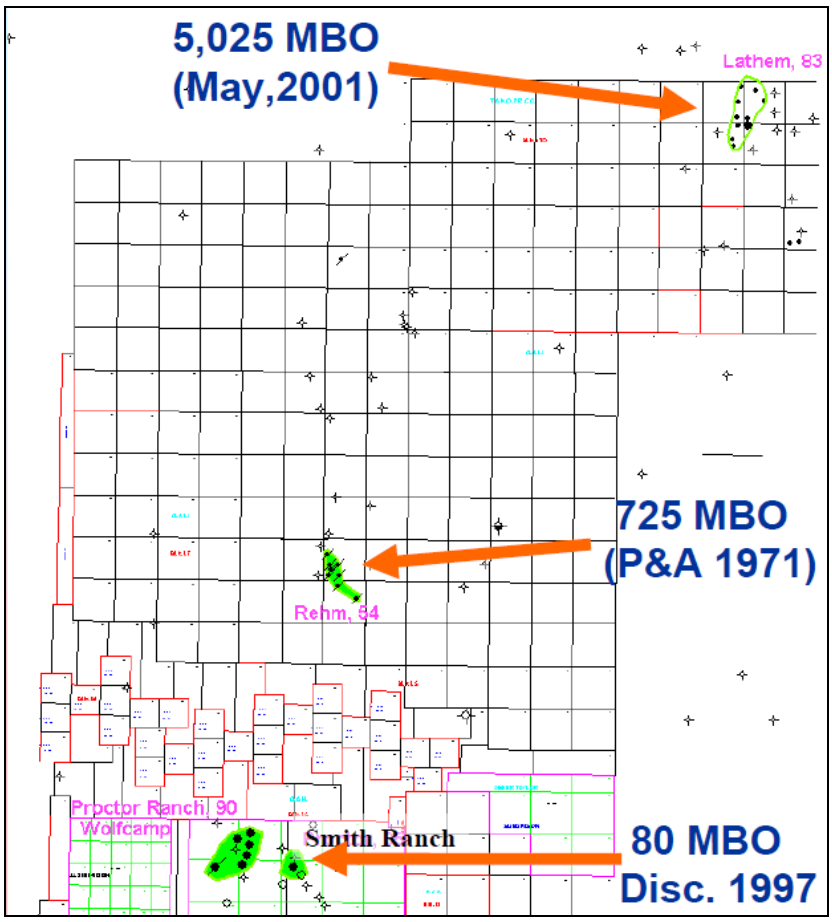

Figure 1.4. The Rehm Field within the Texas Panhandle

(After Burnett, 2002)

In addition to the 3D seismic data the operator provided a suite of logs for 18 wells that fall within the 3D survey area. Four of the wells have deep resistivity (Rt), spontaneous potential (SP), Gamma Ray (GR), density (RHOB) and sonic (DT) logs that are most useful in the well-tie process. (Table 1).

Number of wells	Logs available
13	Resistivity and SP
4	Resistivity, SP, GR, DTCO and Density
1	DTCO

Table 1. Inventory of available well data for this study.

CHAPTER II

TECTONIC AND STRATIGRAPHIC FRAMEWORK

Introduction

The Dalhart basin is located in the Texas panhandle and contains rocks of Precambrian to Quaternary age, but most of the fill is upper Paleozoic (Dutton and Goldstein, 1989). The Dalhart basin was interconnected with the Anadarko basin to the east during most of its geological history. The carbonate are strata genetically related to those of the Palo Duro basin to the South and were deposited during the later Pennsylvanian to early Permian, in the southern portion of the basin (Duncan, 1980).

The stratigraphic chart of Pennsylvanian and Permian strata in the Dalhart and Palo Duro basins made for Dutton in 1989 is show in Figure 2.1.

The rocks of Precambrian age in the Dalhart basin belong principally to two groups: The Panhandle volcanic terrain and the Wichita igneous province. The Panhandle volcanic terrain consists mainly of rhyolite porphyry flows, while the Wichita province consists mainly of granitic intrusive rock. (Duncan, 1980)

The Cambrian consists of the relatively thin Hickory sandstone (Birsa, 1977). The Ordovician system includes the Ellenburger limestone group, the Simpson sandstone group and the Viola Limestone. The Sylvans shale which is present across parts of the Anadarko Basin, is absent in the Dalhart Basin.(Duncan,1980).

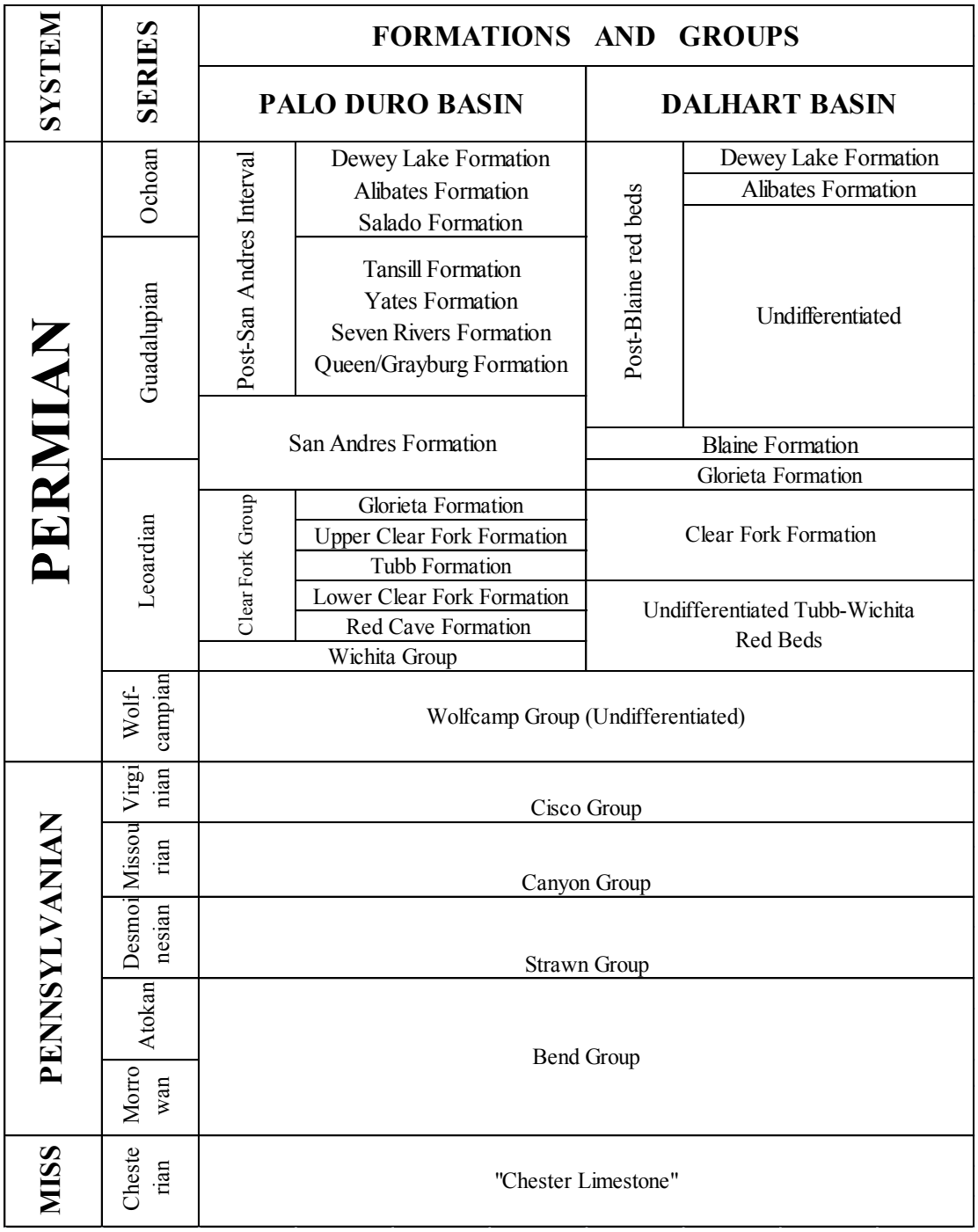

Figure 2.1 Stratigraphic Chart of Permian and Pennsylvanian strata in Dalhart and Palo Duro basins.

(After Dutton and Goldstein, 1989)

The Silurian and the Devonian age rocks are not found in the Dalhart basin, either because of erosion or non-deposition. (Duncan, 1980). In contrast, the Mississippian age strata are well-represented in the majority of the Dalhart basin, except in Oldham County and western Hartley County, by the Kinderhook, Osage, Meramec and Chester Series (Duncan, 1980). The Kinderhook series is described as sandstone interbedded with brown dolomite, the Osage series as a dolomite, the Meramec series as a limestone which is an easily recognized marker throughout the Dalhart basin. Finally the Chester series is described as a limestone (Duncan, 1980).

The Pennsylvanian rocks are present in the Dalhart basin through the sediments of the Morrow, Atoka, Des Moines, Missouri and Virgil series (Duncan, 1980). Sediments of the Morrow series are predominately granite wash and arkosic shale (Cunningham, 1961). The thickness of the Morrow varies from zero on surrounding uplifts to more than 800 feet in northeastern Hartley County. The Atoka series consists of lignitic coal with associated underclay. (Duncan, 1980). The Des Moines series was described as glauconitic and arkosic limestone. The Missouri series appear to be an arkosic limestone and granite wash. Finally the Virgil series consists of limestone and interbedded red shale (Cunningham, 1961).

In the Dalhart Basin, the Permian system is represented by a variety of lithologies, and includes rocks of the Wolfcamp, Leonard and Guadalupe series. Granite wash, sandstone and shale, normal marine limestone, marine to non-marine red beds, massive dolomite, anhydrite and salt are present (Cunningham, 1961).

Unconformably overlying the Permian are upper Triassic sediments, which consists of interbedded shale and sandstones of the Dockum Group. In the Jurassic system the Morrison formation is present and described as interbedded shale and sandstones. (Duncan, 1980).

Tectonic and Stratigraphic Framework

The Anadarko Basin underwent rapid subsidence during the Pennsylvanian as the adjacent Amarillo uplift was elevated. The clastic sediments consisting of Granite Wash, pebbles and boulders were eroded from the Precambriam basement and deposited in the Anadarko Basin in the North of Palo Duro Basin on the south (Fig. 2.2). In the west-central United States during the Pennsylvanian period several similar fault-bounded uplifts and adjacent basins occurred. (Dutton, 1982)

In the late Mississippian and Pennsylvanian time the Amarillo-Wichita, Sierra Grande, Apishapa, Uncompahgre, Frontage and Pedernal uplift were formed. (Dutton, 1984). Thick wedges of coarse-grained, terriginous clastic deposits accumulated along each of the fault-bounded uplifts. The Pennsylvanian and Lower Permian sediments of the Fountain, Maroon, Hermosa-Cutler, and Sangre de Cristo formations in Utah and Colorado are stratigraphic and genetic equivalents of the Granite Wash in the Texas Panhandle (Dutton, 1984)

Fan-delta deposits are recognized in the subsurface by coarse-grained clastic sediments that were deposits adjacent to an elevated source area that interfingers with marine sediments. Contemporaneous faults commonly bound thick, proximal fan-delta

deposits. Therefore, Pennsylvanian and Lower Permian rocks in the west-central United States provide examples of extensive fan-delta deposition in an intracratonic tectonic setting (Dutton, 1984).

Figure 2.2 Structural elements of west-central United States during middle Pennsylvanian (After Dutton, 1984)

The Dalhart basin is an intra-continental basin, which began to develop during Pennsylvanian time. The geologic history and the tectonic development of the basin can be subdivided into four periods: Pre-Pennsylvanian, Pennsylvanian, Permian and Post-Permian. (Duncan, 1980).

Pre-Pennsylvanian

The Dalhart basin is situated in an area considered to be the foreland facies of the Ouachita orogenic belt. The oceanic crust was added to Paleozoic North America as the rifted and attenuated continental margin subsided thermotectonically and retreated from the newly formed spreading ridge (Figure 2.3 a). Plate motion reversed, resulting in plate convergence during the late Ordovician time (Figure 2.3 b). In the Devonian period much of the Panhandle area had been deeply eroded due to a convergence of plates which caused the foreland facies to be uplifted. (Figure 2.3 c). The area subsided and the environment became favorable to carbonate deposition. At the close of this period, the present African plate converged on the North America plate, causing the area to be uplifted and to be exposed to erosion (Figure 2.3 d) (Walper, 1977).

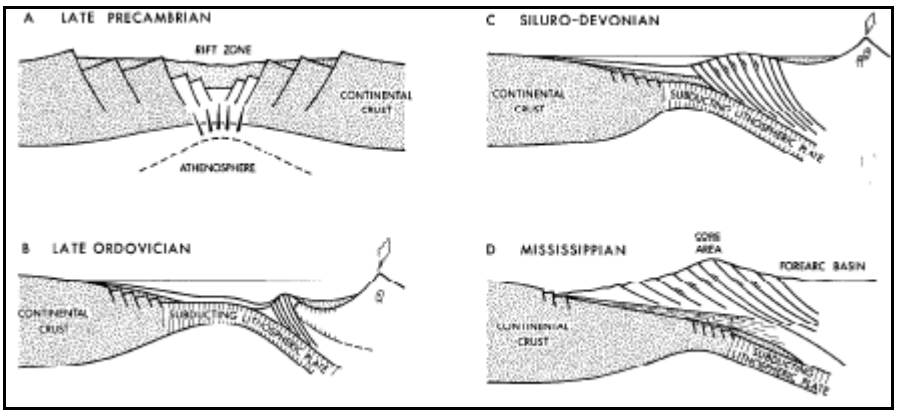

Figure 2.3 Diagrammatic cross section of the tectonic evolution of the Ouachita System (Walper, 1977)

Pennsylvanian

Morrow time saw the initiation of marginal continental and shallow marine deposition. The Amarillo uplift and the Bravo Dome remained sufficiently positive that the Palo Duro Basin avoided inundation by the seas. (Duncan, 1980).

The plate collisions resulted in transcurrent and vertical faulting. Active structural deformation occurred; intense block faulting elevated the Amarillo Uplift and the Bravo Dome. A large quantity of clastic material, mainly Granite Wash, was deposited in continental, shelf and basinal environments. The tectonic activity had ceased at the end of the Pennsylvanian period (Walper, 1977). The seas gradually encroached farther upon the area, and a period of carbonate to clastic cyclicity with, the carbonates sediments dominant were deposited at the end of the Pennsylvanian (Duncan, 1980).

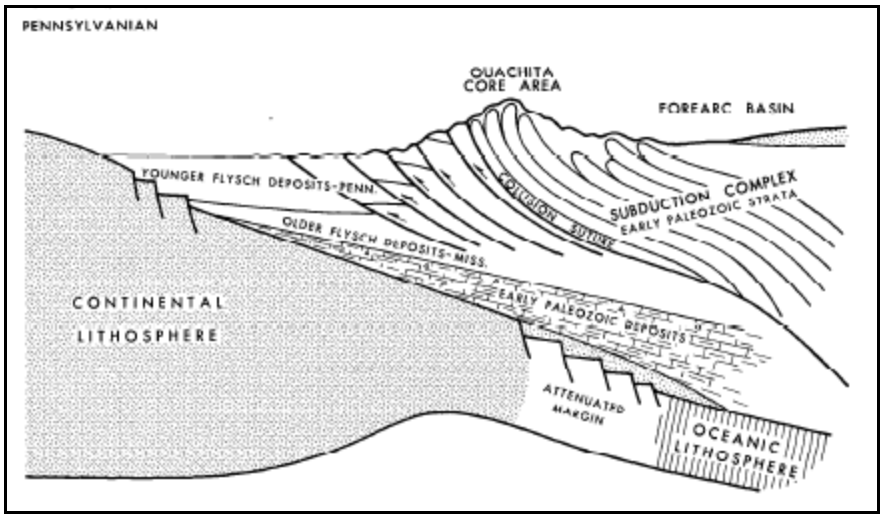

Figure 2.4 Diagrammatic cross section (Pennsylvanian) showing synchronous development of foreland basin fold trust belt and basin sedimentation.
(Walper, 1977)

Permian

During Permian time marine sedimentation continued with the Amarillo uplift and Bravo Dome covered by clastic sediments. The Dalhart, Palo Duro and Anadarko Basins were covered by the sea during the Wolfcampian time, and formed a large evaporites-salt basin. (Eddleman, 1961).

Post-Permian

The sedimentation during the Triassic time was dominated first by meandering river systems and then by the braided alluvial sheets (Asquith, 1975). During Cretaceous time the sediments probably covered the Dalhart basin area, and then late in the Cretaceous the Laramide revolution uplifted and tilted the basin to the east and southeast, the faulting renewed along old planes of weakness (Duncan, 1980).

The Granite Wash formation in the Texas-Oklahoma Panhandle region is Pennsylvanian and early Permian in age and was deposited along the southern edge of the Anadarko basin when the Amarillo-Wichita Mountain horst block was uplifted. Some 30,000 ft (10,000 m) of vertical displacement occurred due to a series of high angle reverse faults along the frontal Wichita fault zone. As the uplifting occurred large volumes of arkosic sediment were carried by braided streams to alluvial fans and fan deltas (Schenewerk,1980). Figure 2.5 shows an isolith of the regional extent and total thickness of Granite Wash in Lower Pennsylvanian through Lower Permian strata.

To the north of Amarillo, a fault in the Anadarko Basin bounds a prism of Granite Wash greater than 5,000 ft thick (1,600 m). (Figure 2.6) The fault displacement is less in the Palo Duro Basin than the Amarillo uplift, such that a much greater thickness of sediments accumulated in the Amarillo uplift. Granite Wash at the north of the uplift is more than five times as thick as it is at south of the uplift (Figure 2.7; Dutton, 1984).

Figures 2.8 and 2.9 depict two east-west cross sections which, showing the stratigraphic framework and depositional systems of Pennsylvanian-Lower Permian strata. The Top of the Wolfcampian series is used as the datum plane in all of the cross sections.

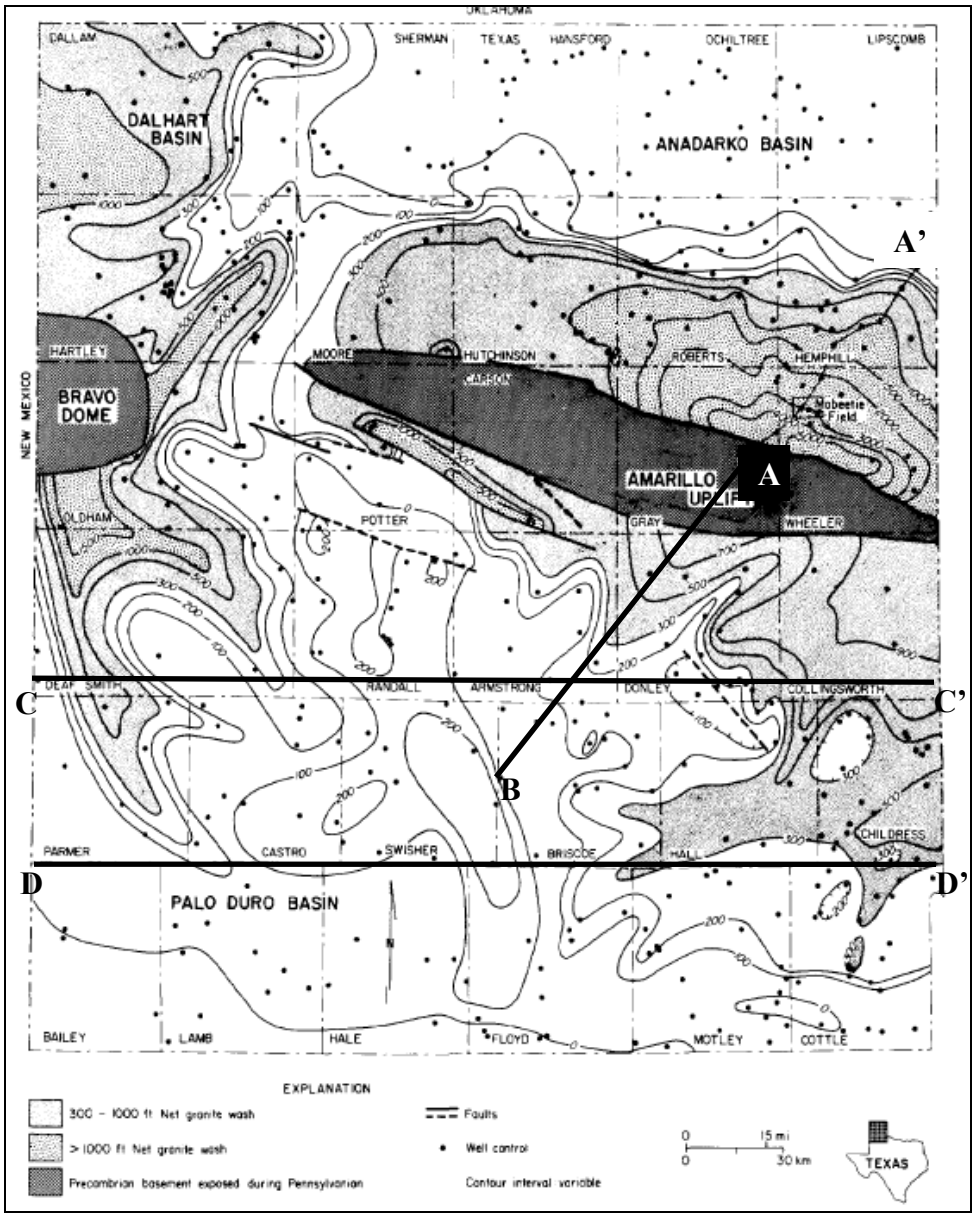

Figure 2.5 Granite-Wash isolith map of Lower Pennsylvanian to Lower Permian strata. (Dutton, 1982).

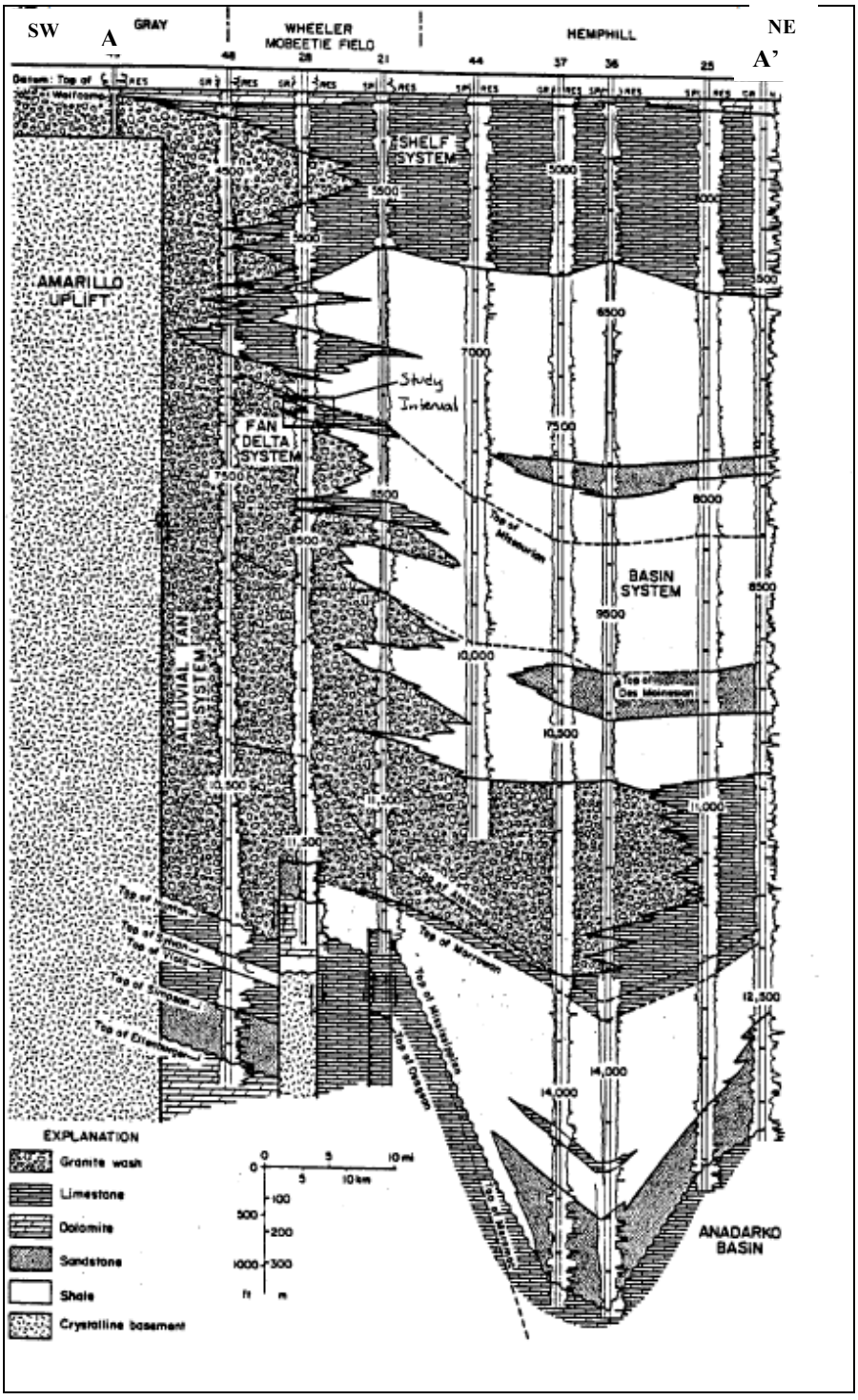

Figure 2.6 North-south regional cross section A-A'. Location of line shown in Figure 2.5 (After Dutton, 1984)

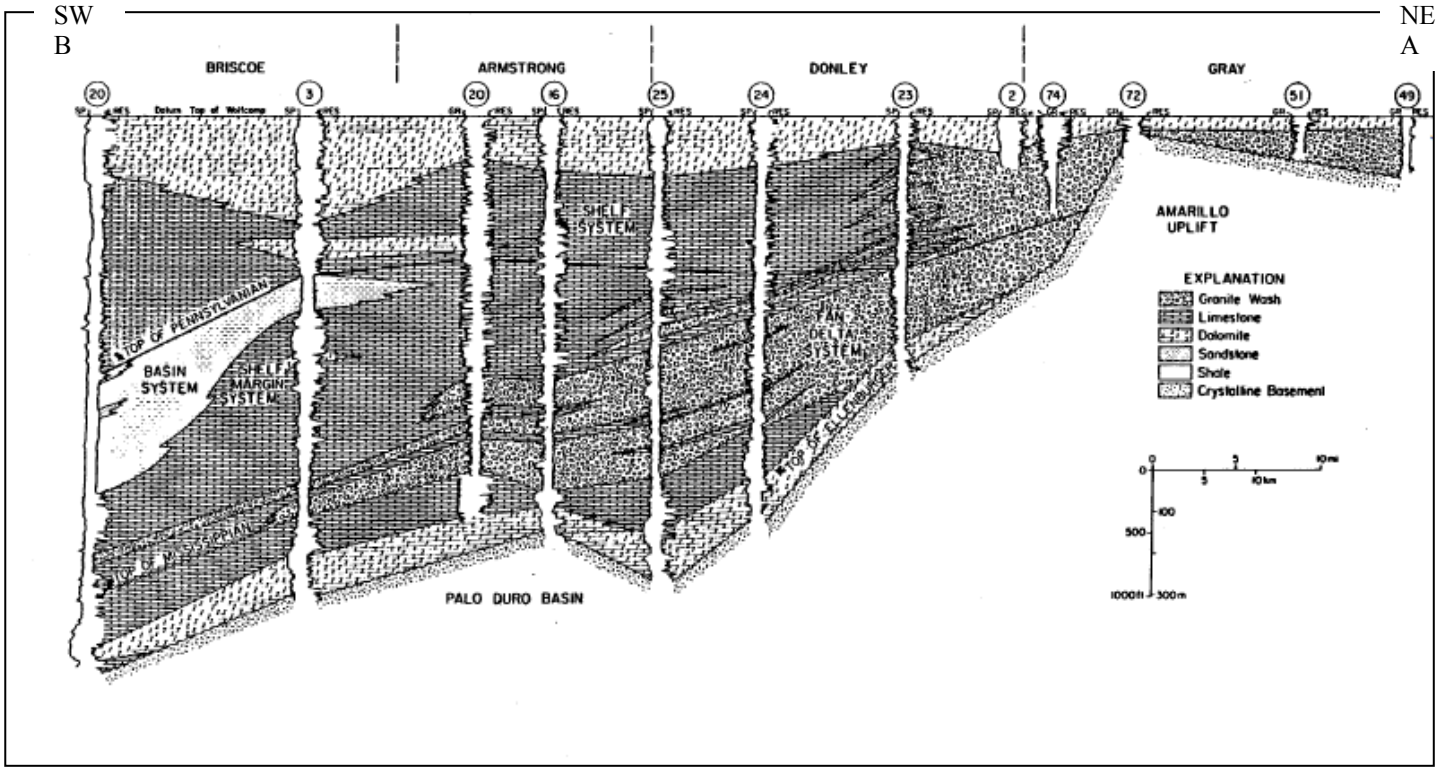

Figure 2.7 North-south regional cross section B-A. Location of line shown in Figure 2.5

(After Dutton, 1984)

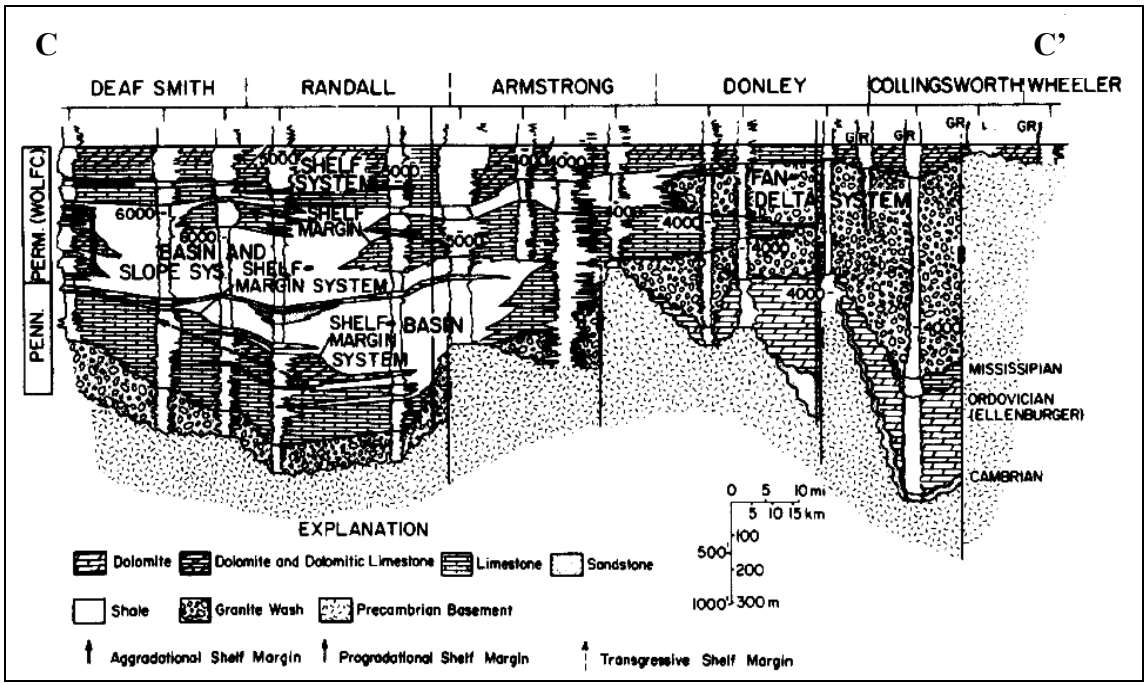

Figure 2.8 East-west regional cross section C-C'. Location of line shown in Figure 2.5

(After Schenewerk, 1980)

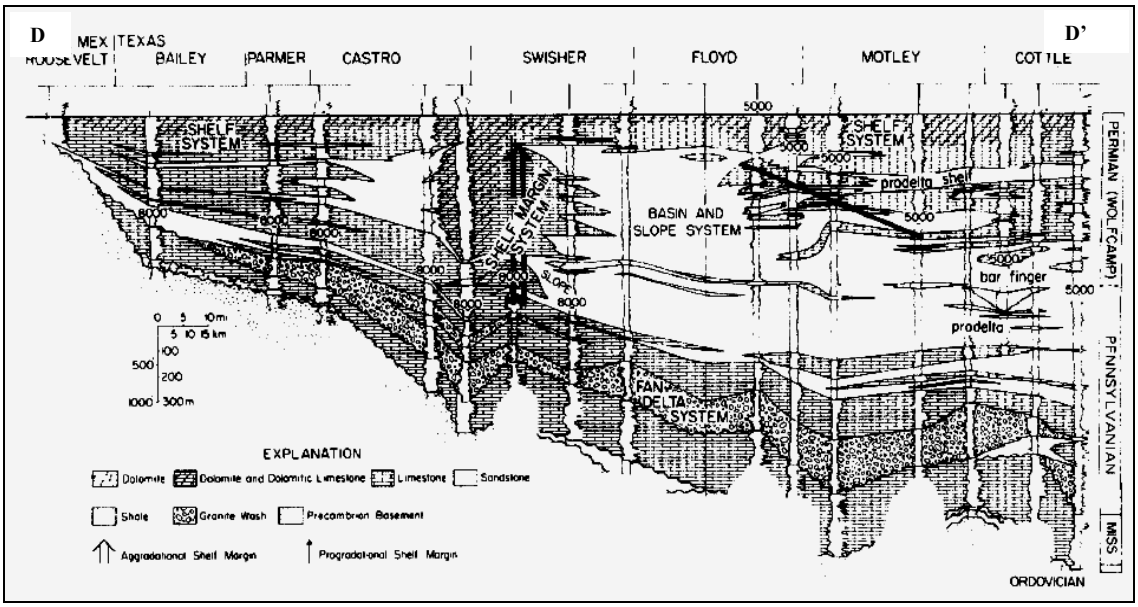

Figure 2.9 East-west regional cross section D-D'. Location of line shown in Figure 2.5

(After Schenewerk, 1980)

CHAPTER III

3D SEISMIC ATTRIBUTES

Introduction

The Oxford Dictionary defines an attributes as, "A quality ascribed at any person or thing". Taner, 2001 have extended this definition to: "Seismic attributes are all the information obtained from seismic data, either by direct measurements or by logical or experience based reasoning".

A seismic attribute is any measure of seismic data that helps us visually enhance or quantify features of interpretation interest. A good seismic attribute is either directly sensitive to the desired geologic feature or reservoir property of interest, or allows me to define the structural or depositional environment and thereby enables us to infer some features or properties of interest. (Chopra and Marfurt, 2008)

One of the goals of seismic attributes is to somehow capture this expertise by quantifying the amplitude and morphological features seen in the seismic data through a suite of deterministic calculations performed on a computer. (Chopra and Marfurt, 2007)

Footprint

Acquisition footprint describes the seismic noise that is closely related to acquisition geometry and sampling intervals (Bangrang et al., 2008). Marfurt et al. (1998) define acquisition footprint as "any pattern of noise that is highly correlated to the

geometric distribution of sources and receivers on the earth's surface". Stacking combines traces obtained at different offsets and azimuths. Because of the surfaces-acquisition geometry, different bins may contain different combinations of offsets and azimuths in addition to differences in the total number of traces to be stacked (Chopra and Marfurt, 2008). Drummond et al. (2000) mentioned two causes of footprint: the first is related with the acquisition geometry and the second is related to errors or limitations in signal processing.

The processor's goal is to avoid exacerbating the footprint during the processing. In addition to careful velocity and statics analysis, data interpolation to avoid operator aliasing may be performed (Chopra and Marfurt, 2008).

3D Seismic Attributes interpretation

Seismic attributes are dependent on several factors including structural complexity, lithology, change in thickness, layering, and data quality. Definitions of attributes used in this thesis can be found in Appendix A.

Acquisition Footprint

The first step in interpretation is to check the data quality. The Boomer Sooner survey was acquired in 1993 and is strongly affected by footprint. Normally footprint is strongest on shallow time slices and, in general, heals with depth, but in this survey the footprint effect in the low frequency and high frequency signal. Figure 3.1 shows the footprint effect at the time slice t= 500 ms.

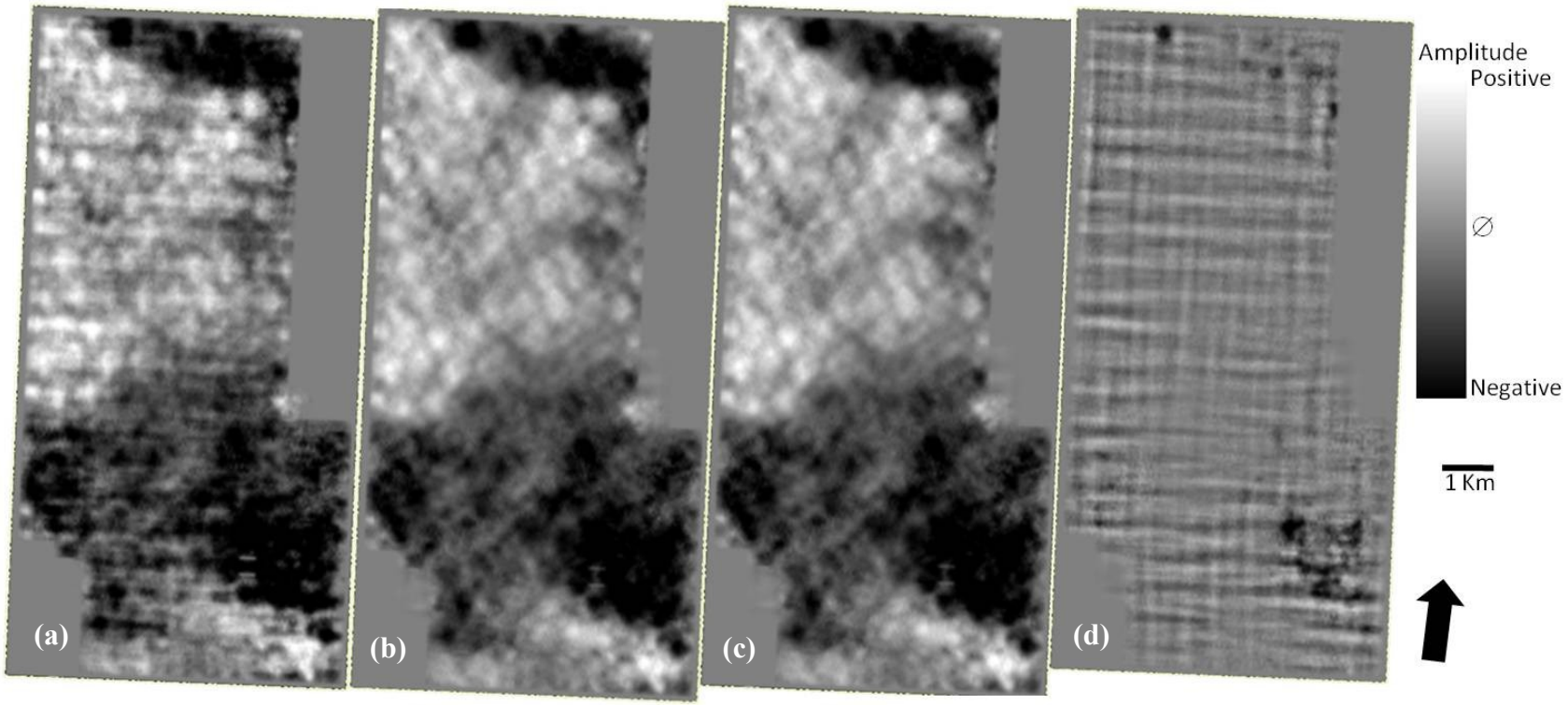

Figure 3.1 Comparison between raw data and filtered data in the Boomer Sooner data set.

(a) Raw seismic data at the time slice t=500 ms, (b) seismic data after first iteration footprint removal algorithm at the time slice t=500 ms (c) seismic data after second iteration footprint removal algorithm at the time slice t=500 ms and (d) the noise associated with the footprint, this is the signal that was removed from the original data set, using the footprint removal algorithm described by Falconer and Marfurt (2008).

Due to the strong acquisition footprint effect in the Boomer Sooner data set, a workflow to remove this effect was designed (Figure 3.2). This workflow is based in the dip of the data set. The first step used the seismic amplitude data as input of the dip3d program. The dip3d uses a Kuwahara multiple overlapping window dip search where the window with the highest, the confidence (coherence) is used for subsequent structure-oriented filtering.

For my data, I applied a principal component filter along the dip and azimuth, within the "best" window to reject cross-cutting noise and preserve edges. It is often useful to apply this workflow iteratively, as shown in Figure 3.2.

Figure 3.3 shows input line AA' before and after two passes of structure-oriented filtering. Figure 3.4 shows the rejected noise plotted at the same scale.

Figure 3.5 shows input line BB' before and after two passes of structure-oriented filtering. Figure 3.6 shows the rejected noise plotted at the same scale.

Figure 3.7 shows time slices at t=1.2 s before and after one and two passes of structure-oriented filtering and the rejected noise plotted at the same scale.

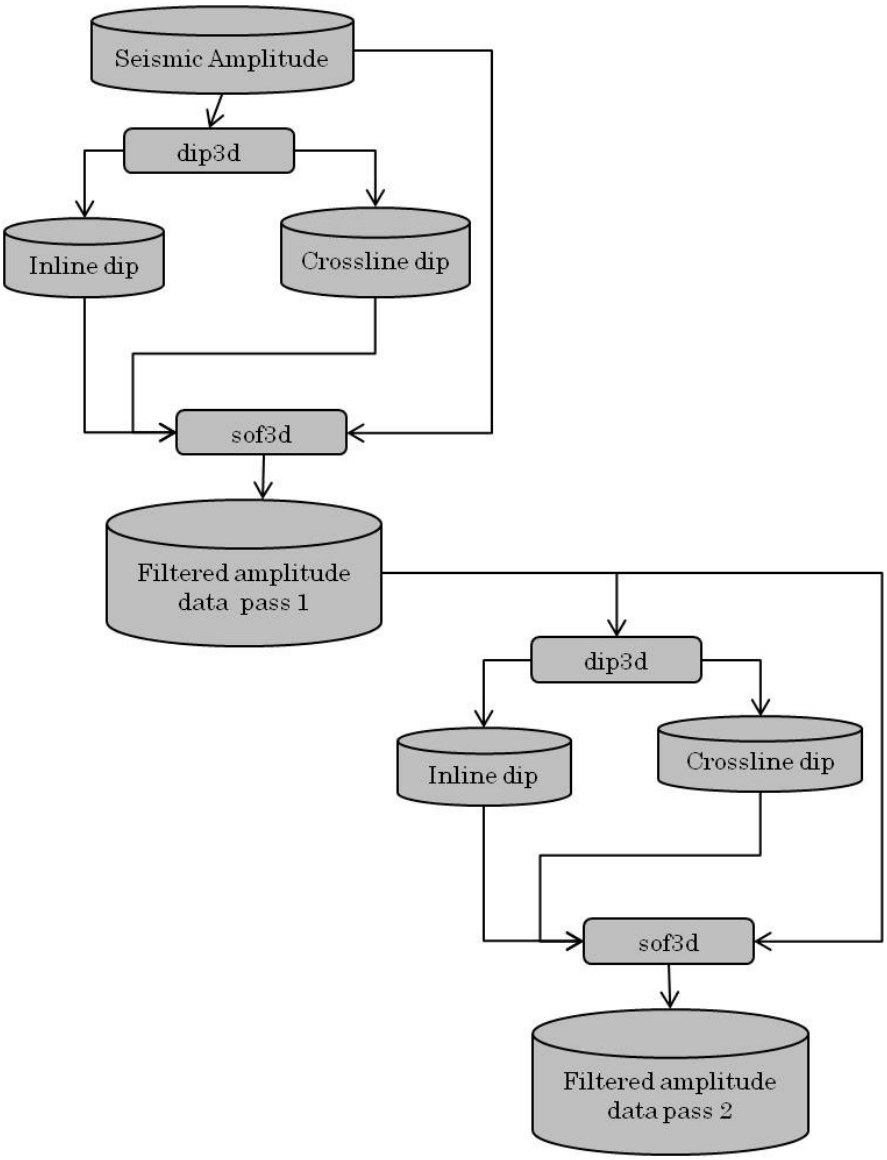

Figure 3.2Workflow used to remove the acquisition footprint in the Boomer Sooner data. Program dip3d computes inline and crossline components of reflector dip from the seismic amplitude data. Program sof3d applies a principal component edge preserving filter along the structure.

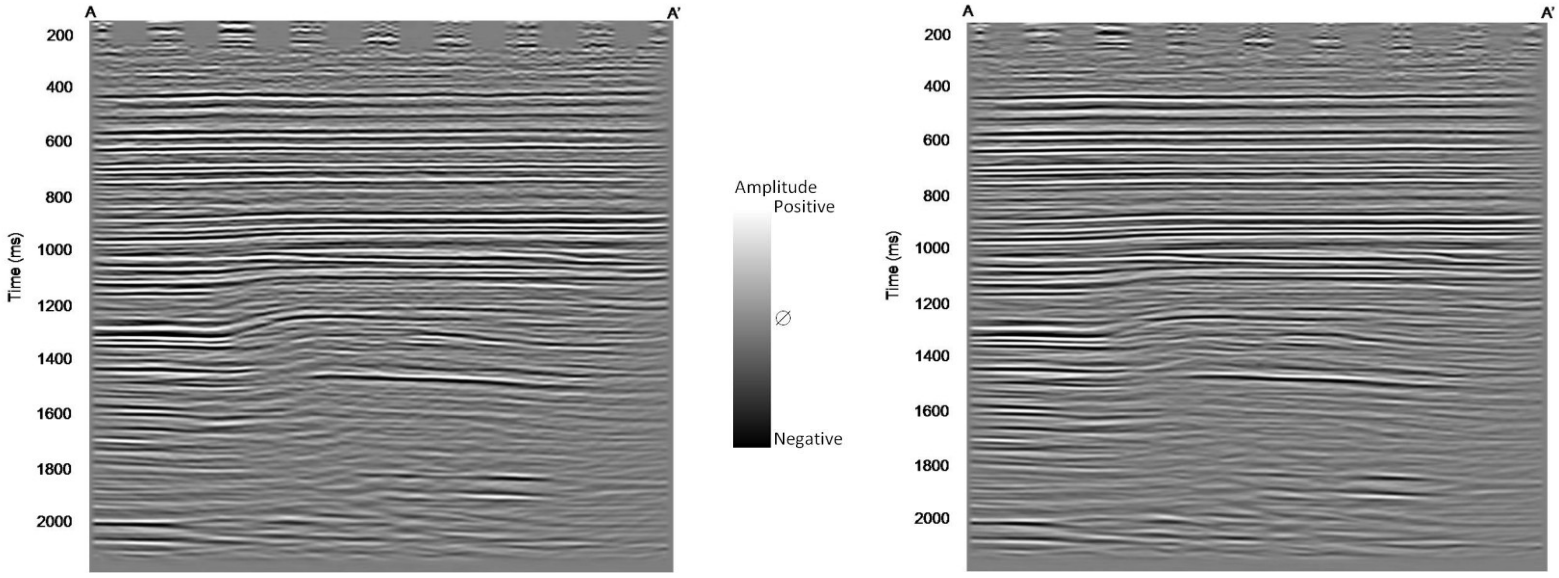

(a) (b)

Figure 3.3 Line AA' (a) before and (b) after two passes of structure-oriented filtering.

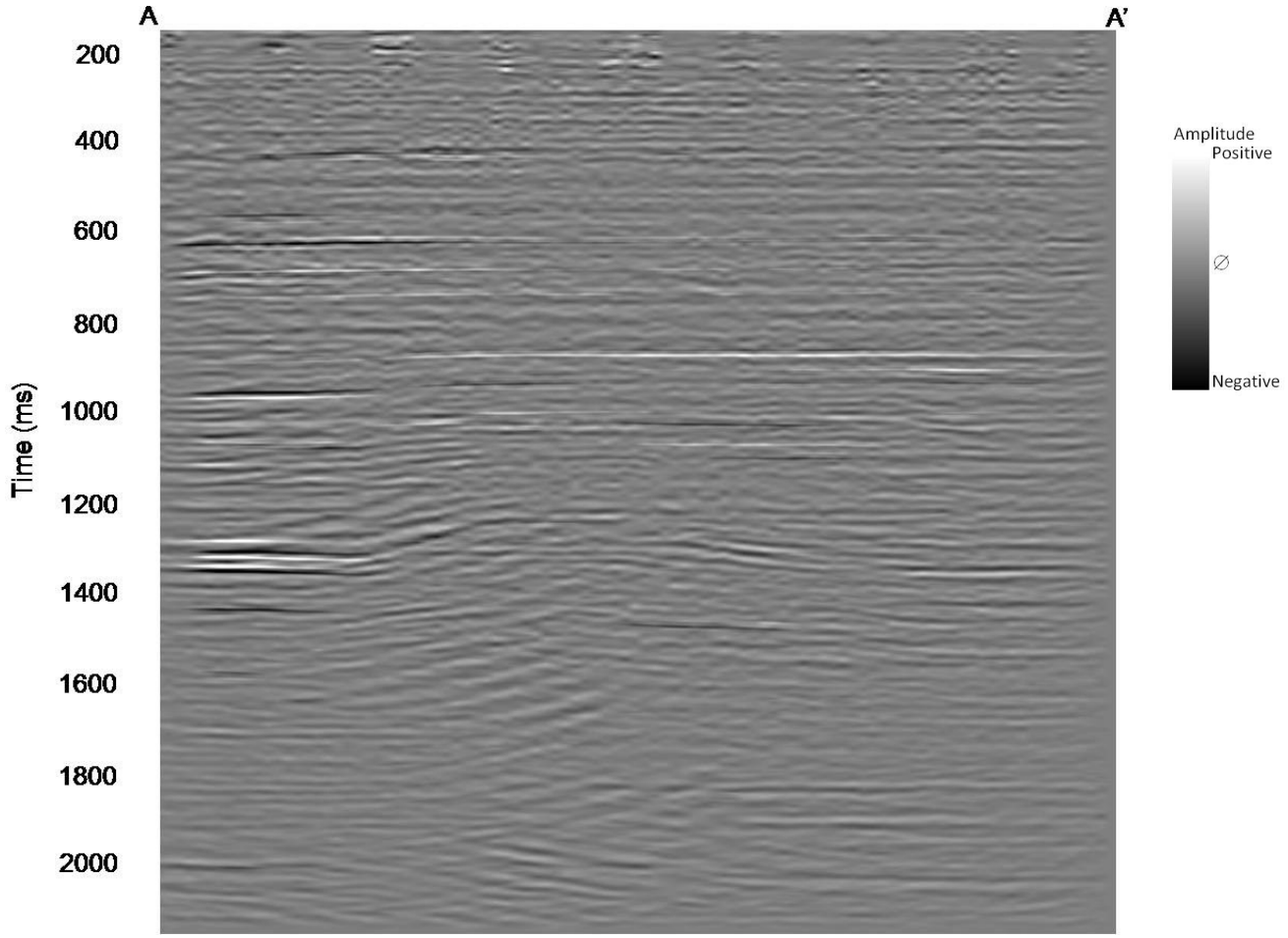

Figure 3.4 The reject noise at the line AA'.

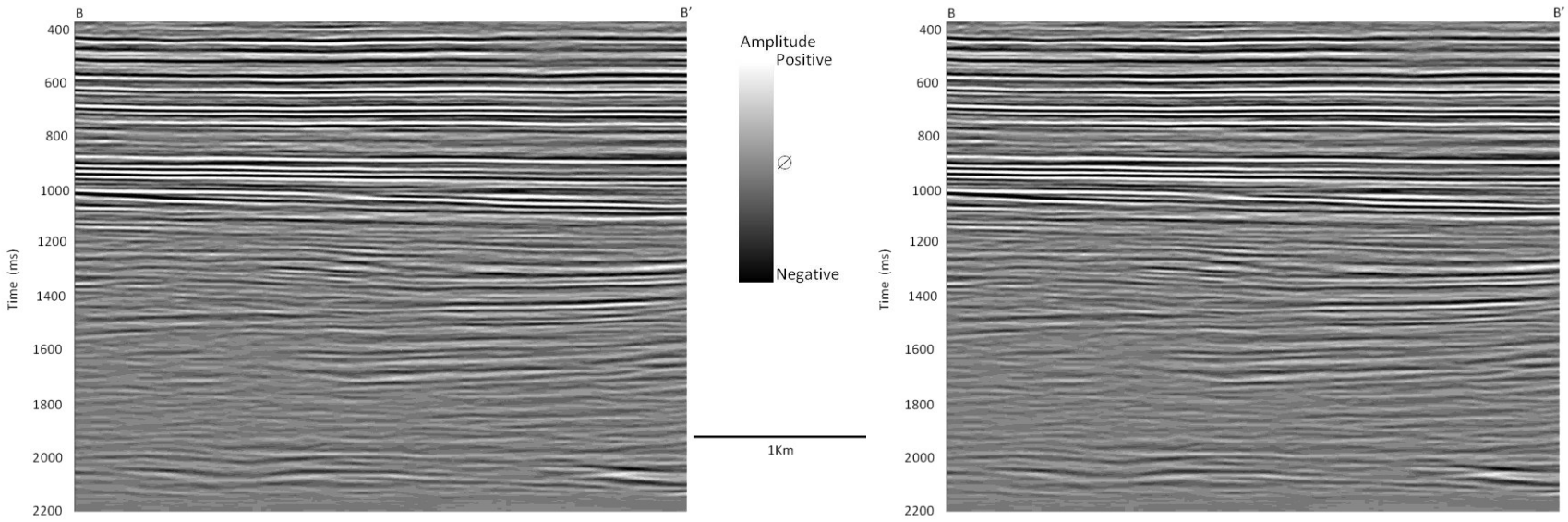

Figure 3.5 Line BB’ (a) before and (b) after two passes of structure-oriented filtering.

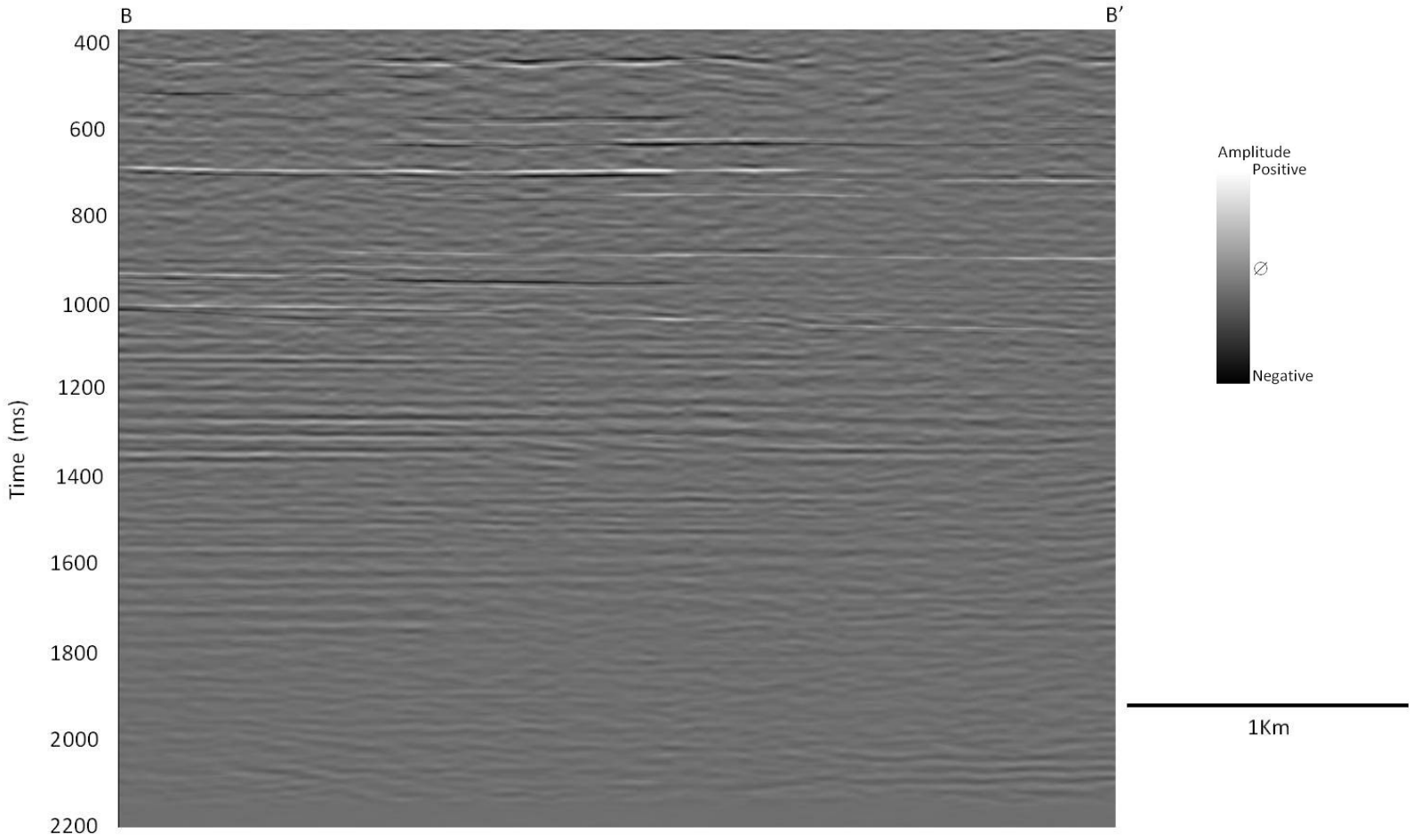

Figure 3.6 The reject noise at the line BB'.

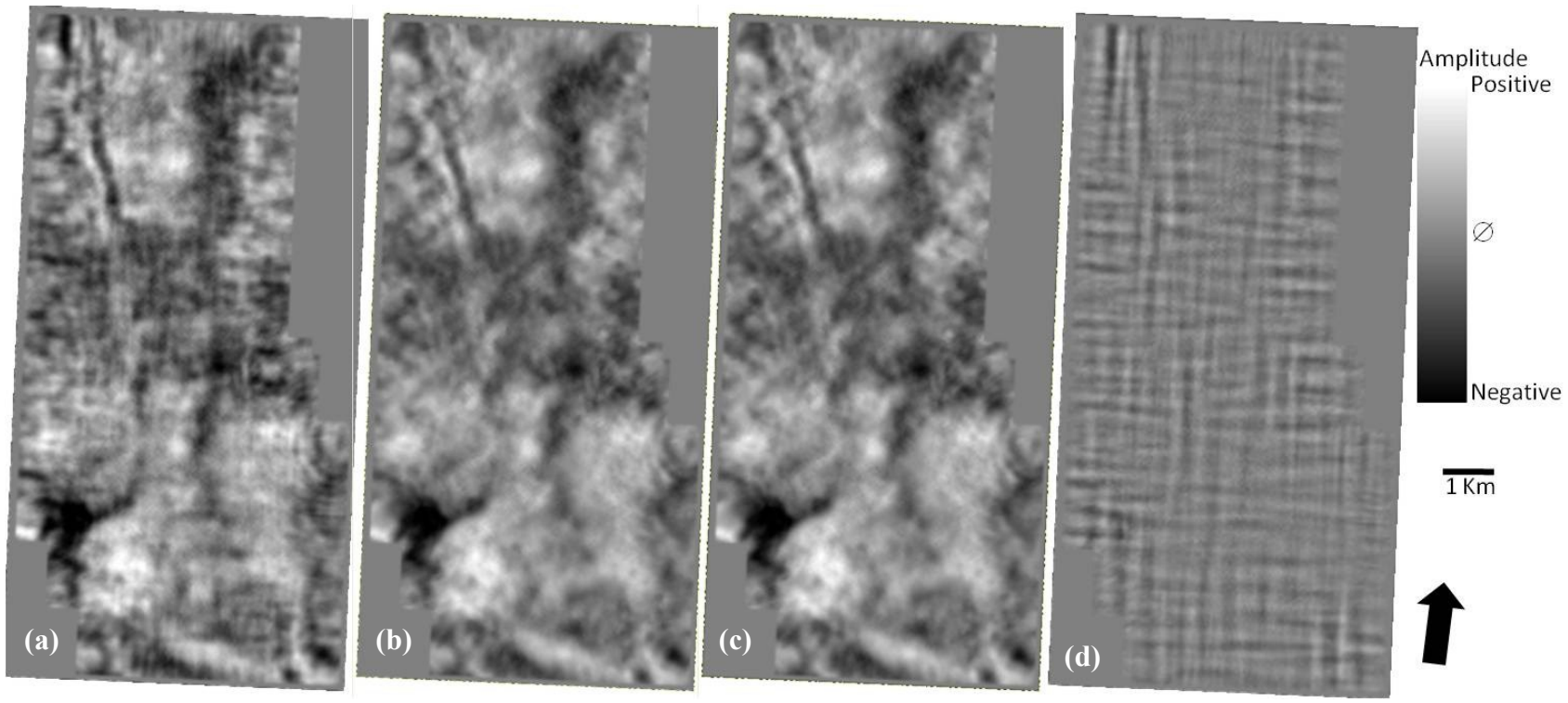

Figure 3.7 Comparison between raw data and filtered data in the Boomer Sooner data set.

(a) Raw seismic data at the time slice t=1200 ms, (b) seismic data after first iteration of footprint removal algorithm at the time slice t=1200 ms (c) seismic data after second iteration footprint removal algorithm at the time slice t=1200 ms and (d) the noise associated with the footprint, this is the signal that was removed from the original data set.

Seismic Interpretation

Figure 3.8 shows the location of the 3D seismic data and the color map is a regional structural map of the top Lefty Limestone. The map also shows the Bravo dome, which was subaerially exposed during Pennsylvanian time. This dome provided the source of the Granite Wash for the Dalhart basin and Whittenburg Trough, which are separated by a ridge or structural nose.

Four main horizons were interpreted: the Brown Dolomite, the top of the Granite Wash, the bottom of the Granite Wash and the basement. These horizons were interpreted based on five cross sections made with the well log data available for this study.

The well map (Figure 3.9) shows the location of these cross sections; three of these sections trend NW-SE direction and the other two sections trend NE-SW.

Figures 3.10 and 3.11 show NE-SW cross-sections (Well section NE-SW2 and well section NE-SW1 in figure 3.9) showing that the Granite Wash is locally deposited as a classic fan-delta, with massive sand in the lowest part, grading upward to a much thinner sandy section at the top of the structure.

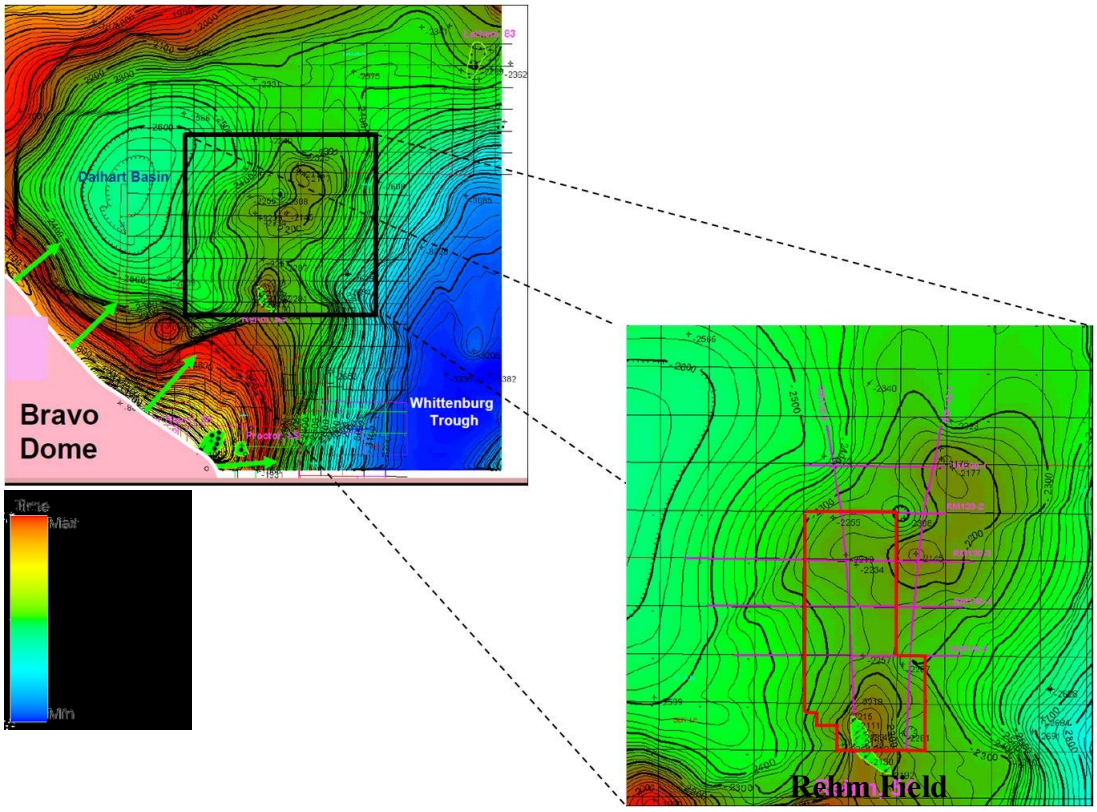

Figure 3.8 Regional structural map of the top Lefty Limestone.

The Boomer Sooner survey (red square) is located north east of the Bravo Dome and to the east of the Dalhart basin. (After Burnett, 2002)

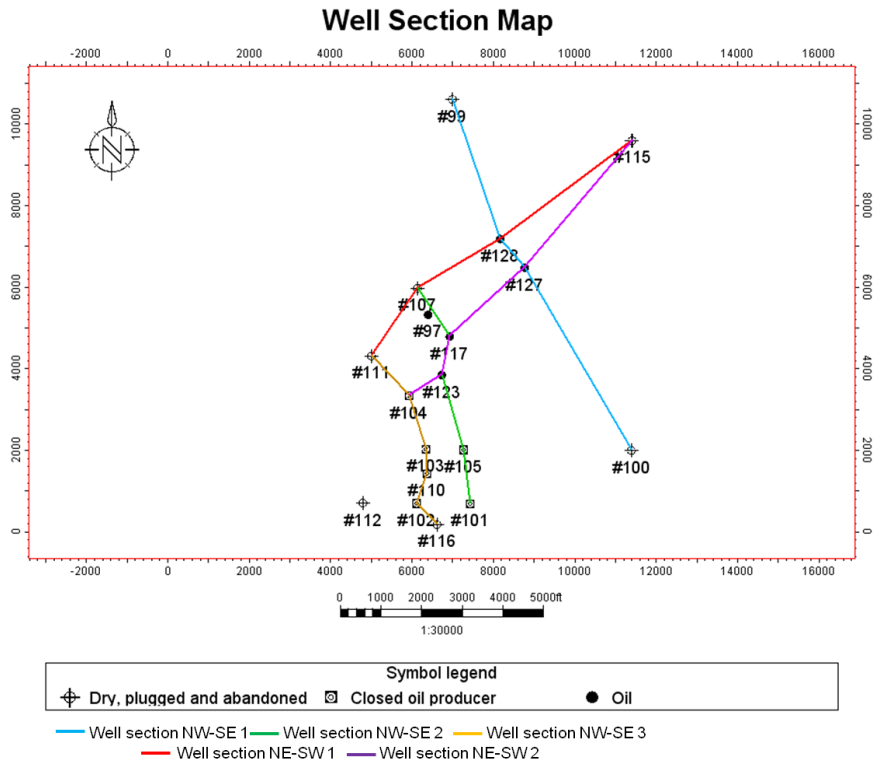

Figure 3.9 Location of well cross sections within the Boomer Sooner data set.

Figures 3.12, 3.13 and 3.14 shows the three NW-SE cross-sections (Well section NW-SE1, NW-SE2 and NW-SE3 in figure 3.9) which show that the Granite Wash is locally deposited as a classic fan-delta, laterally extended from north-west to south-east.

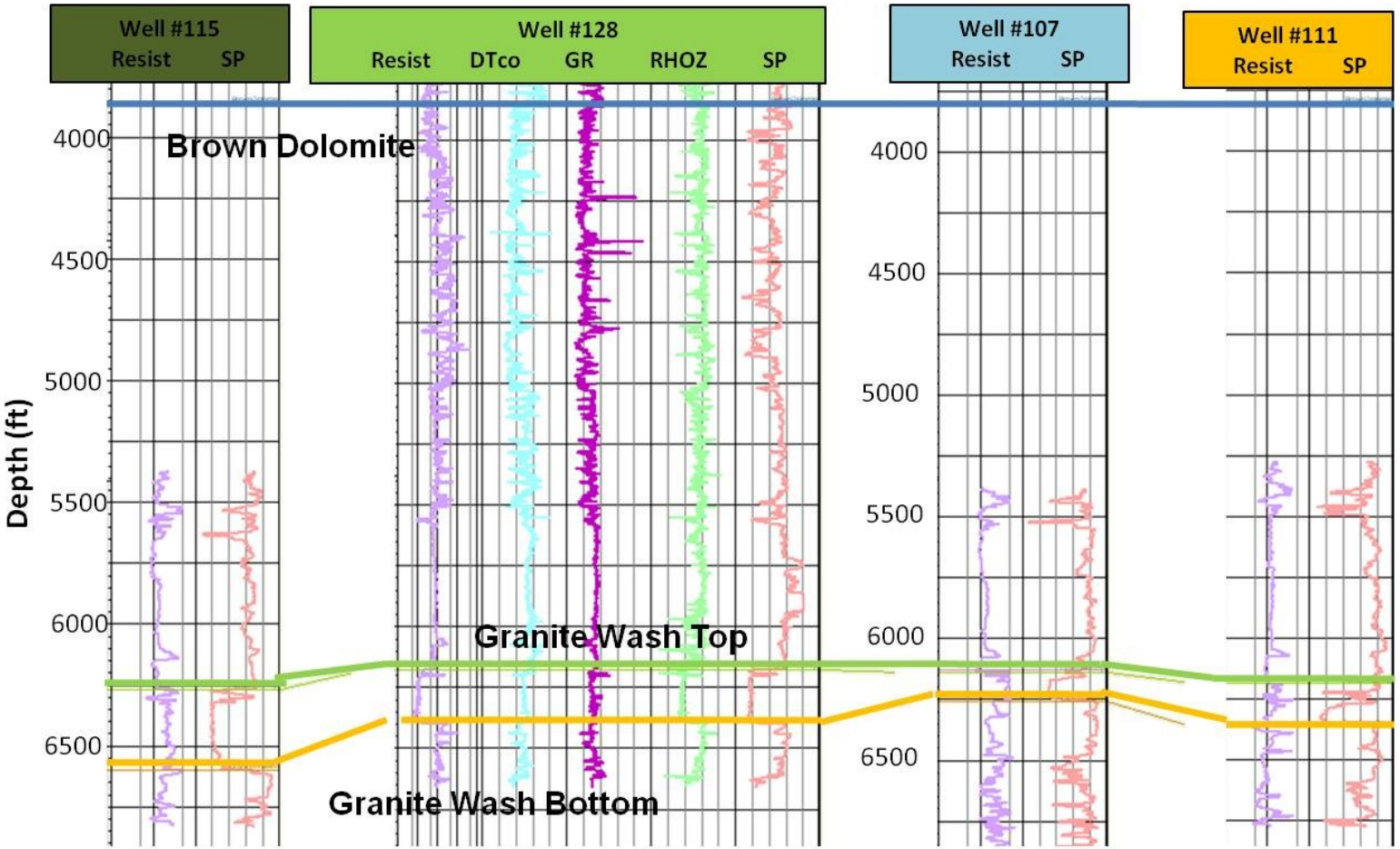

Figure 3.10 Cross-section NE-SW1 along wells 115, 128, 107 and 111.

Granite Wash is locally deposited as a classic fan-delta, massive sand at the lowest part, grading upward to a thinner sandy section.

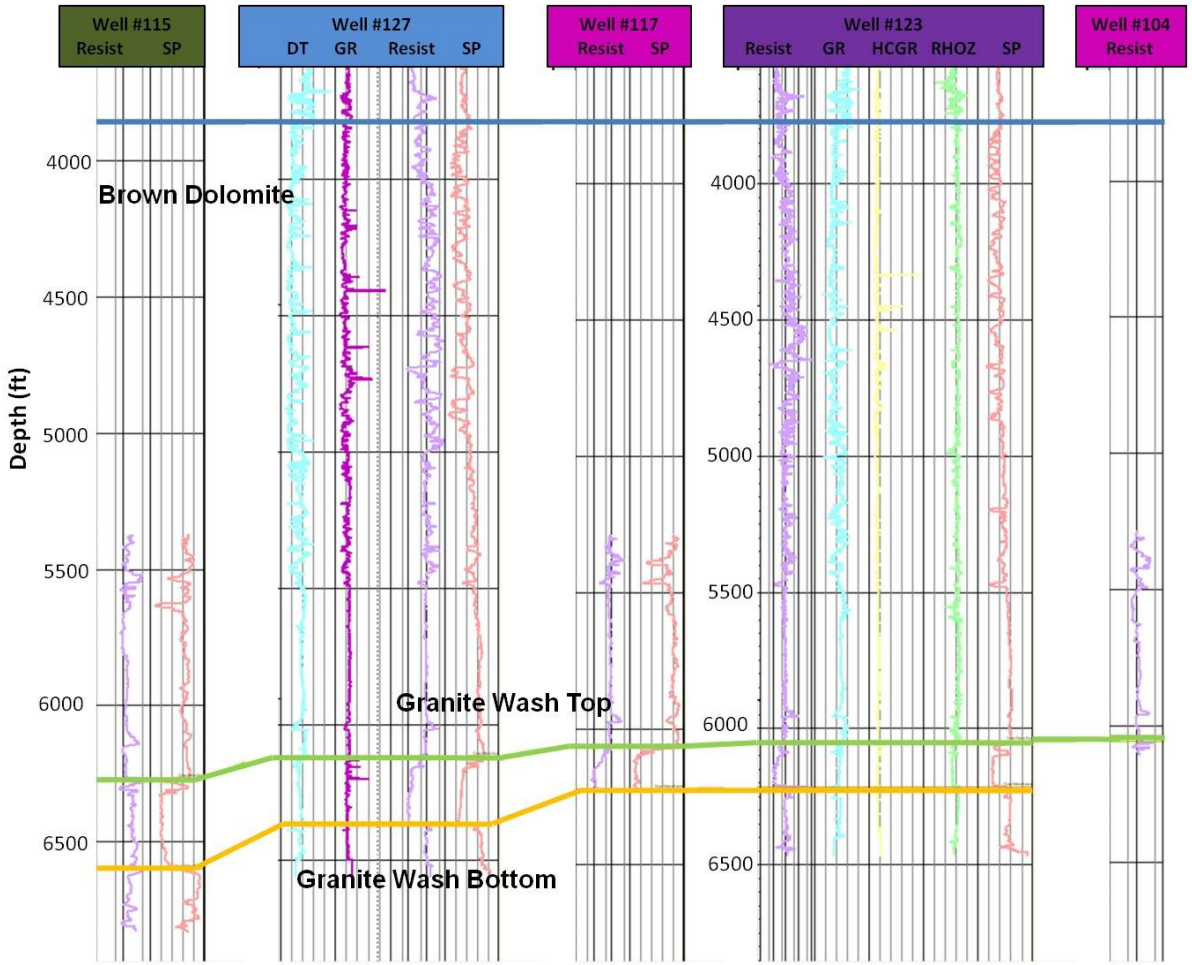

Figure 3.11 Cross-section NE-SW2 along wells 115, 127, 117, 123 and 104.

Granite Wash is locally deposited as a classic fan-delta, massive sand at the lowest part, grading upward to a thinner sandy section.

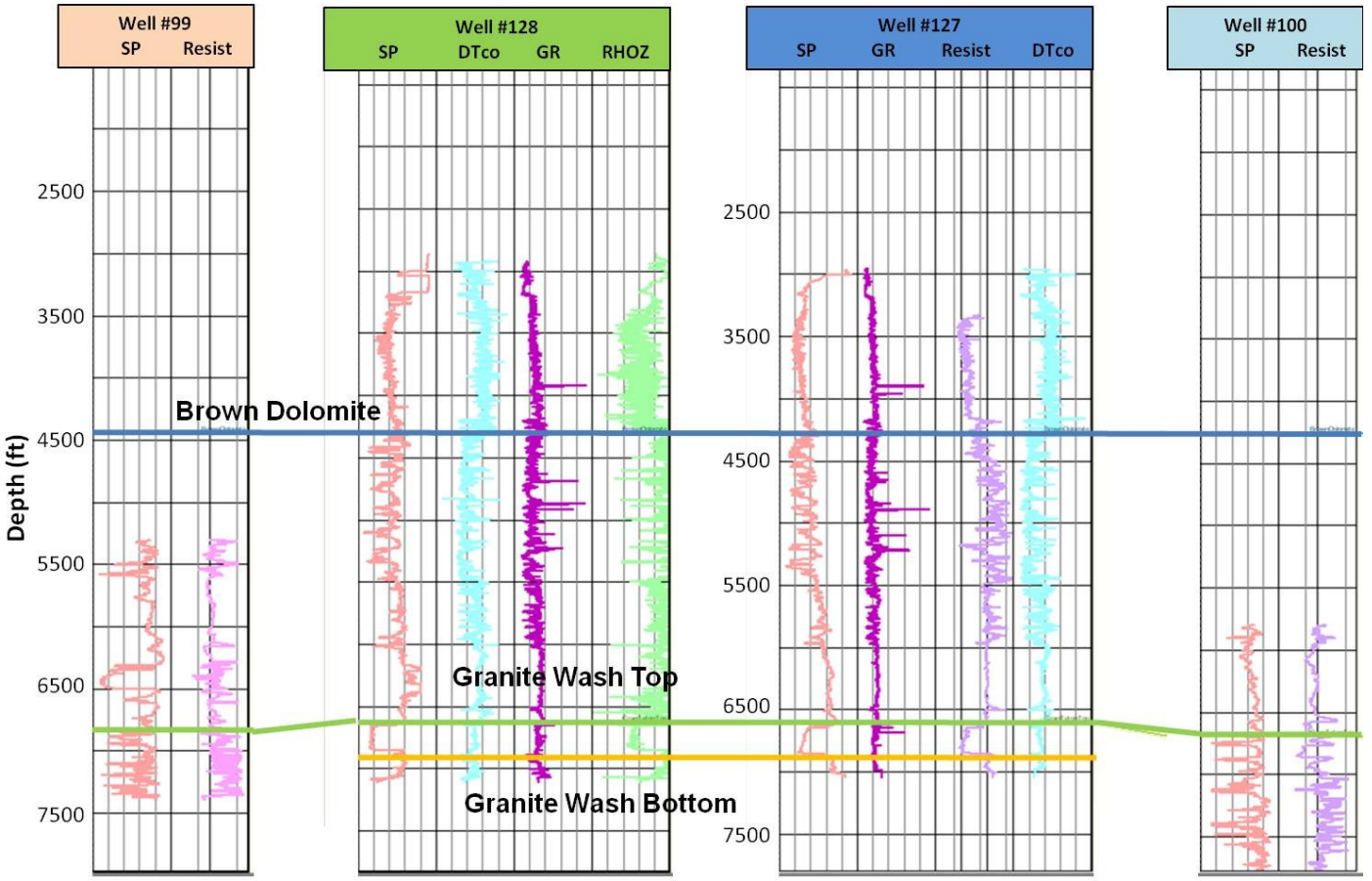

Figure 3.12 Cross-section NW-SE1 along wells 99, 128, 127 and 100.

Granite Wash is laterally extended from NW to SE.

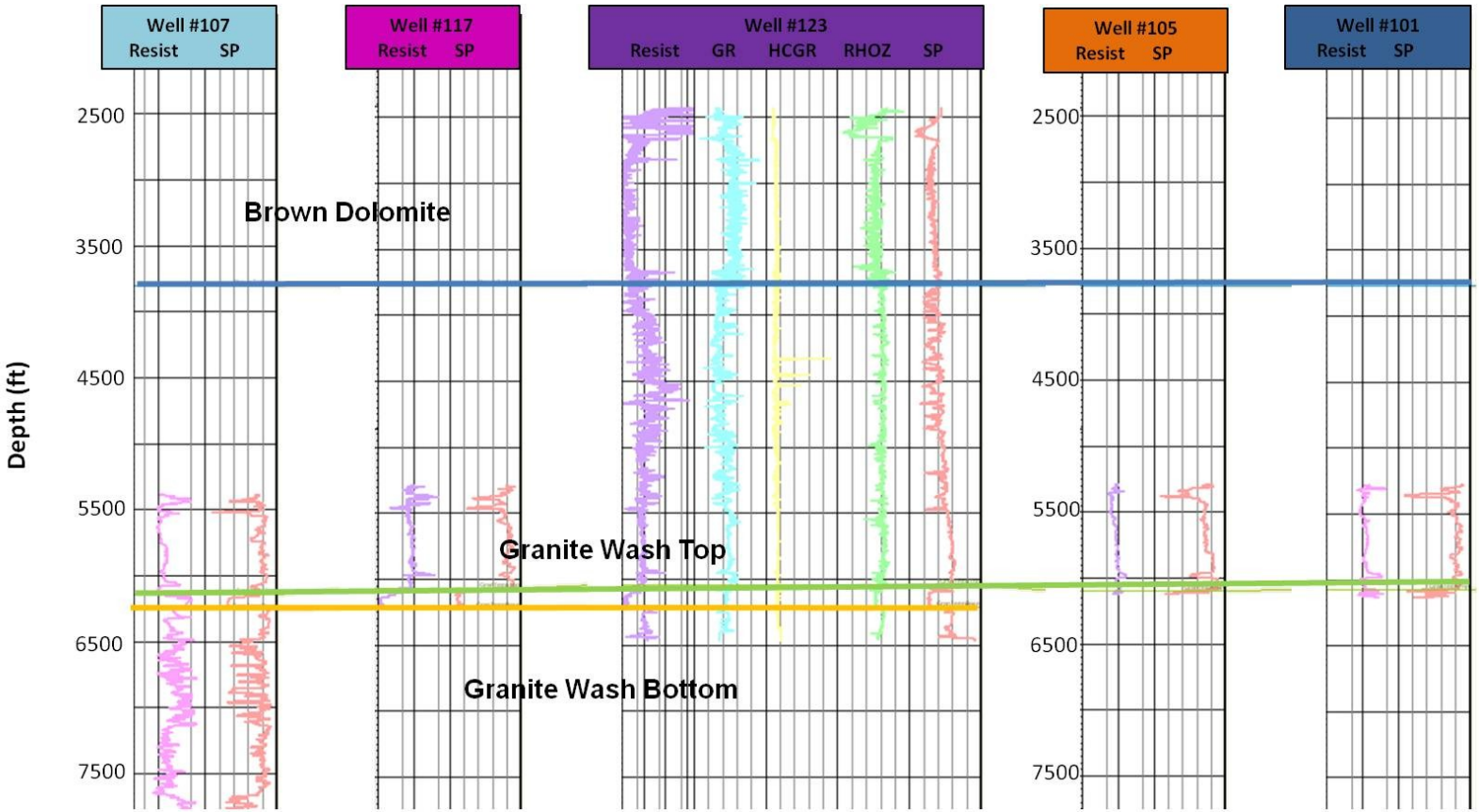

Figure 3.13 Cross-section NW-SE2 along wells 107, 117, 123, 105 and 101.

Granite Wash is laterally extended from NW to SE.

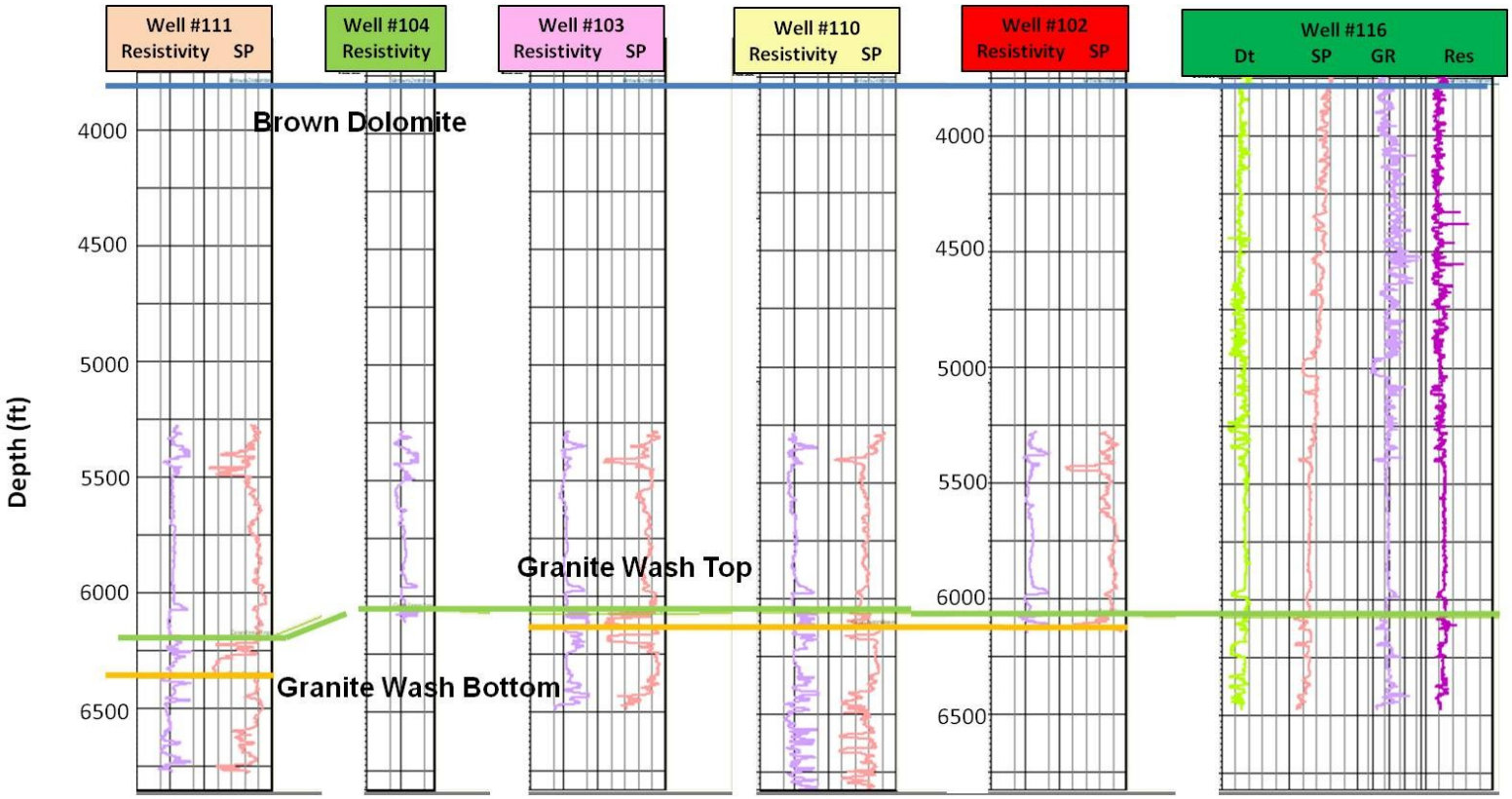

Figure 3.14 Cross-section NW-SE3 along wells 111, 104, 103, 110, 102 and 116.

Granite Wash is laterally extended from NW to SE.

Once the correlation using well log data is made the horizon can be picked in the amplitude seismic data set, previously corrected the acquisition footprint (Figure 3.15).

Lines AA' and BB' show the complexity of the area of study, from the top to the bottom, Brown Dolomite (purple line), Top of Granite Wash (green line), Bottom of Granite Wash (light green line) and Basement (blue line). Also in the figure the main fault (Fault #1) of this data set is shown (red line).

Fault #1 is the main structural characteristic in this area; this is a thrust fault that is running from North to South. The hanging wall is located at the east of the data set and the footwall is located in the west area of this data set. One of the evidences of the occurrence of this fault # 1 is that the sediments during the Pennsylvanian and Permian was coming from the west part of the basin (Figure 2.8), also in Figure 3.15 a progradation above the Brown Dolomite horizon (red ellipse) is an evidence of this fault #1.

The time-structure map of figures 3.17, 3.18 and 3.19 represent the top of the Granite Wash interval, the bottom of the Granite Wash and the top of Brown Dolomite respectively.

At the Granite Wash top and bottom, the time-structure maps (Figure 3.17 and 3.18) show a high running north-south, which represent the nose which separates the Dalhart basin from Whittenburg Trough. In this area some Granite Wash sediments can

are represented with the red arrows. The sediments in this area were transported from south-west to north-east and deposited as fan deposited as fan deltas (red arrows in Figures 3.17 and 3.18). Also the thrust fault running north-south is seen in this time-structure map (red line in Figures 3.17 and 3.18).

At the top of Brown Dolomite faults are not evident, but there are two structural highs located north and south of the study area (red arrows in Figure 3.19). Also a sinuous channel shaped with evidence of deposition from south to north is recognized in this time-structure map (white arrows in Figure 3.19). This dolomite is a diagenetic replacement rock because it crosses apparent bedding or facies boundaries in the Dalhart basin (Dutton and Goldstein, 1989). For this reason I hypothesize that this may be an incised channel fill that has been dolomitized.

The basement structural map shows that the deepest area of this structure is at the north (red arrows in Figure 3.20), which is coincident with the cross section shown in Figure 2.6.

Figure 3.21 shows the thickness map in the Granite Wash interval; the thickness in this reservoir varies from 5 to 150 ms in the study area. The thicker sediments are located to the north-east part of the area of study, related to the fan deposit location (red arrows). Also thicker intervals occur along the fault (white arrows).

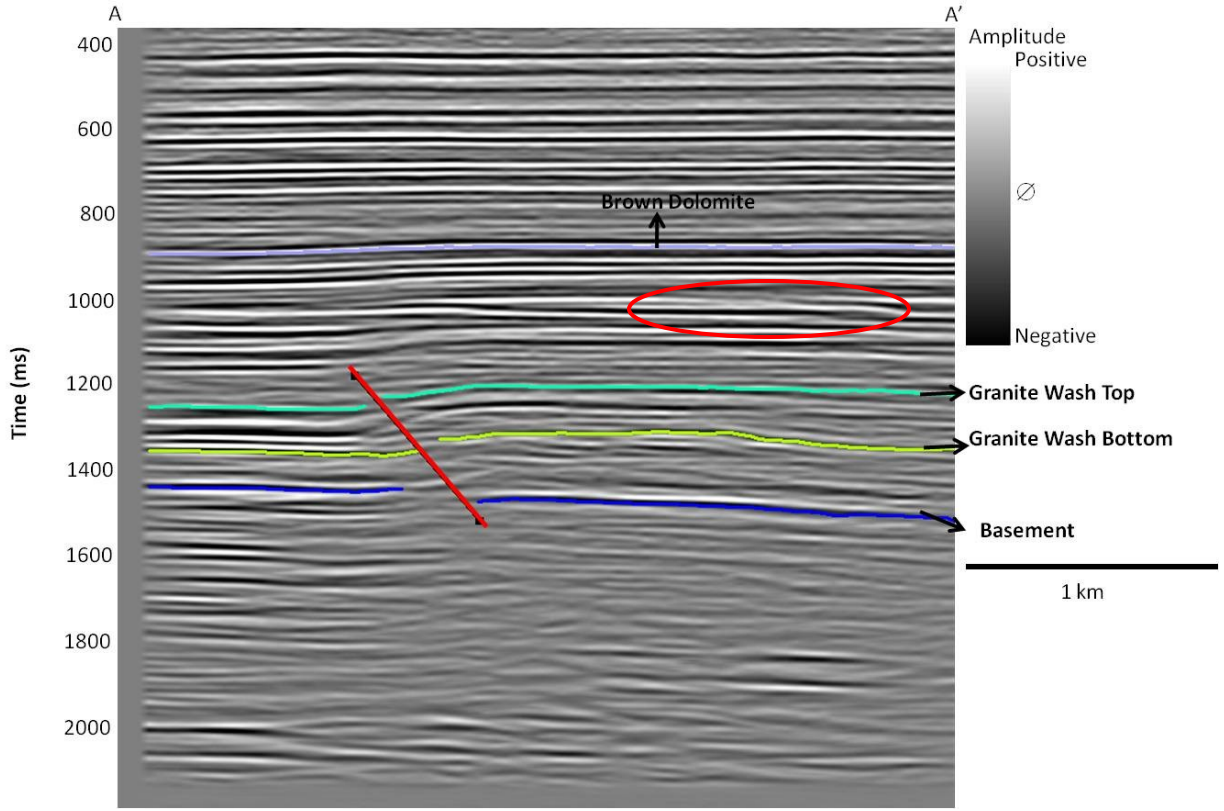

Figure 3.15 Line AA' showing the main horizons interpreted in this seismic data set.

From the top to bottom: Brown Dolomite (purple line), Top of Granite wash (green line), Bottom of Granite Wash (light green line) and Basement (blue line). Also in the figure the main fault (Fault #1) of this data set is show (red line). Location of line shown in Figure 3.17

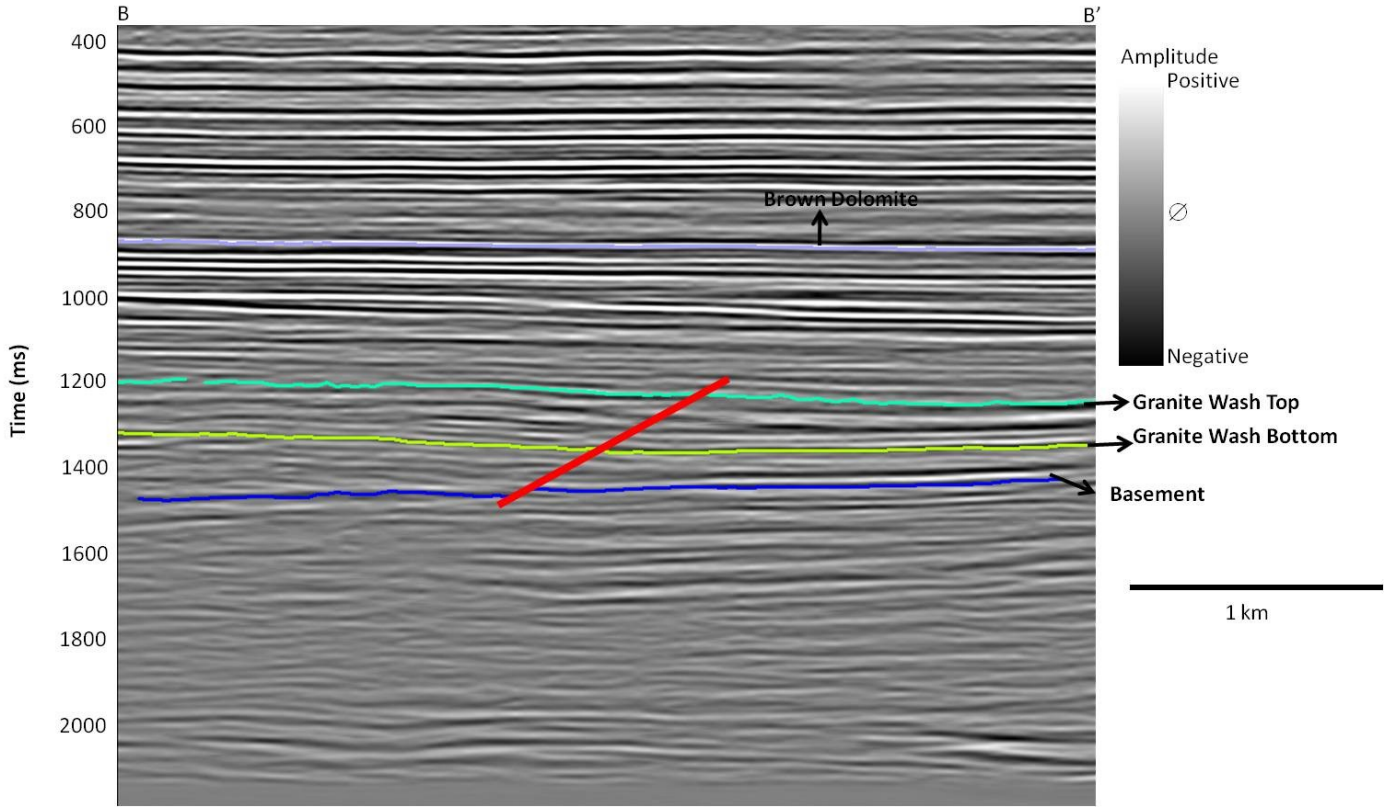

Figure 3.16 Line BB' showing the main horizons interpreted in this seismic data set.

From the top to bottom: Brown Dolomite (purple line), Top of Granite wash (green line), Bottom of Granite Wash (light green line) and Basement (blue line). Also in the figure the main fault (Fault #1) of this data set is show (red line). Location of line shown in Figure 3.17

Figure 3.22 shows the thickness map in the area between the top of the Granite Wash and the Brown Dolomite horizon. The thickness in this reservoir varies from 315 to 390 ms. The interval is thinner in the east part of the area of study (red arrows) and it is particularly thick along Fault #1's footwall (white arrows).

Figure 3.23 shows the thickness map in the area between the bottom of the Granite Wash and the Basement horizon. The thickness in this reservoir varies from 20 to 200 ms. The thicker sediments are located to the north-east part of the area of study (red arrows) and it is thin along Fault #1's footwall (white arrows).

Dip azimuth and dip magnitude maps are important not only because they constitute the basis of the estimation of related seismic attributes, but also because they give a general quantitative geological idea of horizon dip magnitude and dip azimuth.

Analyzing both results, dip azimuth and dip magnitude maps at the top of the granite wash horizon. The main thrust fault is represented by a red line in Figure 3.24. The azimuth related to this fault is between 225° and 250 °.

The main thrust fault is also represented with a red line in Figure 3.25, which is the dip azimuth and dip magnitude at the bottom of the Granite Wash horizon. Also the top and the bottom of the granite wash dip azimuth evidence that they are dipping to the east with an azimuth between 50° and 75°, very consistently.

The Figure 3.26 shows that the brown dolomite horizon is dipping slightly to the west.

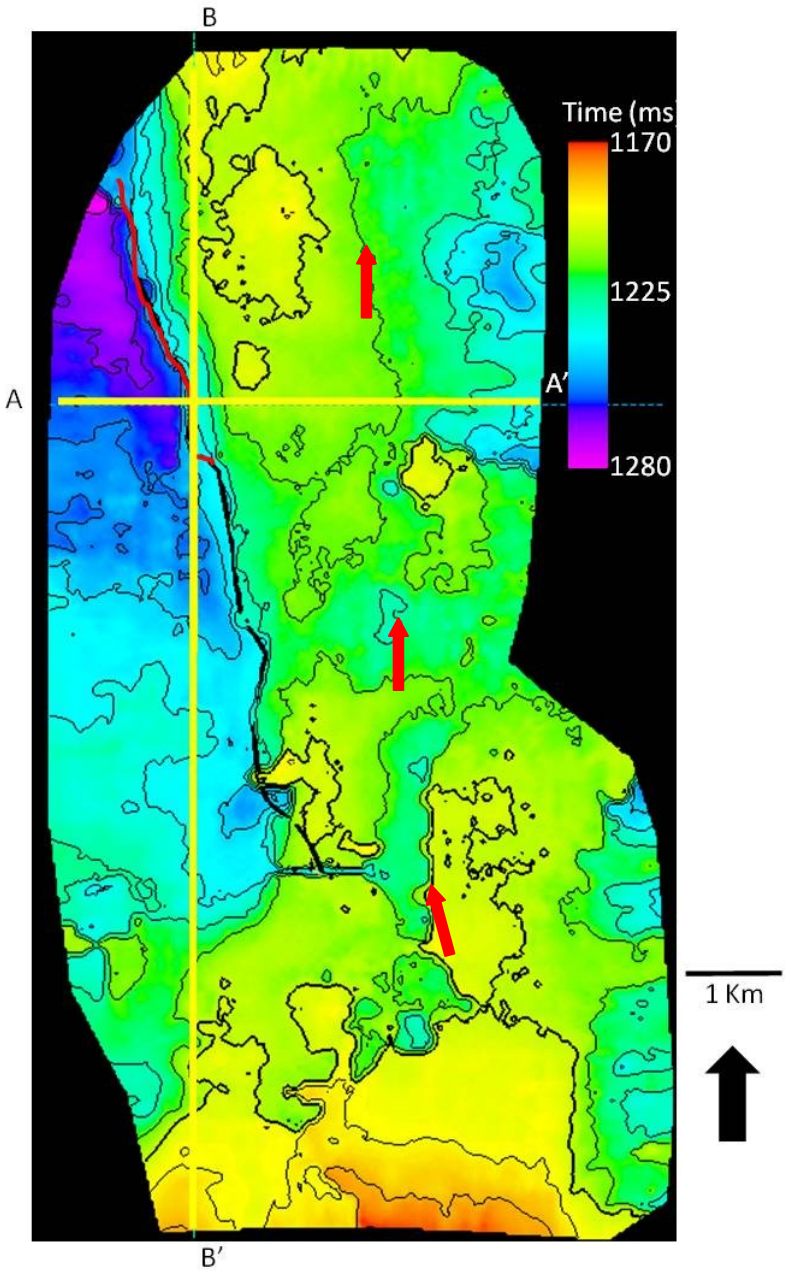

Figure 3.17 Time-structure map corresponding to the top of Granite wash.

Lines AA' and BB' shown in Figures 3.15 and 3.16. Fault # 1 is represented by a red line. The red arrows represent the sediments direction from South West to North East. Interval contours are every 10 ms.

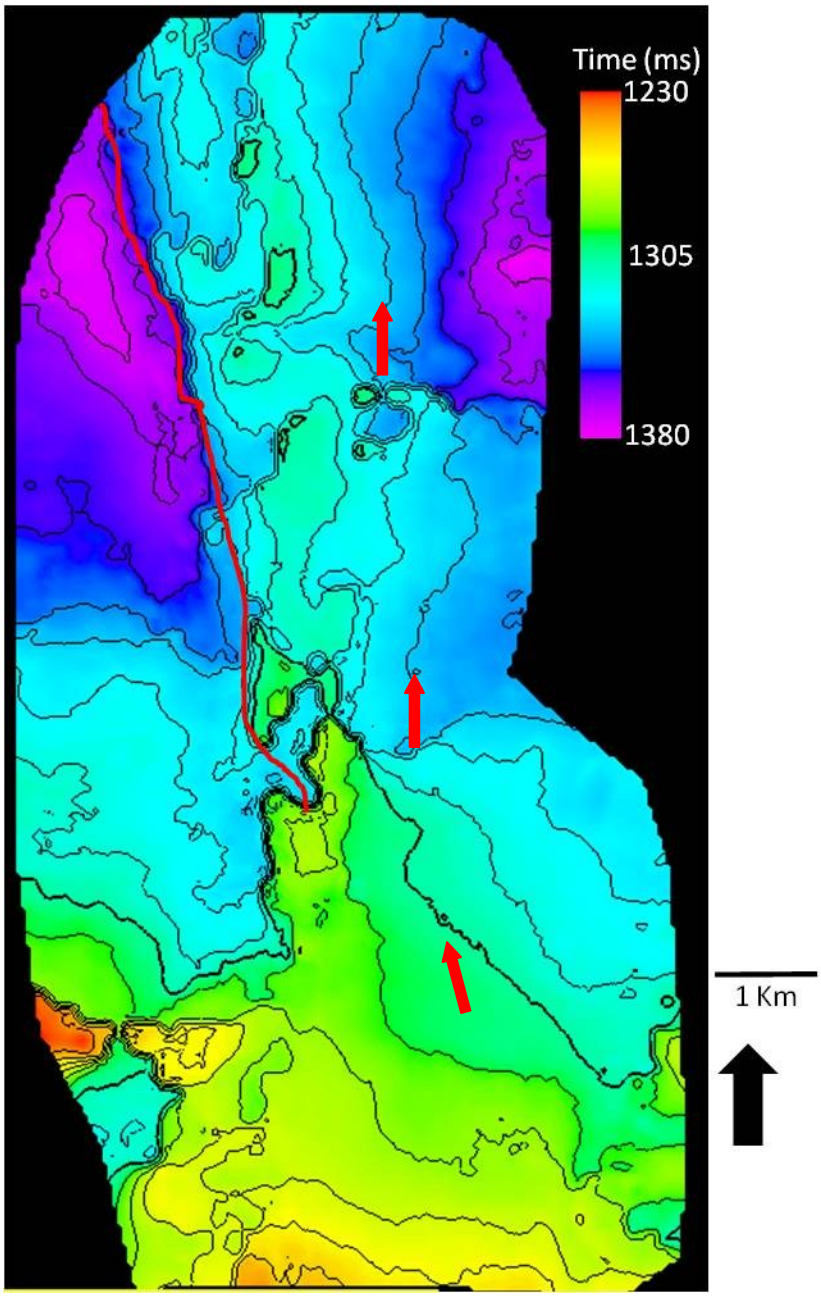

Figure 3.18 Time-structure map corresponding to the bottom of the Granite wash. Interval contours are every 10 ms. Fault # 1 is represented by a red line. The red arrows represent the sediments direction from South West to North East.

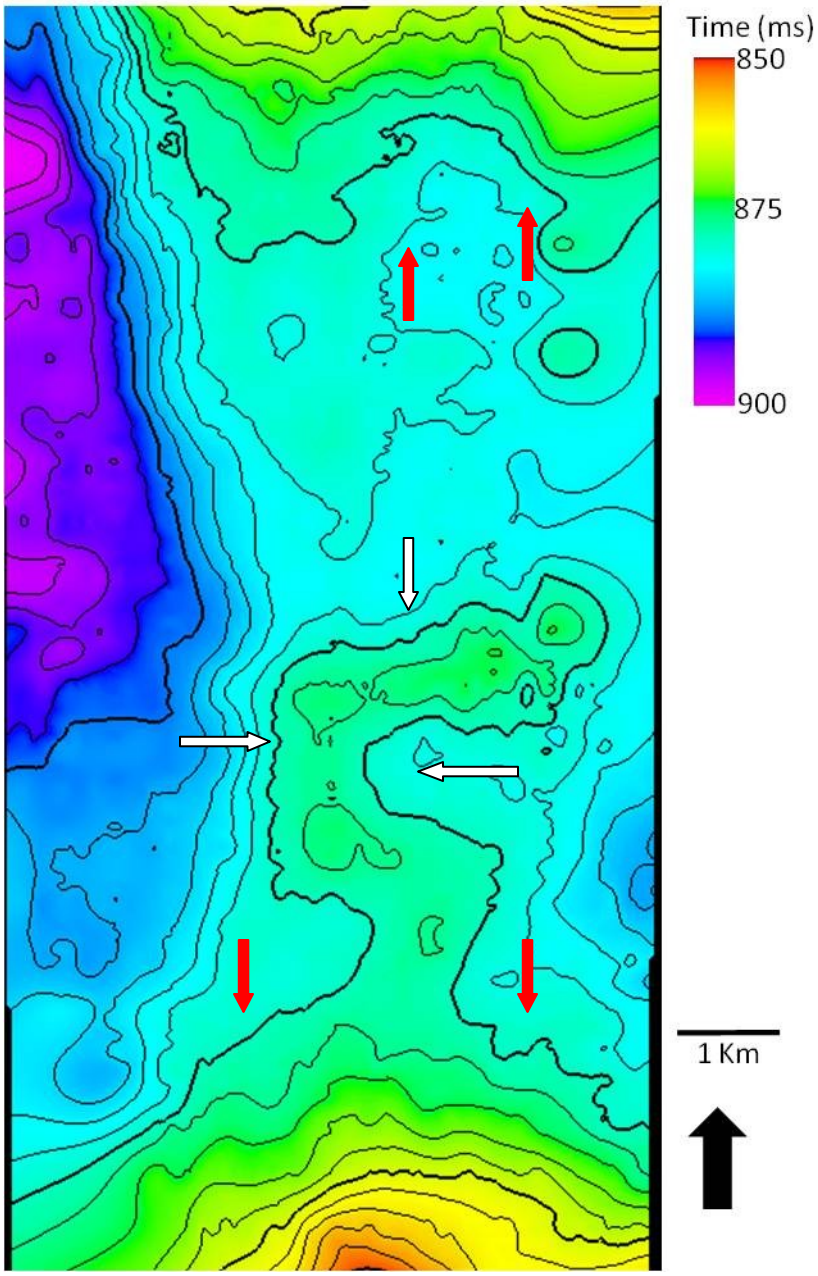

Figure 3.19 Time-structure map corresponding to the Brown Dolomite horizon. Interval contours are every 10 ms. Two structural highs located north and south of the study area are represented by red arrows; also a sinuous channel shaped with an evidence of deposition direction from south to north is represented by white arrows.

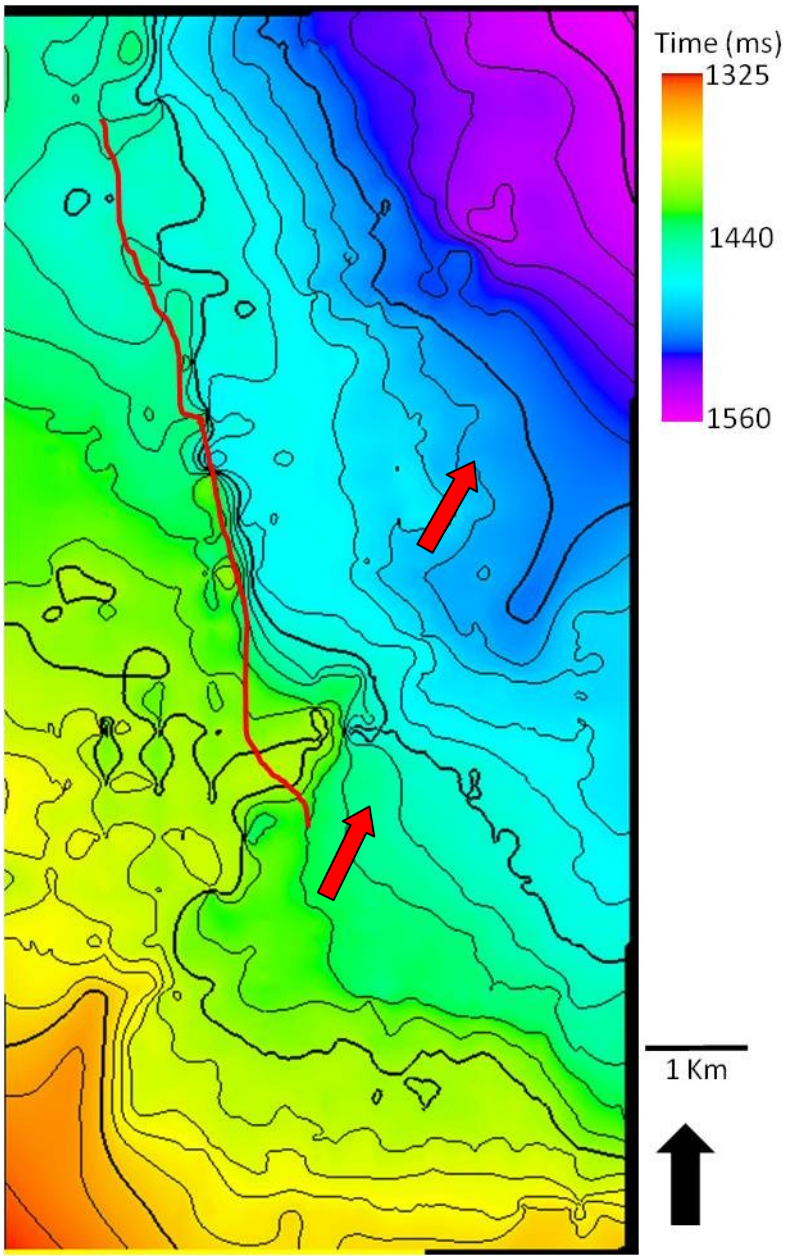

Figure 3.20 Time-structure map corresponding to the basement horizon.

Interval contours are every 10 ms. Fault # 1 is represented by a red line. The deepest area of the basement is at the north represented by the red arrows.

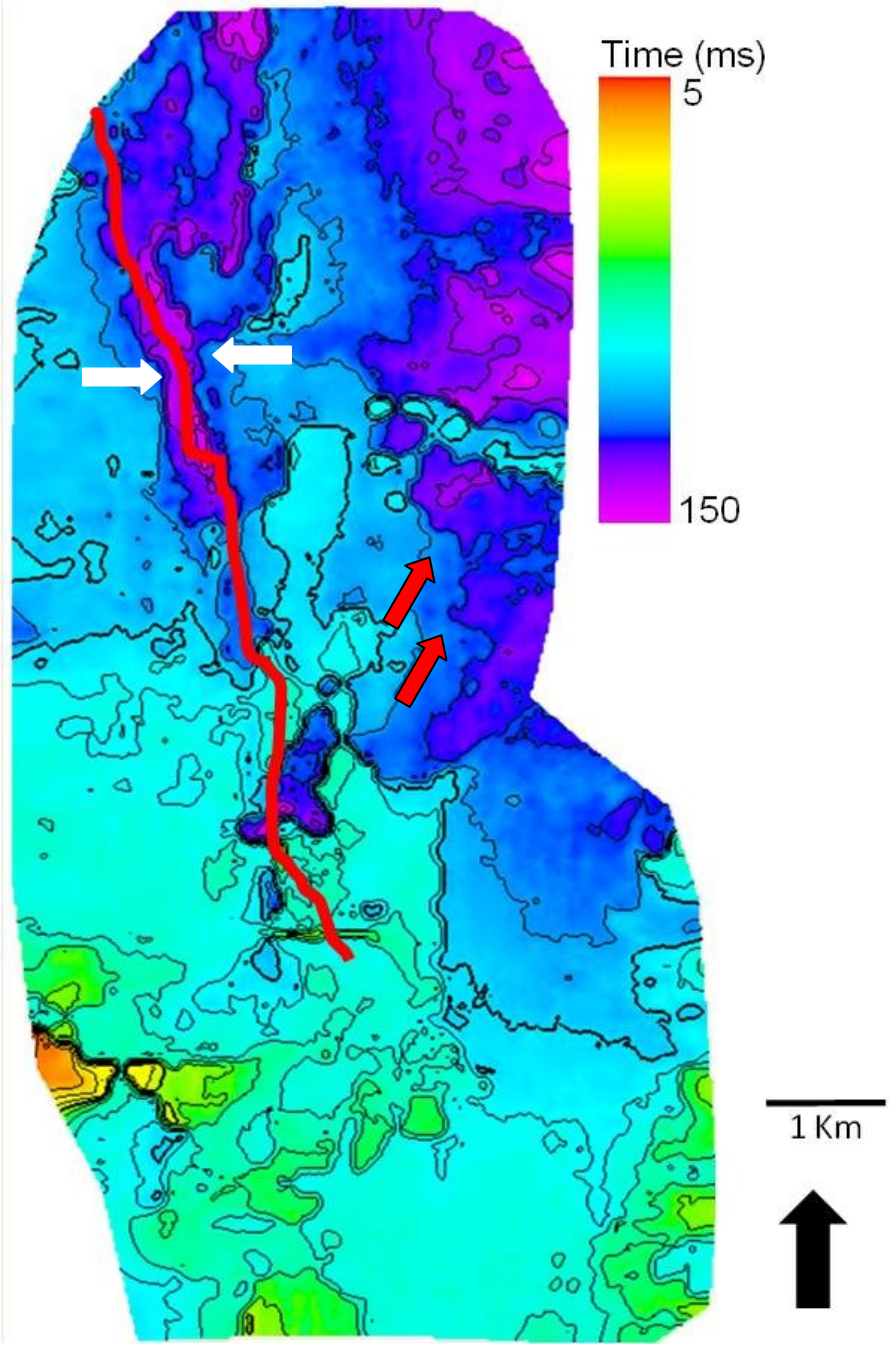

Figure 3.21 Thickness map corresponding to the Granite Wash interval.

Interval contours are every 10 ms. Thicker sediments are located to the north east part (red arrows) and along the fault #1 (red line and white arrows)

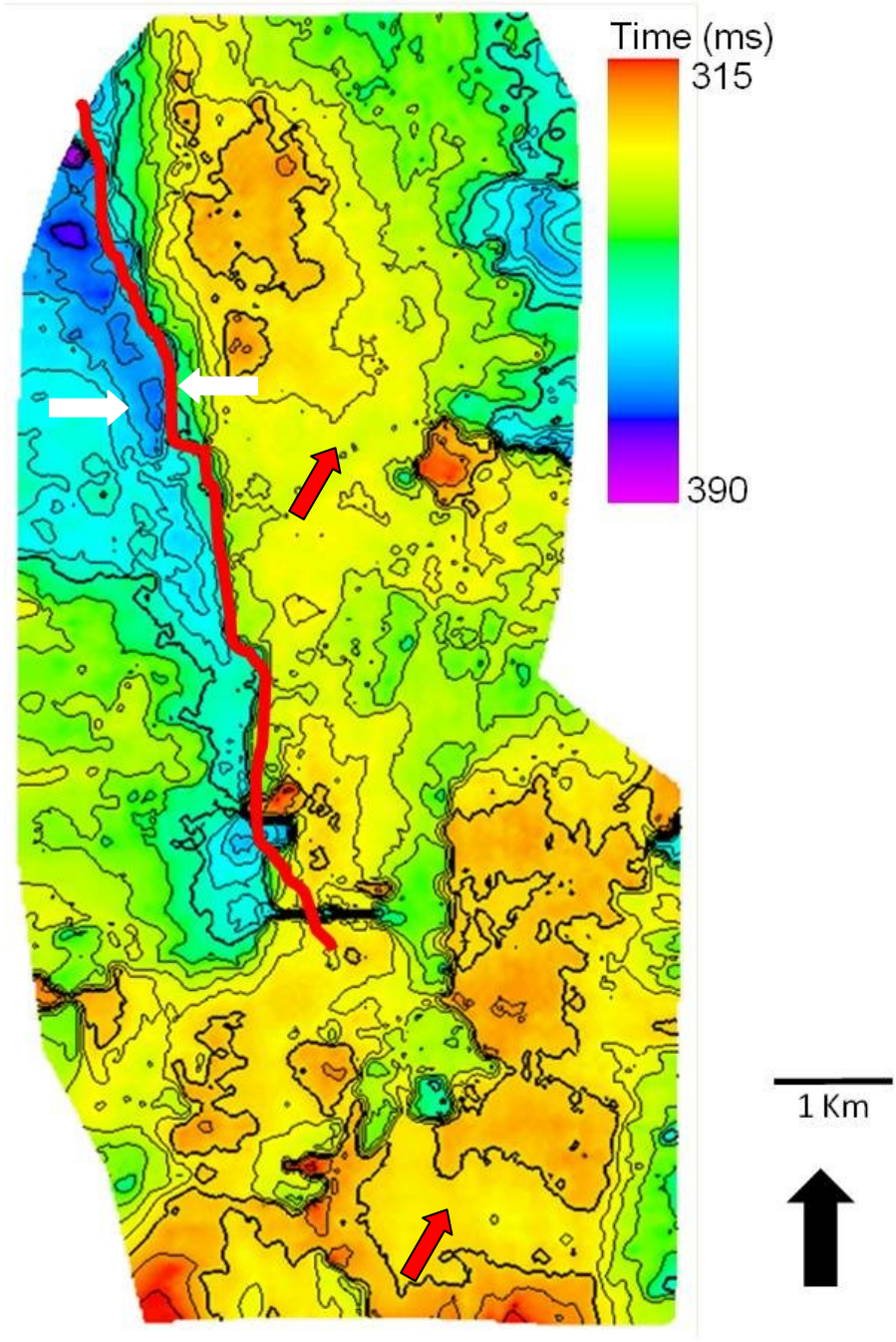

Figure 3.22 Thickness map between the Granite Wash and the Brown Dolomite.

Interval contours are every 10 ms. Thinner in the east part of the area of study (red arrows) and it is particularly thick along the Fault #1's footwall (red line and white arrows).

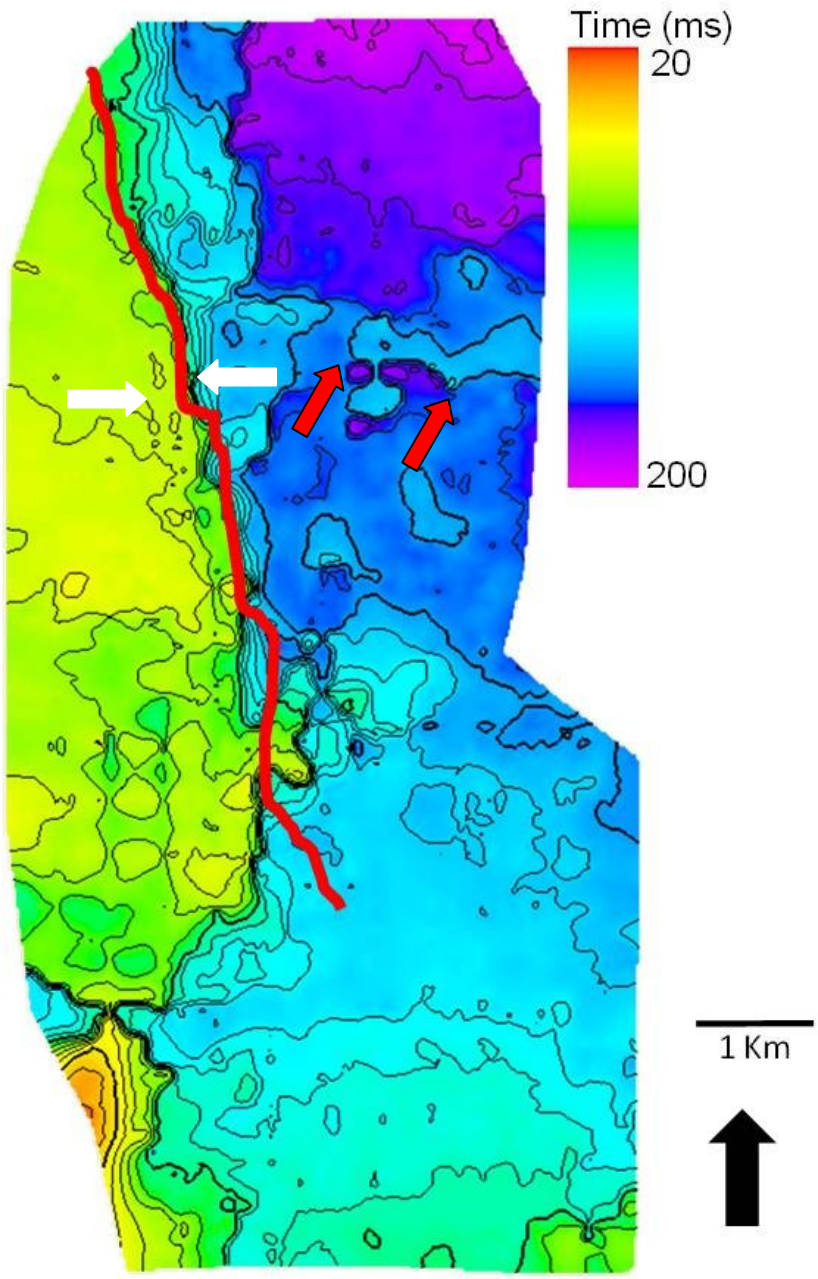

Figure 3.23 Thickness map between the Granite Wash and the Basement.

Interval contours are every 10 ms. Thicker sediments are located to the north east part (red arrows) and it is thin along the Fault #1's footwall (red line and white arrows).

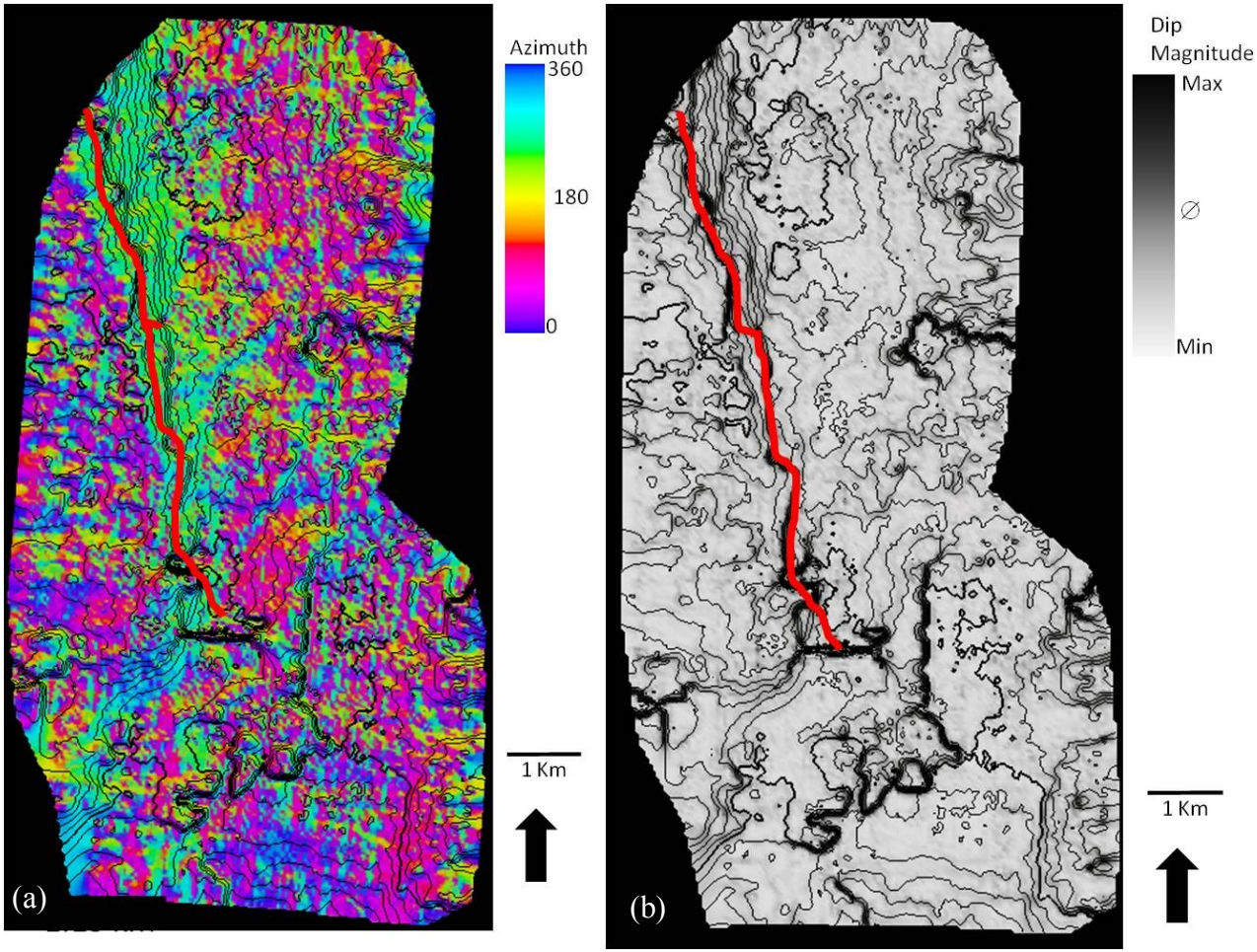

Figure 3.24 (a) Dip azimuth and (b) dip magnitude map at the top of the granite wash.

Fault # 1 represented with a red line.

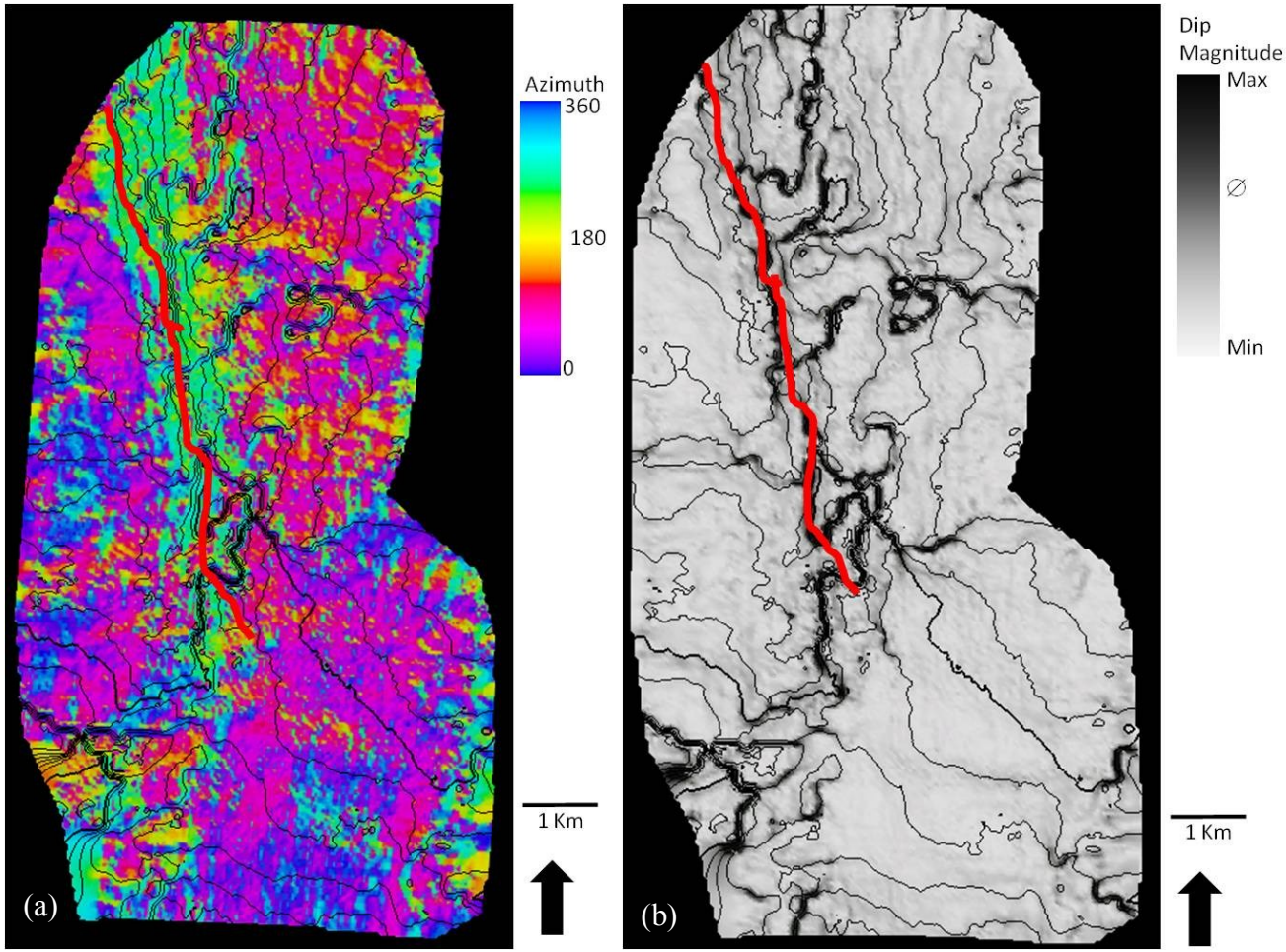

Figure 3.25 (a) Dip azimuth and (b) dip magnitude map at the bottom of the granite wash.

Fault # 1 represented with a red line.

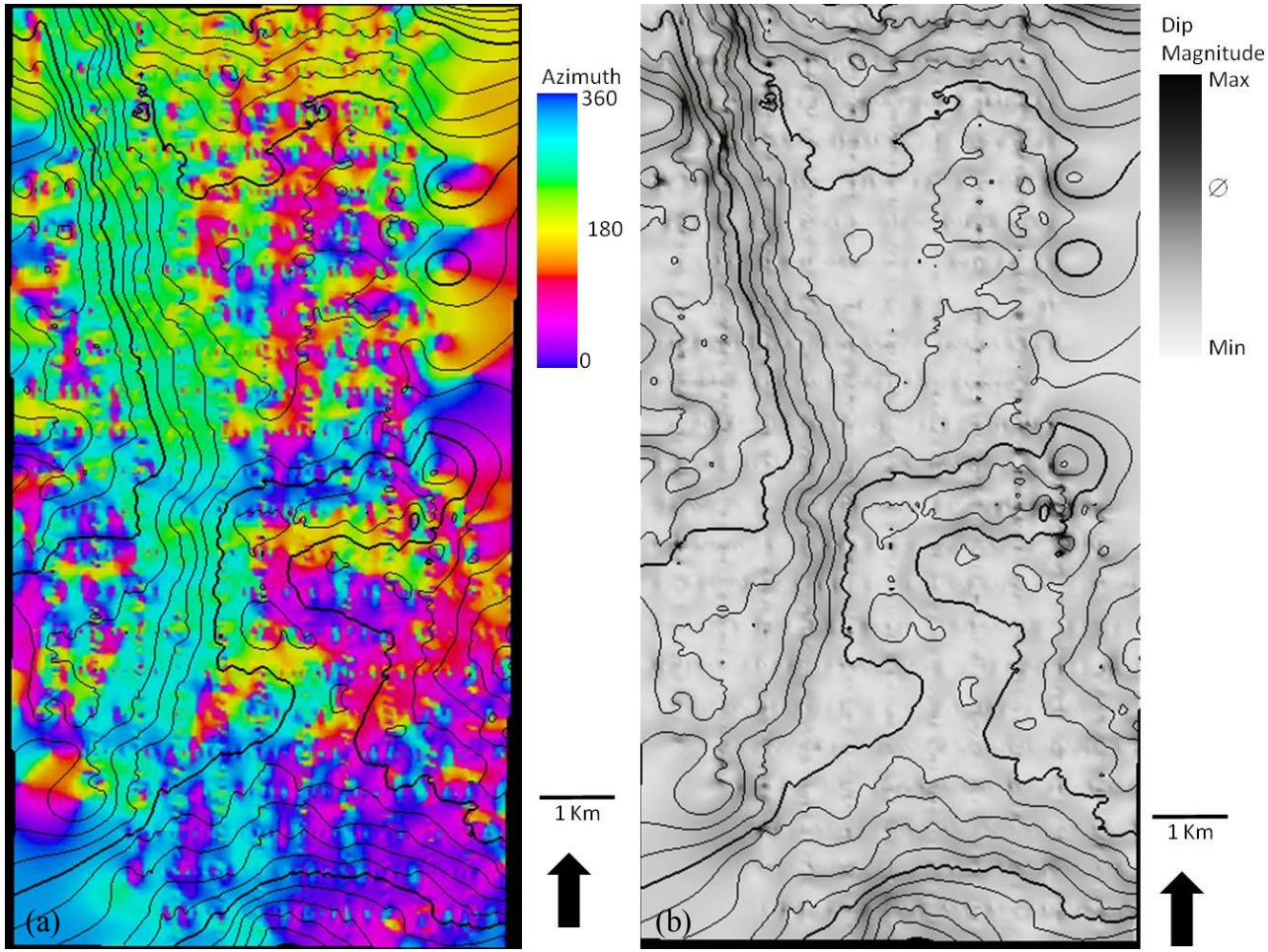

Figure 3.26 (a) Dip azimuth and (b) dip magnitude map at the brown dolomite horizon.

Multi-attributes display

Seismic attributes often enhance properties of the same geological features. While the interpretation of a single attribute can be ambiguous, combining multiple attributes into a single image provides a simple interactive means of highlighting intersecting anomalies of interest.

Seismic geomorphology uses a combination of seismic attributes, time slices, horizon slices, and stratal slices to map geologic features as they may have occurred at a particular instant in geologic time. Phantom-horizon slices are generated by first flattening a 100- to 200-ms slab of seismic data or attributes with respect to a picked horizon and then time slicing through the flattened slab. Even if the original horizon is a sequence boundary corresponding to a given instant in geologic time, shallower and deeper sequence boundaries are generally not parallel; thus, phantom horizons far from the original picked horizon cut formations of different ages. To avoid some of the limitations of phantom-horizon slices, Zeng et al. (1998 a,b) introduced the strata slice, whereby, the interpreter picks two sequence boundaries and generates slices that are proportional between them, thereby more nearly producing intermediate horizon slices that correspond to a single geologic instant in time.

The line AA' in the Figure 3.27 shows the strata slices generated between the top and bottom of the Granite Wash (color lines), Brown Dolomite (purple line), Top of Granite Wash (green line), Bottom of Granite Wash (light green line) and Basement (blue line). Also in Figure 3.27 the main fault (Fault #1) of this data set is shown (red line).

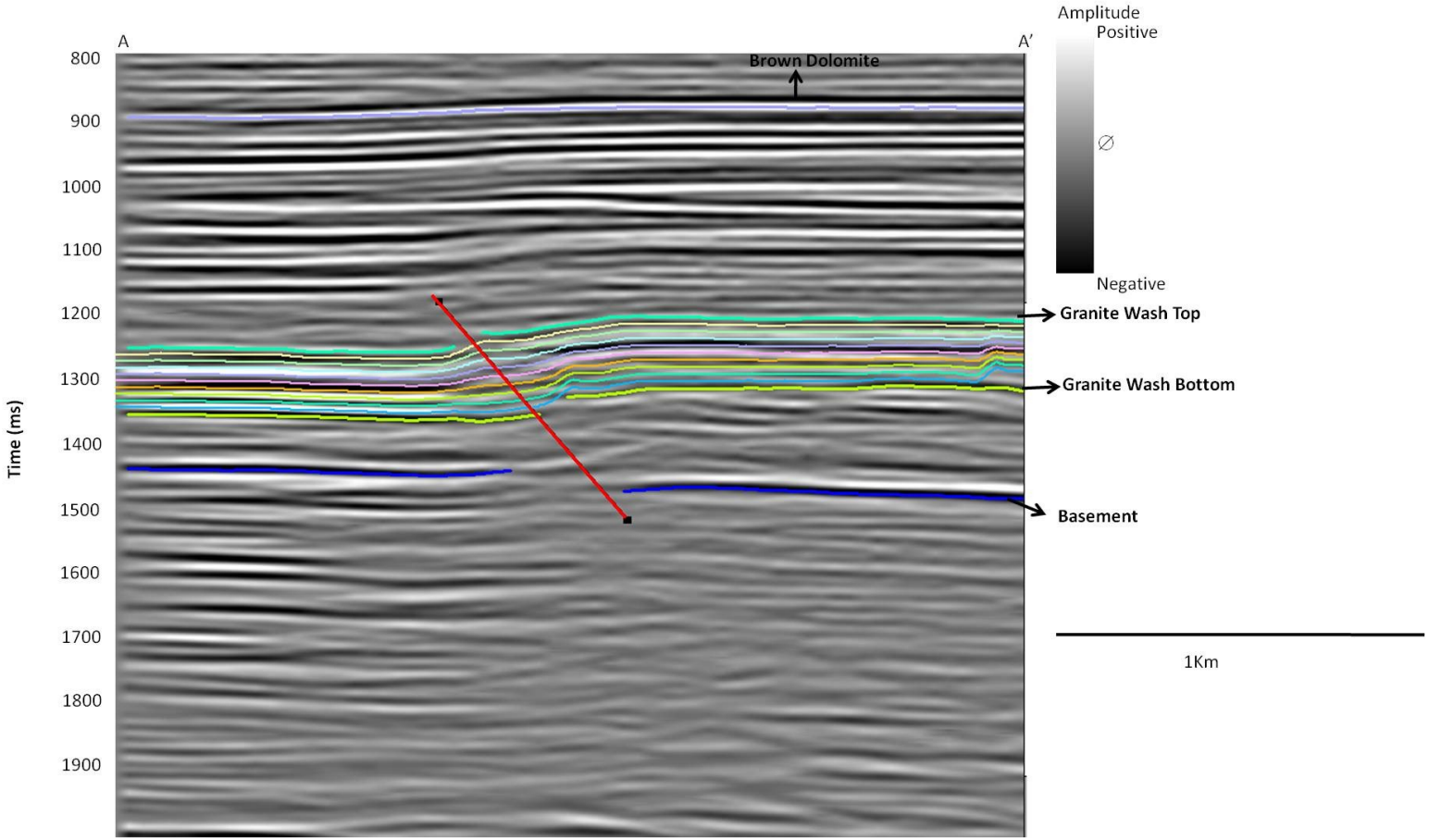

Figure 3.27 Stratal slice generated between the top and the bottom of the Granite Wash.

Figures 3.28 to 3.31 show a suite of stratal slices made between the top and the bottom of the Granite Wash interval within the Boomer Sooner data set. In these figures I co-rendered the coherent energy with the inline energy attribute, using transparency to define the fan deposit present in the granite wash interval.

As defined in Appendix A, the coherent energy provides the energy of coherent component of the complex traces within the analysis window, while the inline energy gradient is the horizontal derivative along the structure of the coherent energy.

Examining these stratal slices we see that the fan delta deposits occur in the south-east area at the bottom of the Granite Wash and move to shallower north-west part (red ellipses in Figures 3.28-3.31). The source of these Granite Wash deposits is the Bravo Dome located in the south and the structural nose that separates the Dalhart Basin from the Whittenburg Trough.

The footwall of the main thrust fault (red line) presented higher energy. The energy represented by this footwall is decreasing as we move shallower (black ellipses).

Figure 3.32 shows the multi-attributes maps with the most positive curvature (k_1), the most negative curvature (k_2) and the Sobel filter, the last two attributes with transparency effect. This attribute map was created to enhance the Fault #1 (red line) and made a better definition of its effect over the interpreted horizons.

Figure 3.29a shows the strata slice at 30 % of the time thickness between the top and the bottom of the Granite Wash horizons with the oil producer wells (black circles), closed oil producer wells (black square with black circle in the middle) and dry wells (white circles). Most of the oil producer wells and the closed oil producer wells are located in the high energy areas of the fan deposit, but the dry wells are located in the low energy zones. Based on this analysis in this specific stratal slice, the high energy represented in this strata slice can be associated with hydrocarbon saturation.

Figure 3.33 shows the multi-attributes map with the most positive curvature (k_1), the most negative curvature (k_2) and the Sobel filter, the last two attributes with transparency effect, at the basement horizon. The Fault #1 (red line) is characterized in this map, due to the correct seismic attribute.

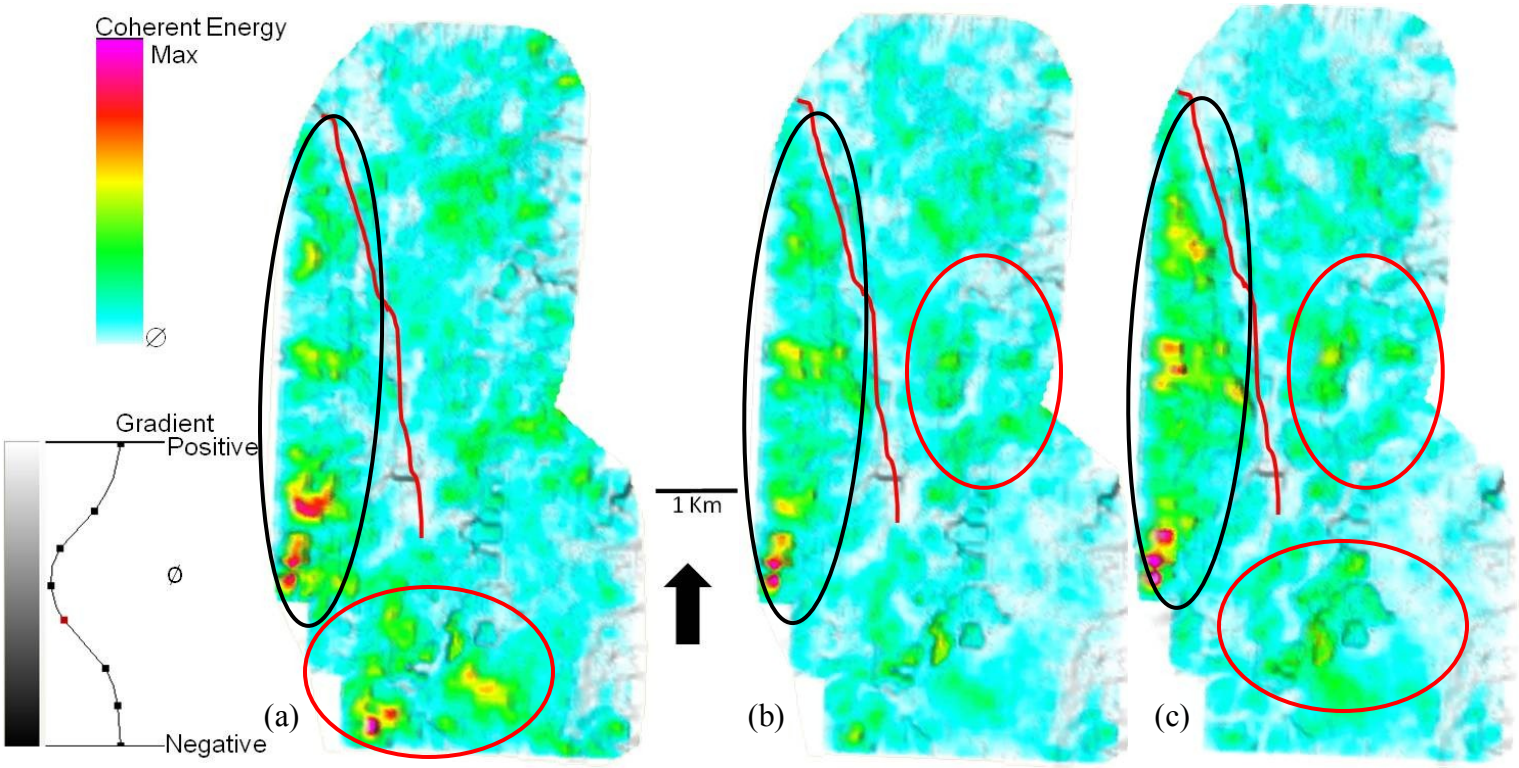

Figure 3.28 Stratal slices through the coherent energy co-rendered with the inline energy gradient volumes at (a) the top of the Granite Wash, (b) 10 % and (c) 20% of the time thickness between the top and the bottom of the Granite Wash horizons shown in Figure 3.27.

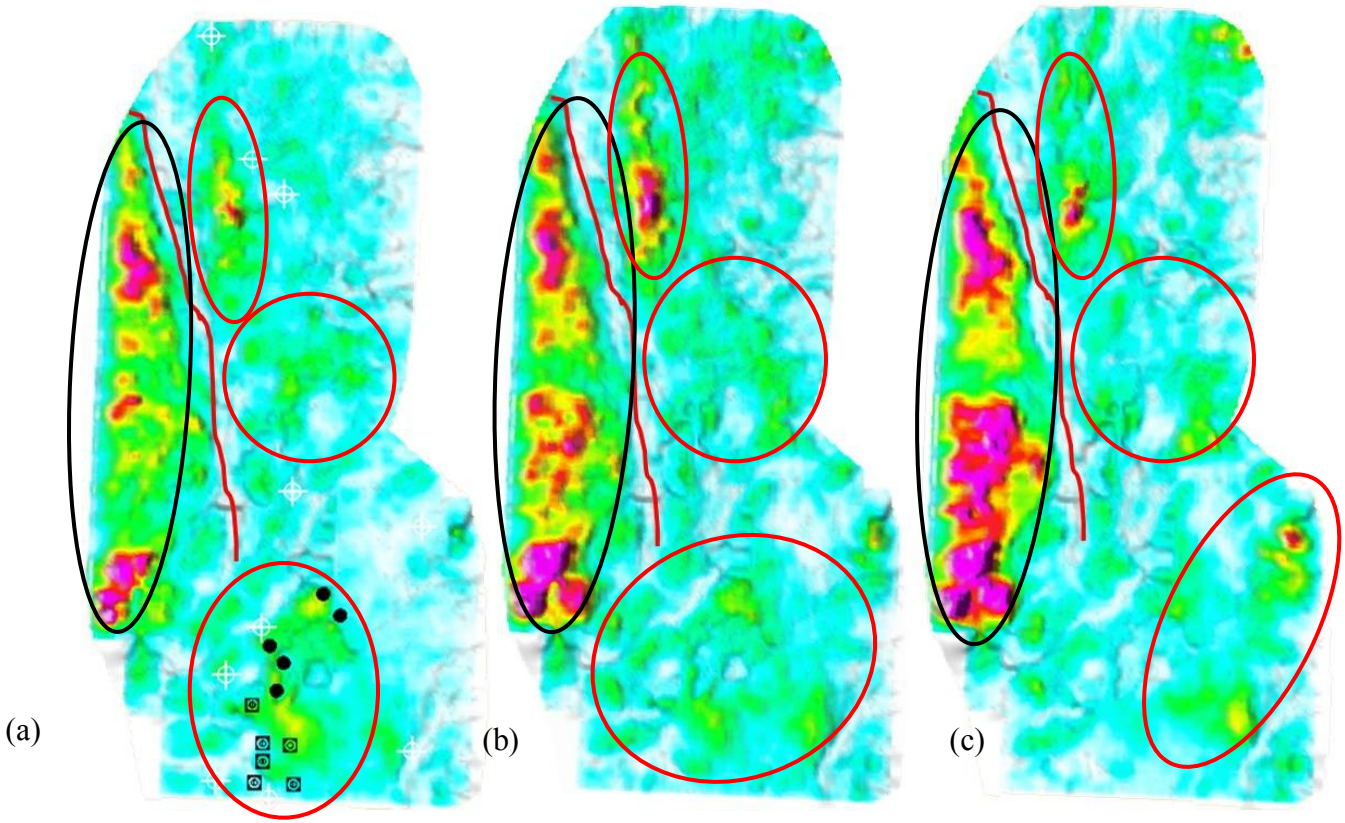

Figure 3.29 Stratal slices through the coherent energy co-rendered with the inline energy gradient volumes at (a) 30%, (b) 40 % and (c) 50% of the time thickness between the top and the bottom of the Granite Wash horizons shown in Figure 3.27.

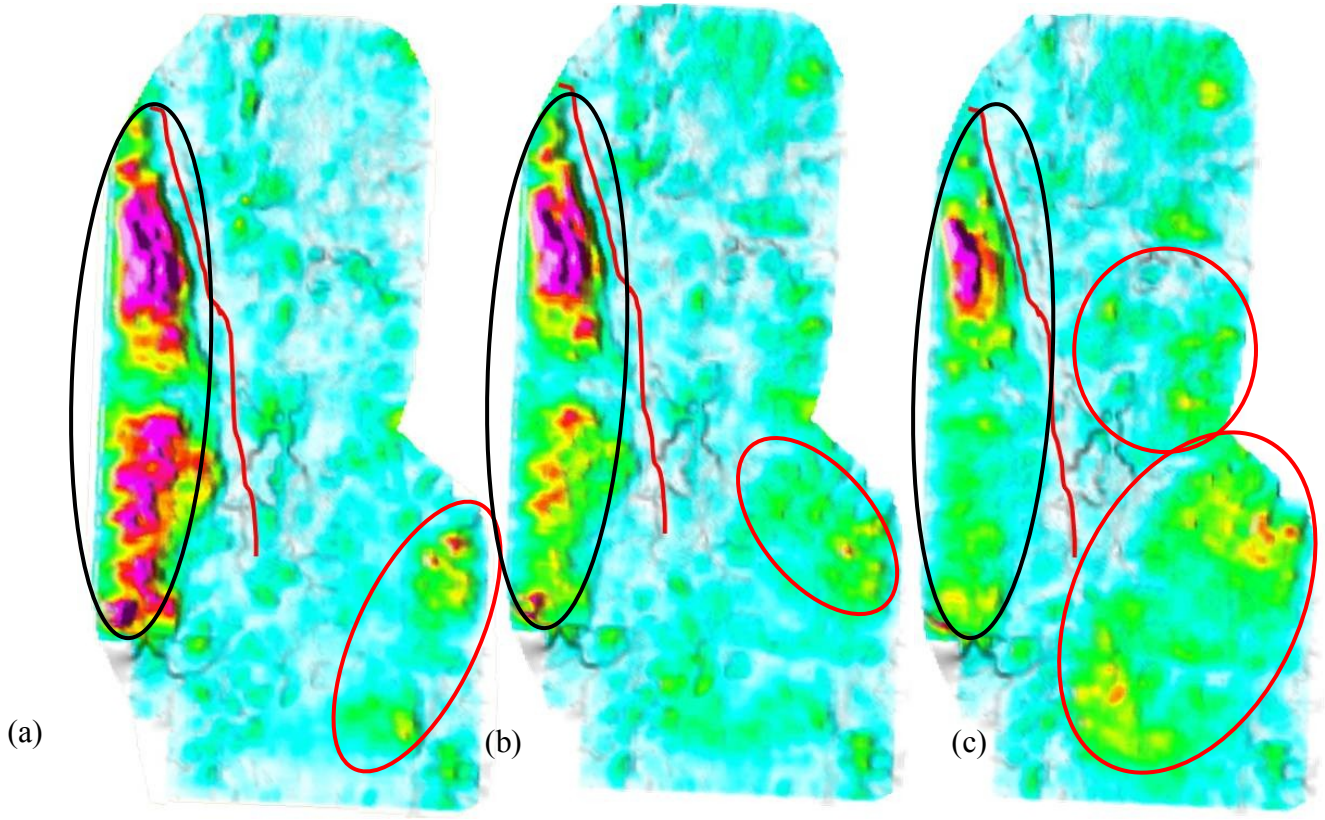

Figure 3.30 Stratal slices through the coherent energy co-rendered with the inline energy gradient volumes at (a) 60%, (b) 70 % and (c) 80% of the time thickness between the top and the bottom of the Granite Wash horizons shown in Figure 3.27.

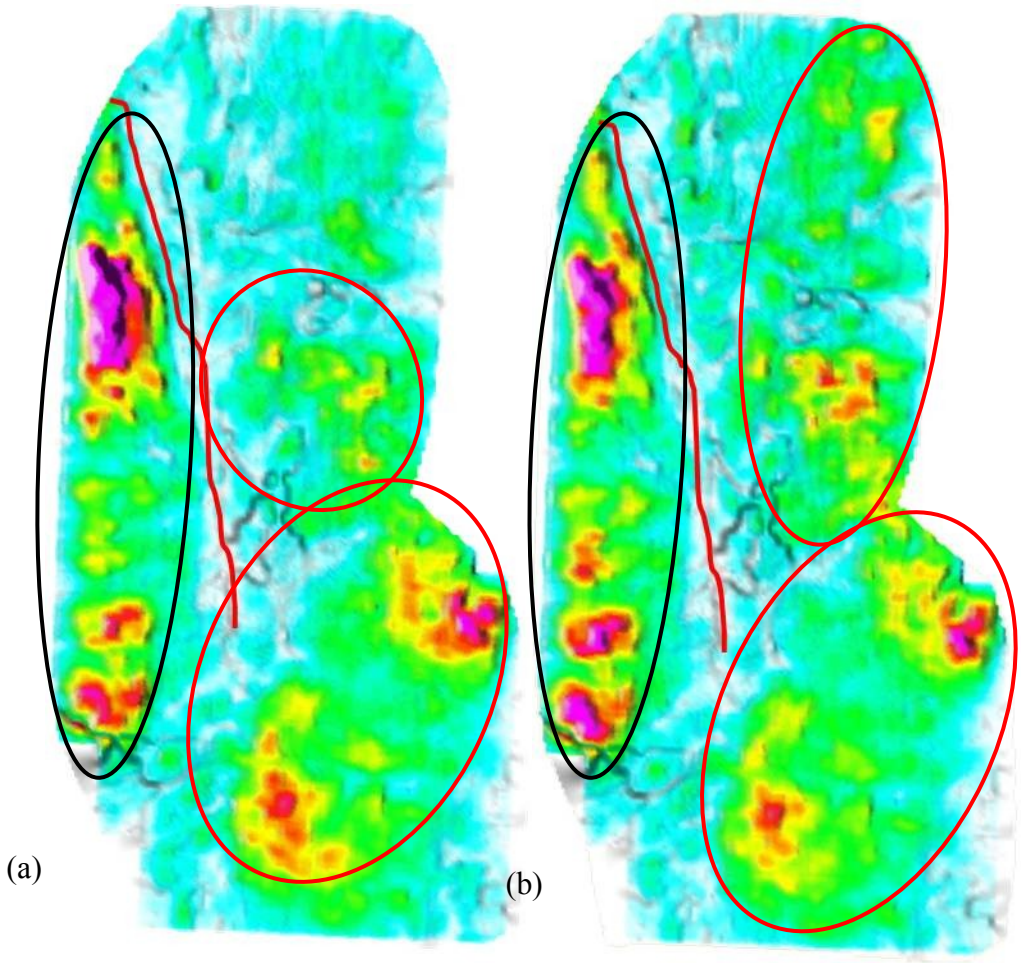

Figure 3.31 Stratal slices through the coherent energy co-rendered with the inline energy gradient volumes at (a) 90%, (b) the bottom of the Granite Wash of the time thickness between the top and the bottom of the Granite Wash horizons shown in Figure 3.27.

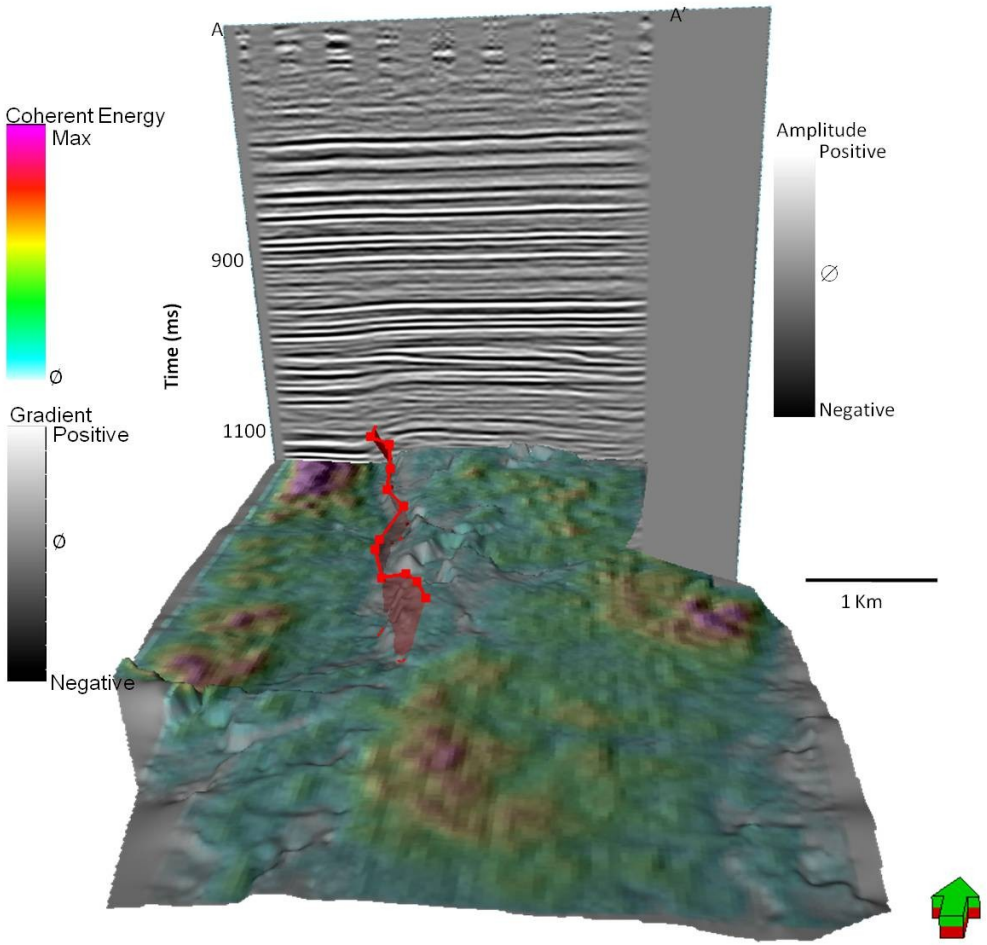

Figure 3.32 3D view of the stratal slices through the coherent energy co-rendered with the inline energy gradient volumes at 90 % of the time thickness between the top and the bottom of the Granite Wash horizons shown in Figure 3.27.

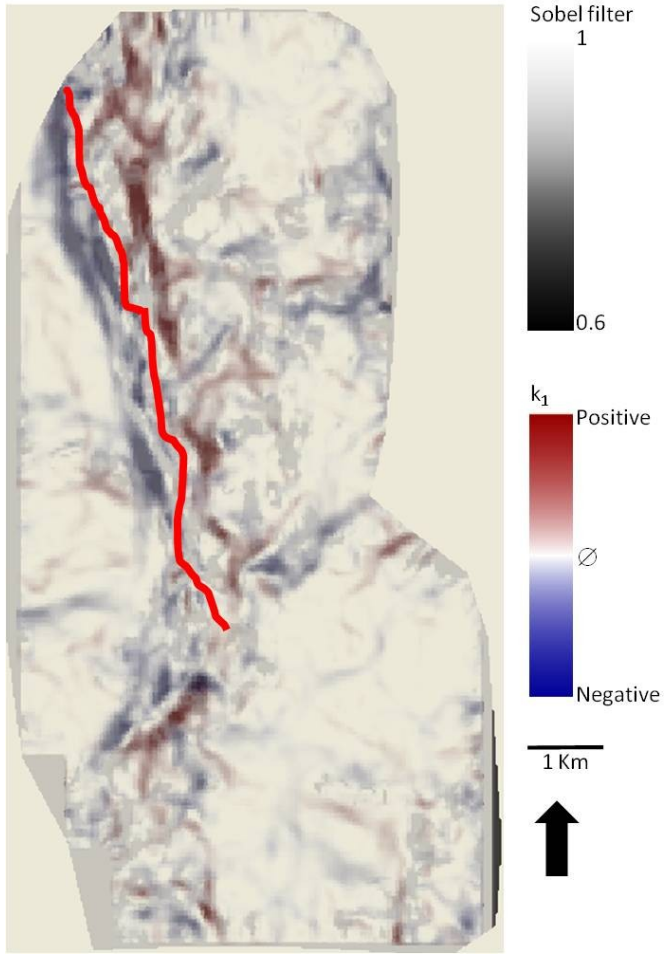

Figure 3.33 Most positive curvature, most negative curvature and sobel filter co-rendered at 70 % of the time thickness between the top and the bottom of the Granite Wash horizons shown in Figure 3.27.

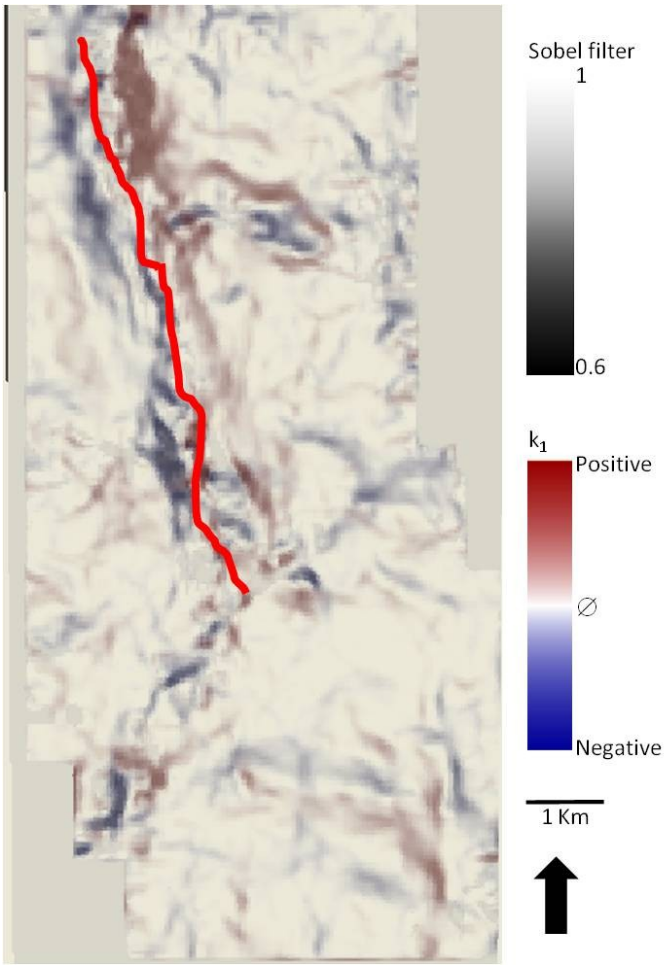

Figure 3.34 Most positive curvature, most negative curvature and Sobel filter co-rendered at the Basement horizon.

CHAPTER IV

SEISMIC INVERSION

Introduction

Russell (1988) defined geophysical inversion as mapping the physical structure and properties of the subsurface using measurements made on the surface of the earth. Inversion is a technique that creates a model of the earth using the seismic data as input.

The seismic inversion methods are summarized in Figure 4.1. Standard seismic processing workflows involve transforming CMP gathers into a stacked section, which approximates to the zero-offset reflection, in which the angle θ in Figure 4.2 is equal to zero (Russell, 2006).

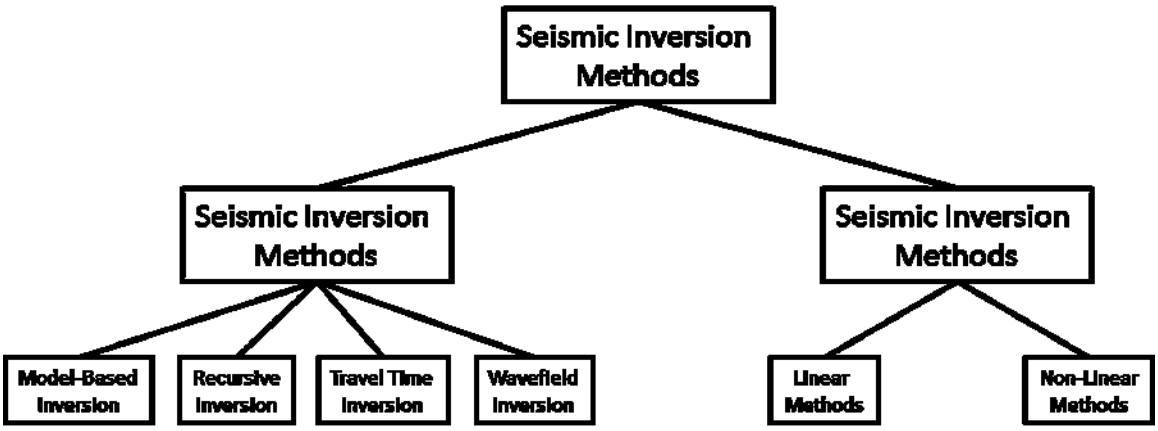

Figure 4.1 Summary of current seismic inversion techniques

(Russell, 1988)

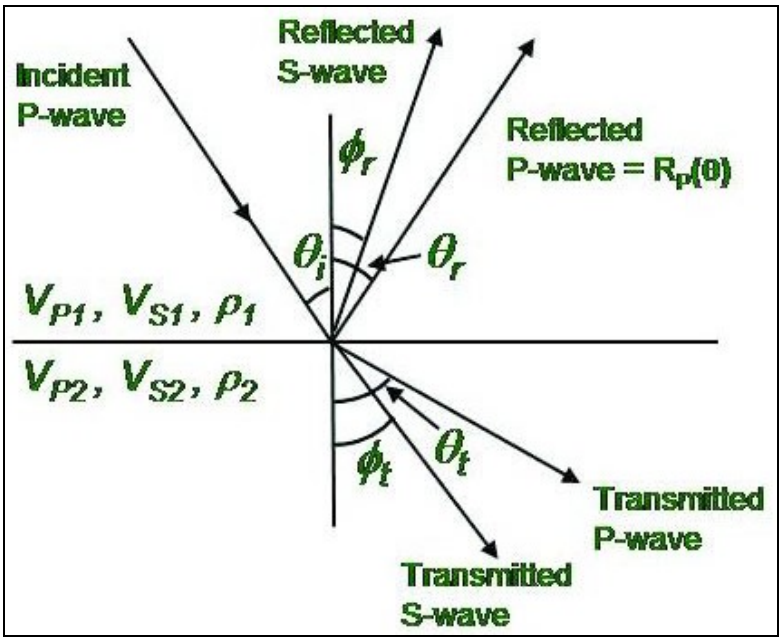

Figure 4.2 Mode conversion of an incident P-wave on an elastic boundary (Russell, 2006)

Acoustic Impedance inversion results

Wavelet Estimation

Figure 4.3 shows a synthetic seismogram constructed using the convolutional model. For normal incidence, the reflection coefficient was estimated directly from the compressional velocity and density logs. This figure shows eight panels for the generation of the synthetic seismogram for one of the five wells, corresponding to the resistivity log (panel 1), P-wave log (panel 2), density log (panel 3), impedance log (panel 4), corrected P-wave (panel 5), three equal synthetic seismogram traces in blue (panel 6), three composite traces extracted from the surface seismic data in red (panel 7), and the seismic data volume (panel 8). Notice that additional information such as the top and bottom of the Granite Wash well marker and the different interpreted horizons are

displayed. Once the reflection coefficients are calculated, the next step is to extract the seismic wavelet that when convolved with the reflectivity series best describes the energy that is recorded at the geophone.

The wavelet for this study is extracted statistically from the entire seismic volume. Due to dispersion between velocities measured at the synthetic trace is shifted, stretched and squeezed, by selecting points on the synthetic and tying it with corresponding points on the composite trace to yield a better correlation results.

By doing so, I was able to convolve my wavelet with the reflectivity series to obtain a correlation coefficient of 0.95. I repeated this synthetic seismogram generation procedure for the five wells with sonic logs in this survey, thereby generating accurate well ties subsequent time to depth conversion.

Acoustic Impedance Results

Wavelet extraction and synthetic seismogram generation are the first step in model-based acoustic impedance. Because the acoustic impedance volume generation is the objective, only compressional velocities logs (V_p) were used for the five wells along with the interpreted horizons corresponding to the key horizons: Brown Dolomite, top of the Granite Wash, bottom of the Granite Wash and the basement in stratigraphic order from younger to older. The reflection coefficients were extracted directly from the seismic traces and the wavelet used was the statistical wavelet common for all five wells.

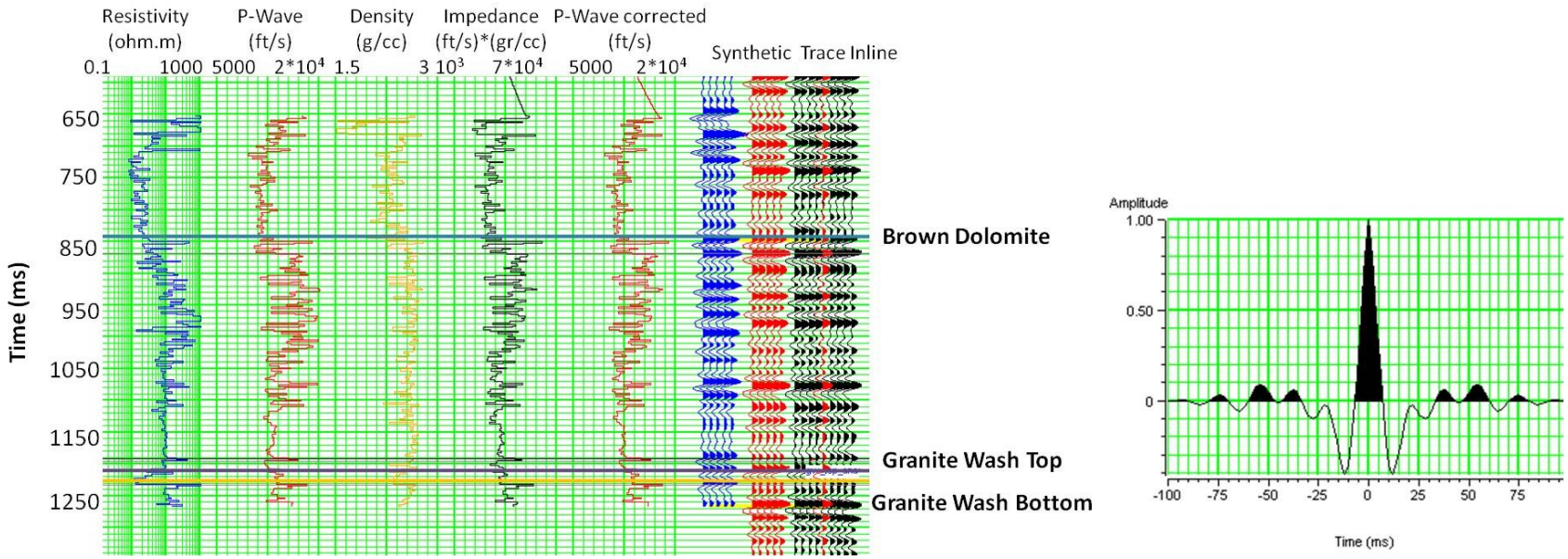

Figure 4.3 Normal incidence synthetic seismogram generation at well #123.

(a) Synthetic seismogram trace (in blue) using "full wavelet" shown in b, (b) wavelet extracted from the entire seismic volume.

In order to corroborate the results of the acoustic impedance inversion, the original acoustic impedance log was superimposed on the acoustic impedance log resulting from the inversion (Figure 4.4). As hoped, the impedance inversion closely approximates the well log impedance components that fall within the seismic bandwith.

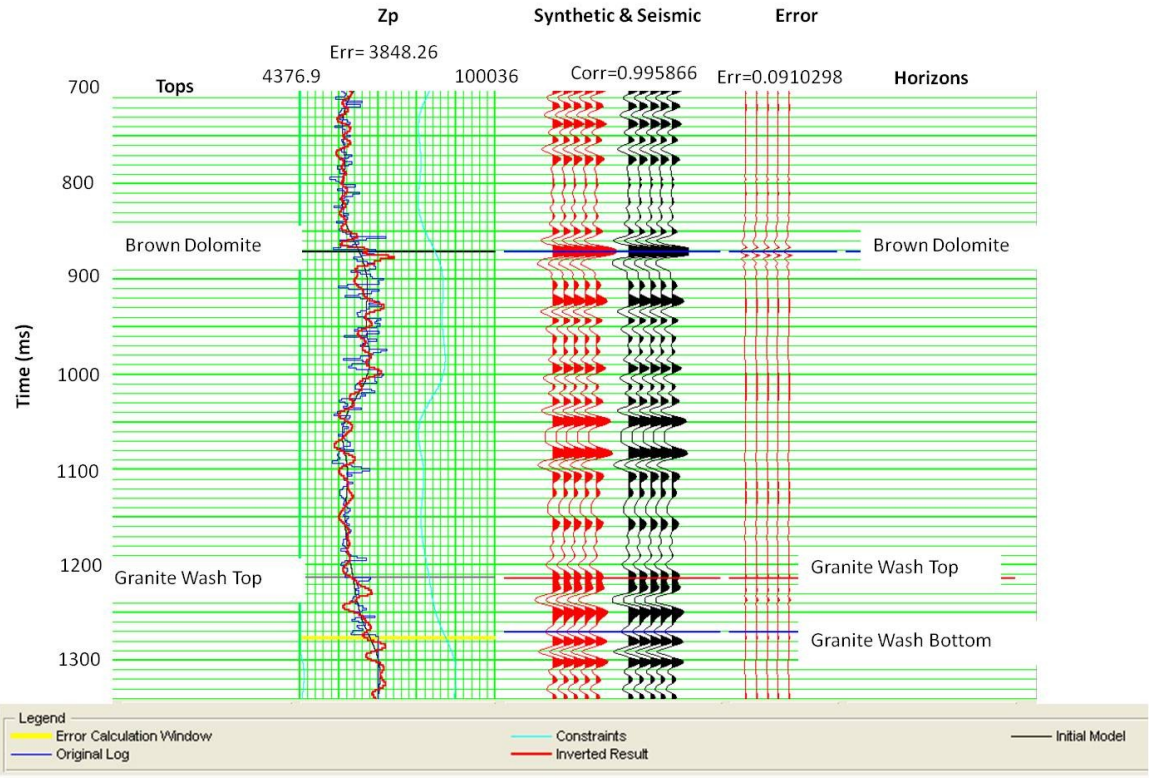

Figure 4.4 Analysis of results for acoustic impedance inversion at the well # 128.

Acoustic impedance not only defines the edges of the Granite Wash deposit but also differentiates zones within the Granite Wash deposit (Figure 4.5). Figure 4.6 shows that the low acoustic impedance zone is correlated with the high resistivity zone at well #123.

Line AA' in Figure 4.7 shows the Brown Dolomite horizon (red line at the top), top of the Granite Wash horizon (orange line), bottom of the Granite Wash (black line), basement horizon (blue line), fault #1 (red line) and the stratal slice through the acoustic impedance at 50% and 40 % of the time thickness between the top and the bottom of the Granite Wash horizons. Note anomalously low acoustic impedance between the stratal slice of 50% and 40 % of the time thickness between the top and the bottom of the Granite Wash horizons (red ellipse).

Figure 4.8 the stratal slice through the acoustic impedance at 40 % of the time thickness between the top and the bottom of the Granite Wash horizons seen on the logs shows good correlation between the producer wells and the low acoustic impedance.

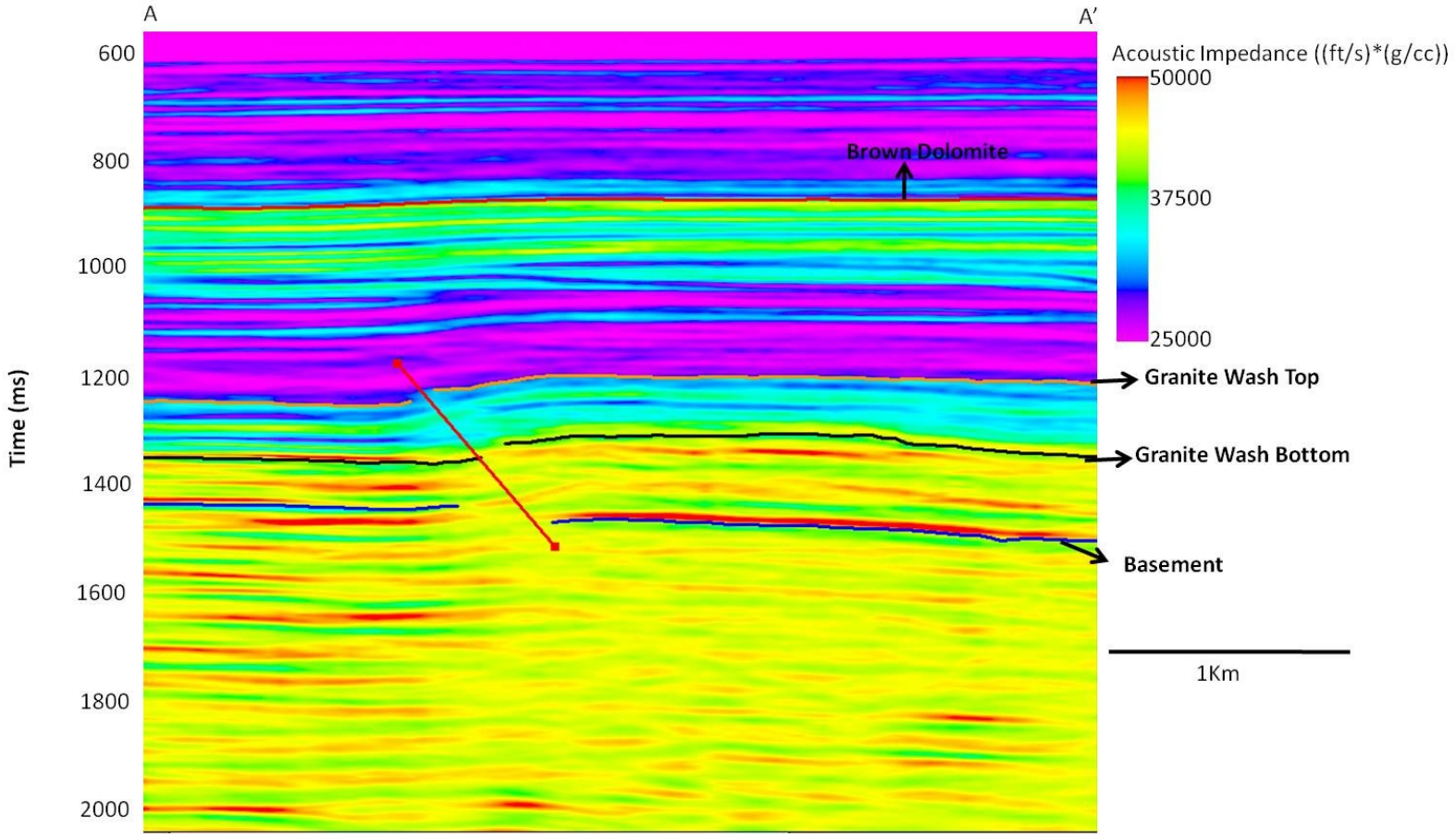

Figure 4.5 Line AA' within the acoustic impedance volume showing the Brown Dolomite horizon (red line at the top), top of the Granite Wash horizon (orange line), bottom of the Granite Wash (black line), basement horizon (blue line) and fault #1 (red line).

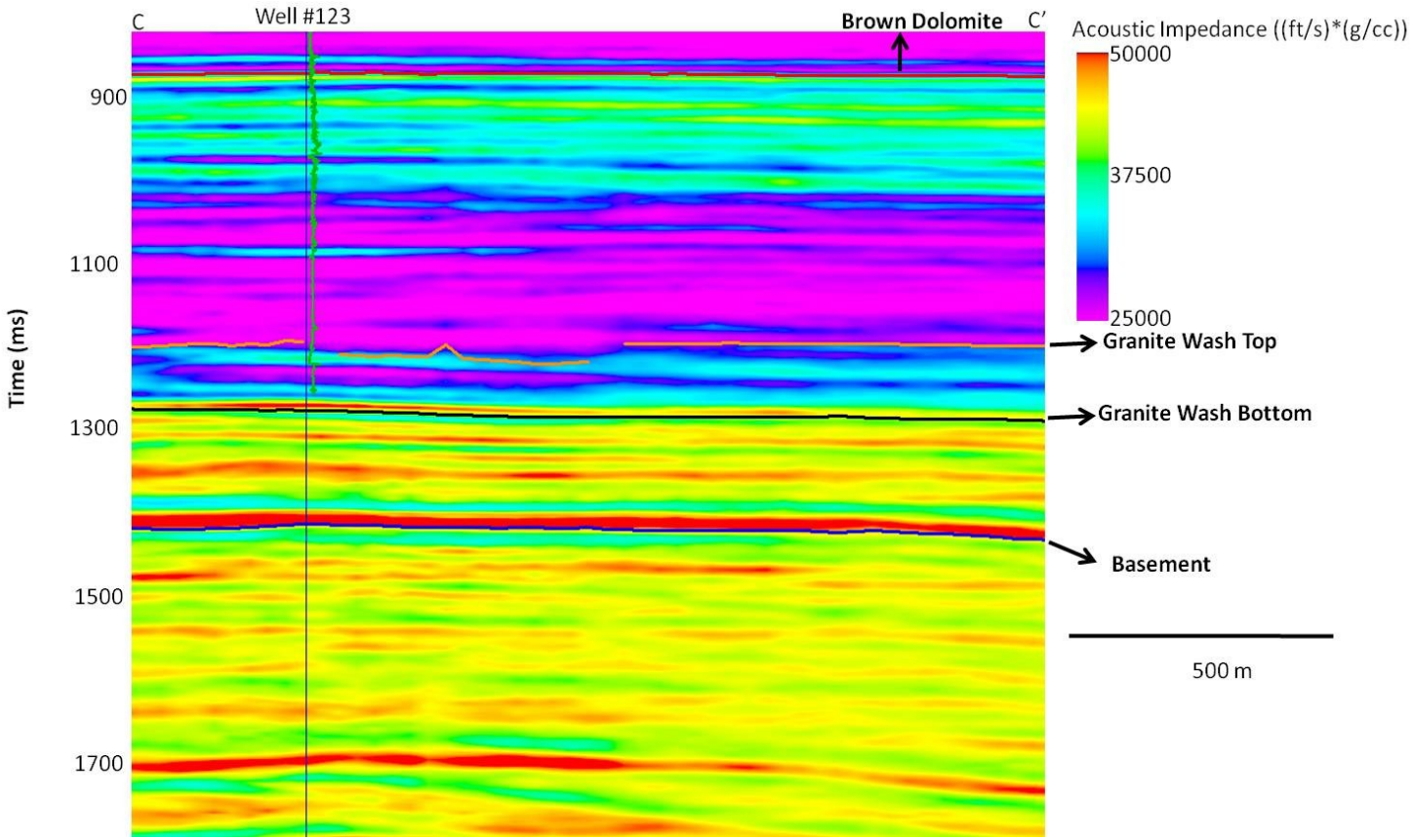

Figure 4.6 Line CC' within the acoustic impedance volume showing the Brown Dolomite horizon (red line), top of the Granite Wash horizon (orange line), bottom of the Granite Wash (black line), basement horizon (blue line), and the resistivity log at well #123.

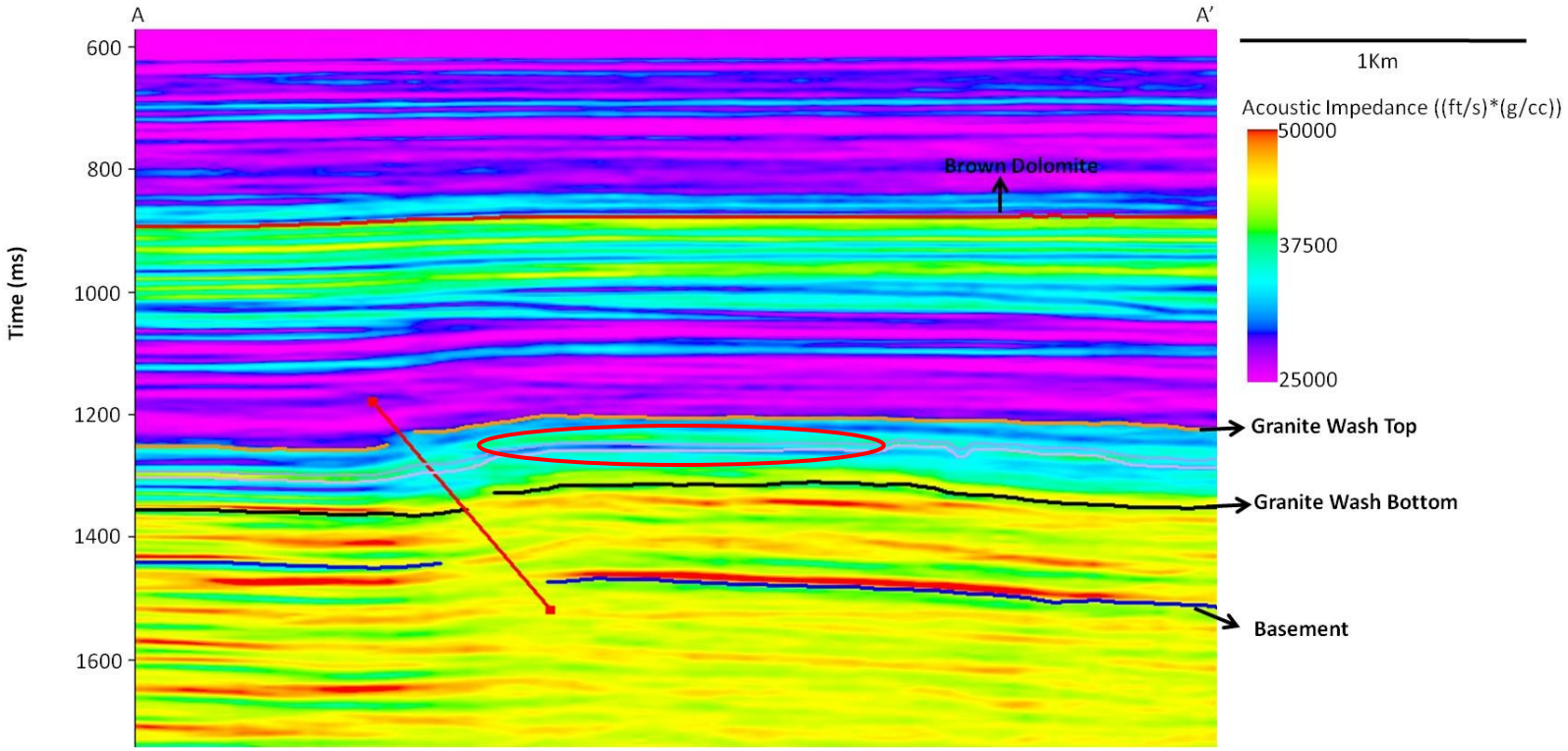

Figure 4.7 Line AA' within the acoustic impedance volume showing the Brown Dolomite horizon (red line at the top), top of the Granite Wash horizon (orange line), bottom of the Granite Wash (black line), basement horizon (blue line), fault #1 (red line) and the stratal slice of 50% and 40 % of the time thickness between the top and the bottom of the Granite Wash horizons.

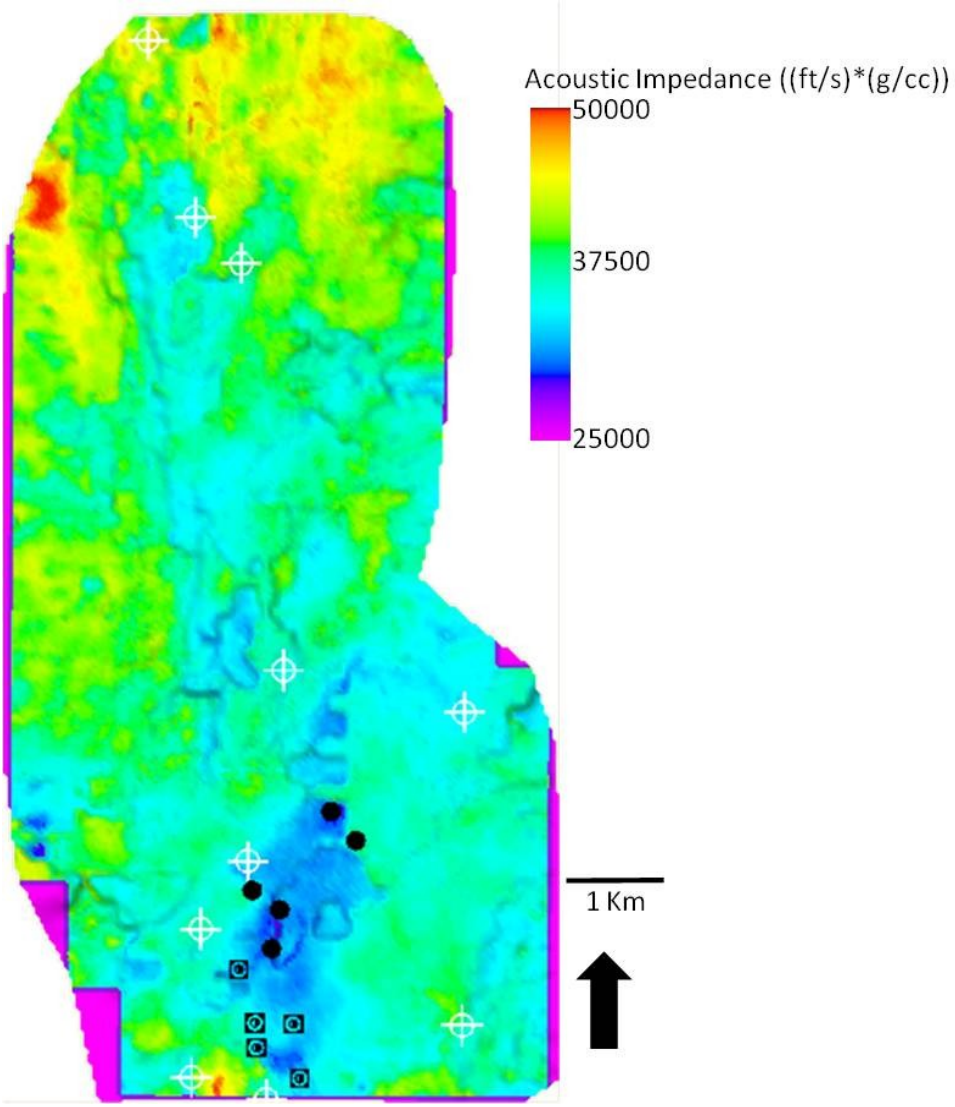

Figure 4.8 Stratal slice through the acoustic impedance at 40 % of the time thickness between the top and the bottom of the Granite Wash horizons.

CHAPTER V

DISCUSSIONS

Using a variety of attributes over the Boomer Sooner survey makes it possible to better define the main thrust fault, which is cuts the Granite Wash interval and the basement. The fan deposit system present in the Granite Wash interval was better delineated with the multi-attributes interpretation workflow.

It is clear that integration of the interpretation derived from different attributes is necessary in order to better understand the morphology of the fan deposit system within the Granite Wash. Figure 5.1 shows a compilation of four of the results discussed earlier showing the differences among them, but resulting in better definition of the Granite Wash's morphology.

The time-structure maps at the top and bottom of the Granite Wash (Figures 5.1a and b) show a structural high trending north-south, which represents the nose with separates the Dalhart basin from the Whittenburg Trough, and the sediments of the fan deposit associated with the Granite Wash in this area. Coherent energy and its gradients (Figure 5.1c) delineated in the Granite, which consistently shows high amplitude anomalies on the footwall of Fault #1, as well as on the north-east part of the survey, which is related to the fan deposit of the Granite Wash. The thickness map of the Granite Wash deposit (Figure 5.1d) shows that the thicker sediments are located in the north-east

part of the study area related to the fan deposit location, as well as along Fault #1 (red line).

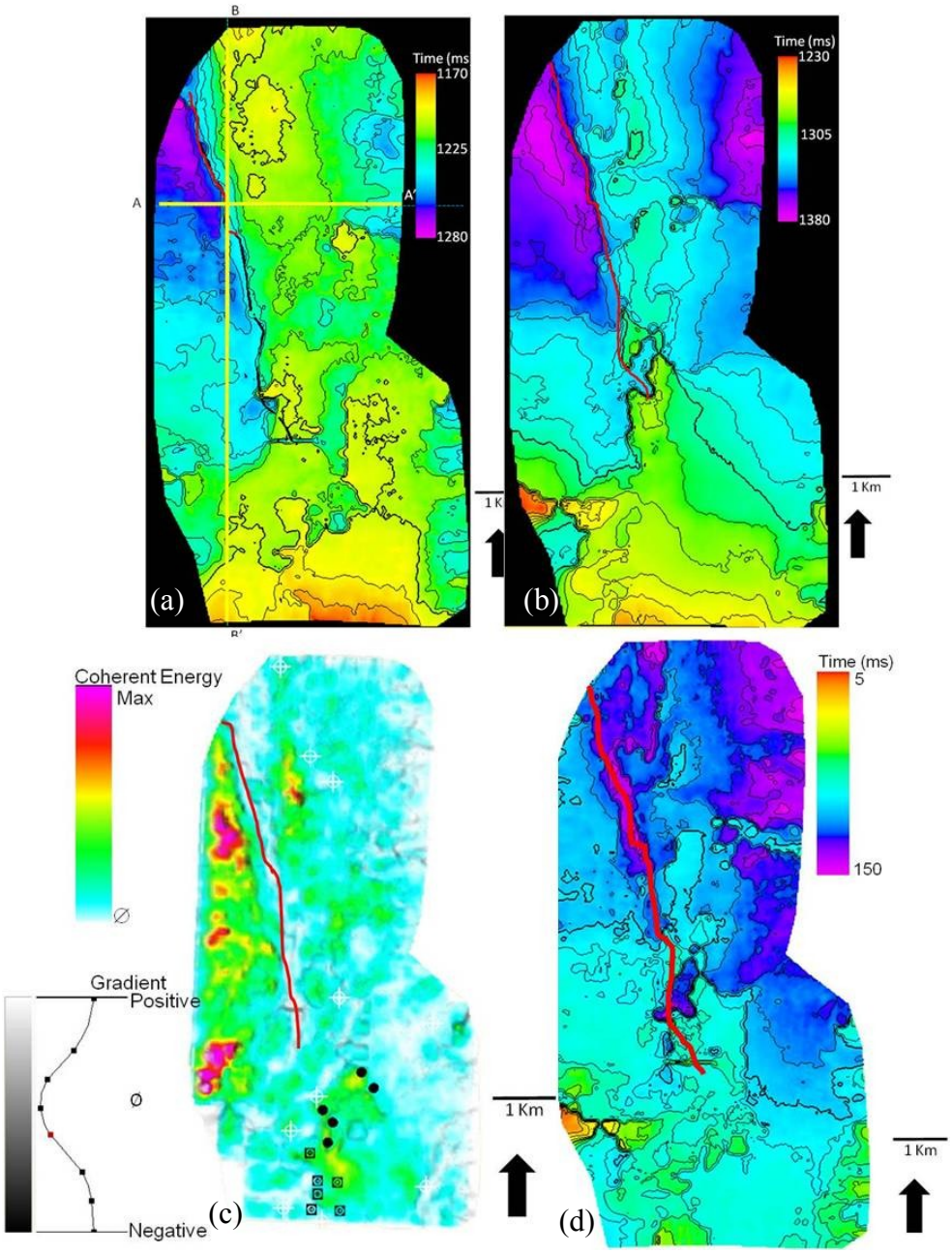

Figure 5.1 Compilation of seismic interpretation over the Granite Wash deposit.

(a) Time-structure at the top of Granite Wash horizon, (b) time-structure at the bottom of the Granite Wash horizon, (c) stratal slices through the coherent energy co-rendered with

the inline energy gradient volumes at 40% of the time thickness between the top and the bottom of the Granite Wash horizons and (d) thickness map of the Granite Wash deposit.

Based on previous work in this area and on my seismic interpretation, I interpret the the Granite Wash along the footwall of the Fault #1 could be a reservoir sliced into segments by secondary faults forming a potential trap (Figure 5.2).

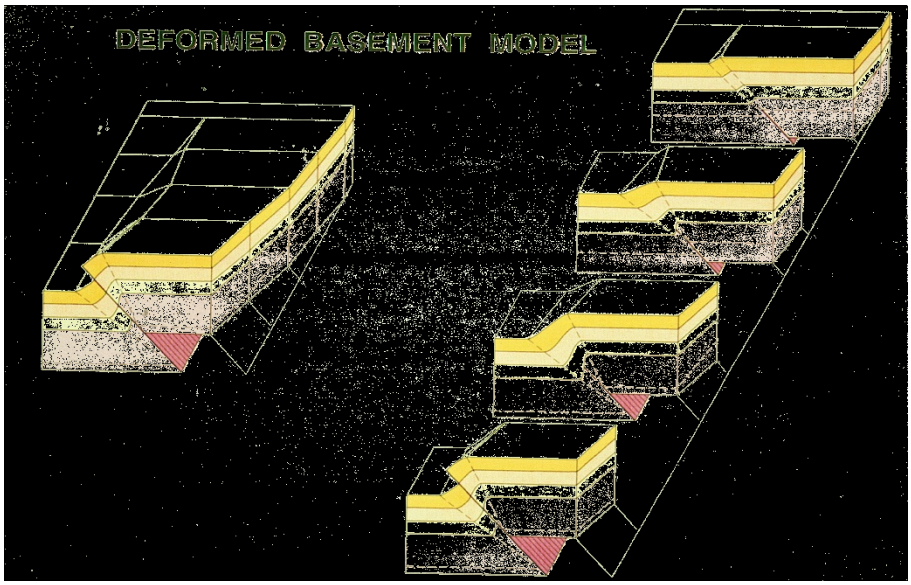

Figure 5.2 Structural traps models.

(Mitra, 2009)

In interpret the basement to be initially cut by a normal fault. The sediments were deposited creating a difference between the amount of sediments present in the footwall and the hanging wall. (Figure 5.3) During the Pennsylvanian, this normal fault was reactivated as a thrust fault that is affecting the Granite Wash deposit and the basement (Figure 5.4).

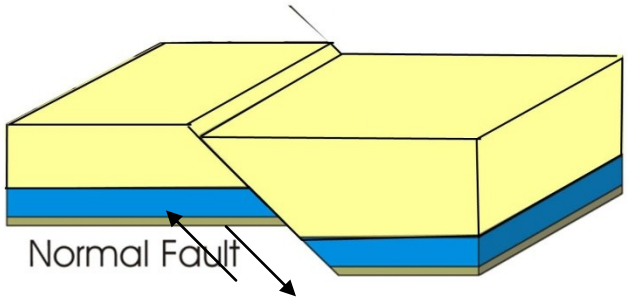

Figure 5.3 Normal fault diagrams showing syntectonic deposition.

(Mitra, 2009)

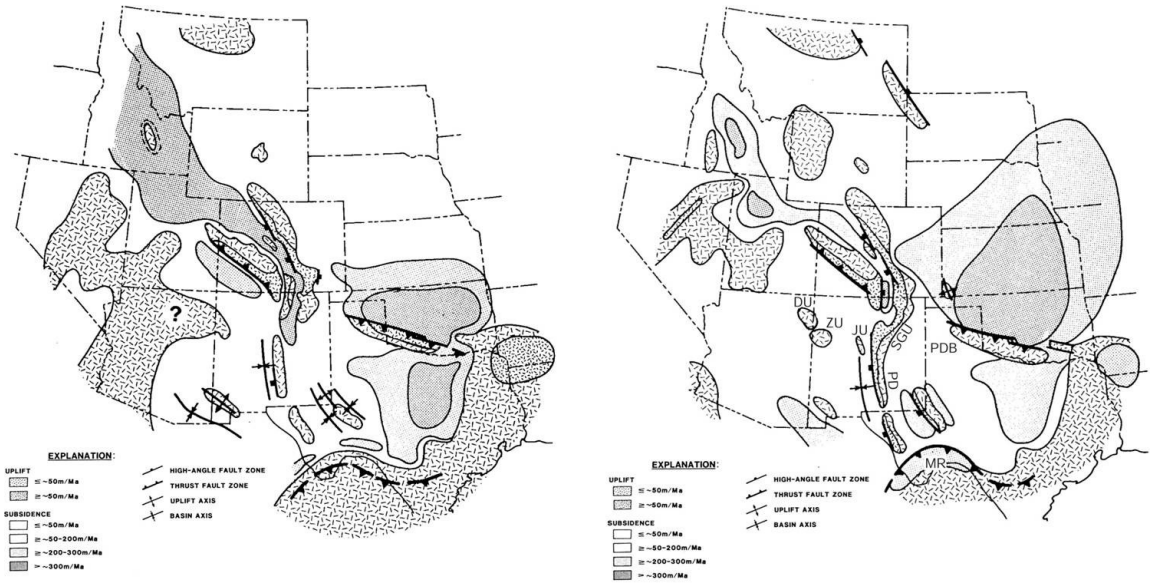

(a) Middle and Late Pennsylvanian (b) Late Pennsylvanian and Early Permian

Figure 5.4 (a) During middle to late Pennsylvanian time, there was subdued activity within the Ouachita region marking the waning of the orogeny. (b) The Late Pennsylvanian and early Permian marked continued thrusting in the Marathon region although lesser to the east near the Ouachita front, with gradually decreasing deformation within the foreland of the southwestern United States.

(Modified from Kluth, 1986, originally modified from McKee and Crosby, 1975).

Acoustic impedance further delineated the fan deposits related with the Granite Wash. Lateral and horizontal variation of impedance may be sensitive to fluids as well as lithological changes in the Granite Wash deposit.

Line AA' in the Figure 5.2a shows that the low acoustic impedance is related to the area between the stratal slice of 50% and 40 % of the time thickness between the top and the bottom of the Granite Wash horizons. The stratal slice through the acoustic impedance at 40 % of the time thickness between the top and the bottom of the Granite Wash horizons (Figure 5.2b) shows good correlation between the producer wells and the low acoustic impedance.

Figure 5.3 shows the stratal slice through the acoustic impedance at 60 % and 20% of the time thickness between the top and the bottom of the Granite Wash horizons. In both strata slices the acoustic impedance is low in the footwall of the fault #1 (red line). The acoustic impedance possibly can be related to the presence of oil to increased porosity, or both.

A geobody is a 3D object extracted from a seismic volume. The main objective of this geobody is to identify, isolate, extract and make a discreet object from the seismic data. I applied this geobody technique over the coherent energy attribute and over the acoustic impedance volume generated within the Boomer Sooner survey.

Figure 5.4 shows the geobodies created over the coherent energy volume and over the acoustic impedance volume. In this figure I observe that the producer wells (white circles) and the closed oil producer wells (white squares with black circles in the middle) are closely related with the low impedance areas more than the high coherent energy area. This relationship corroborates the possibility that the low acoustic impedance can be related to the differences in fluid present within the Granite Wash deposit. Also, these low acoustic impedance values possibly can be related to the location of the fan deposits. The dry wells (white circle with a cross) do not fall within the low acoustic impedance zones.

Risk Analysis

Exploration and production of hydrocarbons is a high-risk venture. Geological concepts are assigned an uncertain (Pg) with respect to structure, timing, source, reservoir seal, and hydrocarbon charge. On the other hand, economic evaluations have uncertainties related to costs, probability of finding and producing economically viable reservoirs, technology and oil price.

Even at the development and production stage the engineering parameters embody a high level of uncertainties in relation to their critical variables (infrastructure, production schedule, quality of oil, operational costs, reservoir characteristics etc.). These uncertainties originate with geological models and are subsequentlycoupled with economic and engineering models to guided high-risk decisions, with no guarantee of successfully discovering and developing hydrocarbons resources.

Figure 5.12 shows the three prospects that I found in the study area, based in the seismic interpretation that I showed before. Table 5.1 shows the probability of geological success, for the three different prospects.

	Ptrap	Preservoir	Pseal	Psource	Ptiming	Pg
Area I	0.9	0.9	0.9	0.9	0.9	59%
Area II	0.9	0.8	0.7	0.6	0.7	21%
Area III	0.6	0.6	0.6	0.6	0.6	8%

Table 5.1 Probability of geological success over the study area.

Volumetric Calculations

Oil in place is the total hydrocarbon content of an oil reservoir and is often abbreviated STOOIP, which stands for 'Stock Tank Original Oil In Place', or STOIIP for 'Stock Tank Oil Initially In Place', referring to the oil in place before the commencement of production. In this case, *stock tank* refers to the storage vessel (often purely notional) containing the oil after production.

The STOOIIP is achieving using the equation:

$$STOIIP = \frac{(Area * thickness * porosity * oil\ saturation * 7758)}{Formation\ Volume\ Factor}$$

And the recoverable is calculated using the following equation:

$$Recoverable = \frac{STOIIP}{Recovery\ Factor}$$

I calculated the STOIIP and the recoverable for the three different prospects and the results are shown in the table 5.2

	Area I producer wells (P90)	Area II hanging wall (P50)	Area III footwall (P10)
Area (acres)	116.31	510.05	801.16
Thickness (ft)	10.00	10.00	10.00
Porosity (%)	20%	20%	20%
Oil Saturation (%)	50%	50%	50%
Formation Volume Factor (FVF)	1.40	1.40	1.40
Recovery Factor (%)	20%	20%	20%
STOIIP (bbls)	644,517.50	2,826,411.18	4,439,554.29
Recoverable (bbls)	128,903.50	565,282.24	887,910.86

Table 5.2 Deterministic volumetric calculation over the study area

The risk analysis process is based in two steps; the first one is the evaluation of probability of geology success (Pg). If this probability reaches a threshold then the second step is the economical evaluation base on the Net Present Value (NPV) of the prospect. The workflow that is the base of the risk analysis is shown in Figure 5.13.

Table 5.3 shows the average oil price, daily production in each well, number of well necessary to produce the area, oil production per year, and the recoverable volume of each prospect.

Table 5.4 shows the initial investment and the cash maintenance expenses that have to be invested to maintain the production.

Table 5.5 shows the Net Present Value (NPV) of the three different prospects in the area of study, all of them are positive. Based on the Pg and the NPV of the three prospects I can conclude that all of this prospect can be a good option to develop.

Average Oil Price ($/bbls)	bbl/d (1 well)	Numbers of well	Oil production per year (bbls)	Prospect	Recoverable (bbls)	Years of production
$ 60.00	20.00	5.00	36,500.00	**Area I**	128,903.50	4
				Area II	565,282.24	15
				Area III	887,910.86	24

Table 5.3 Parameters to calculate the Net Present Value (NPV).

Cash maintaince expenses (Annualy)	$	(766,500.00)	**Net Cost Value (NCV)**
Well development (Initial Investment)	$	(3,622,300.00)	
Cash Flow per year	$	2,190,000.00	
Interest rate (%)		10%	

Table 5.4 Net Cost Value (NCV).

Net Present Value Area I	$4,575,670.40
Net Present Value Area II	$7,204,954.18
Net Present Value Area III	$9,167,483.11

Table 5.5 Net Present Value (NPV) of three prospects under the area of study.

.

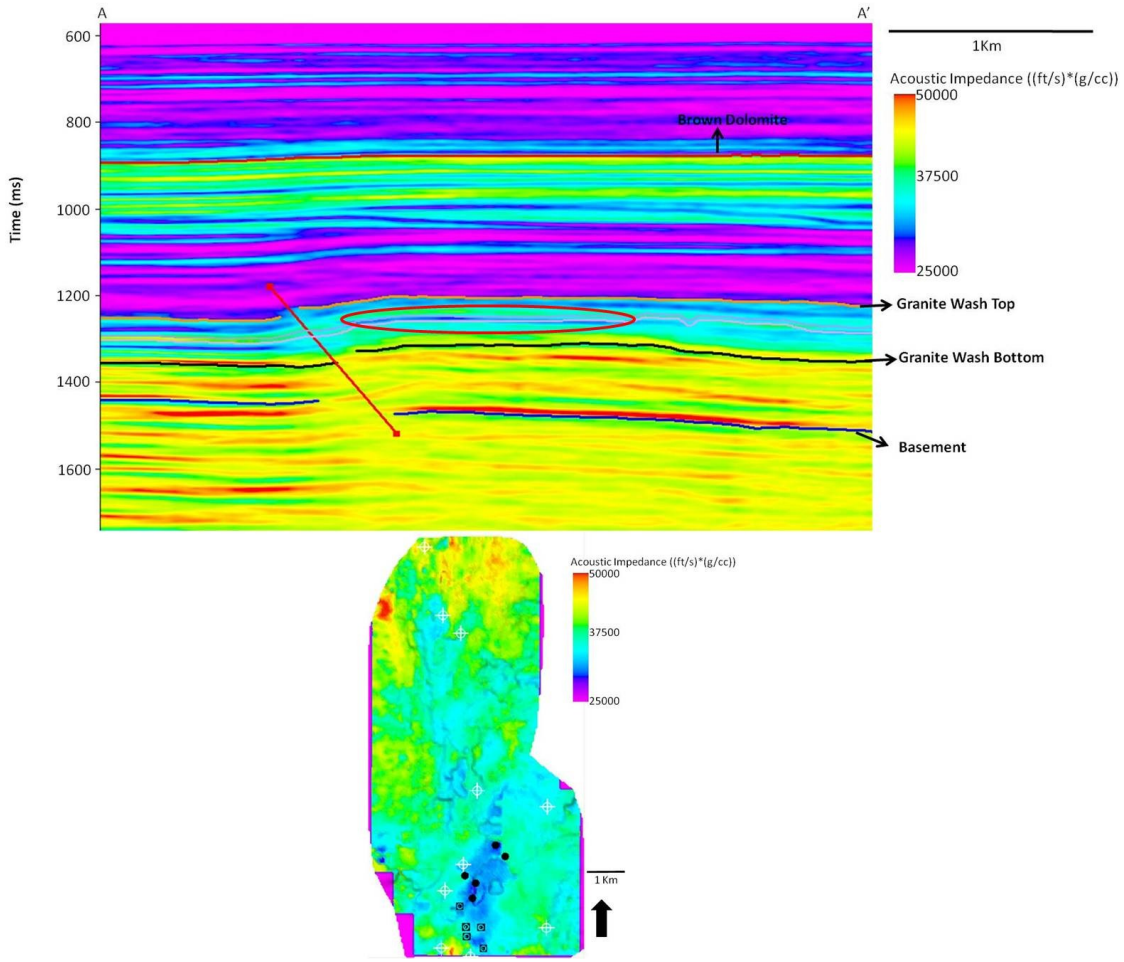

Figure 5.2 (a) Line AA' within the acoustic impedance volume. (b) Stratal slice through the acoustic impedance at 40 % of the time thickness between the top and the bottom of the Granite Wash horizons.

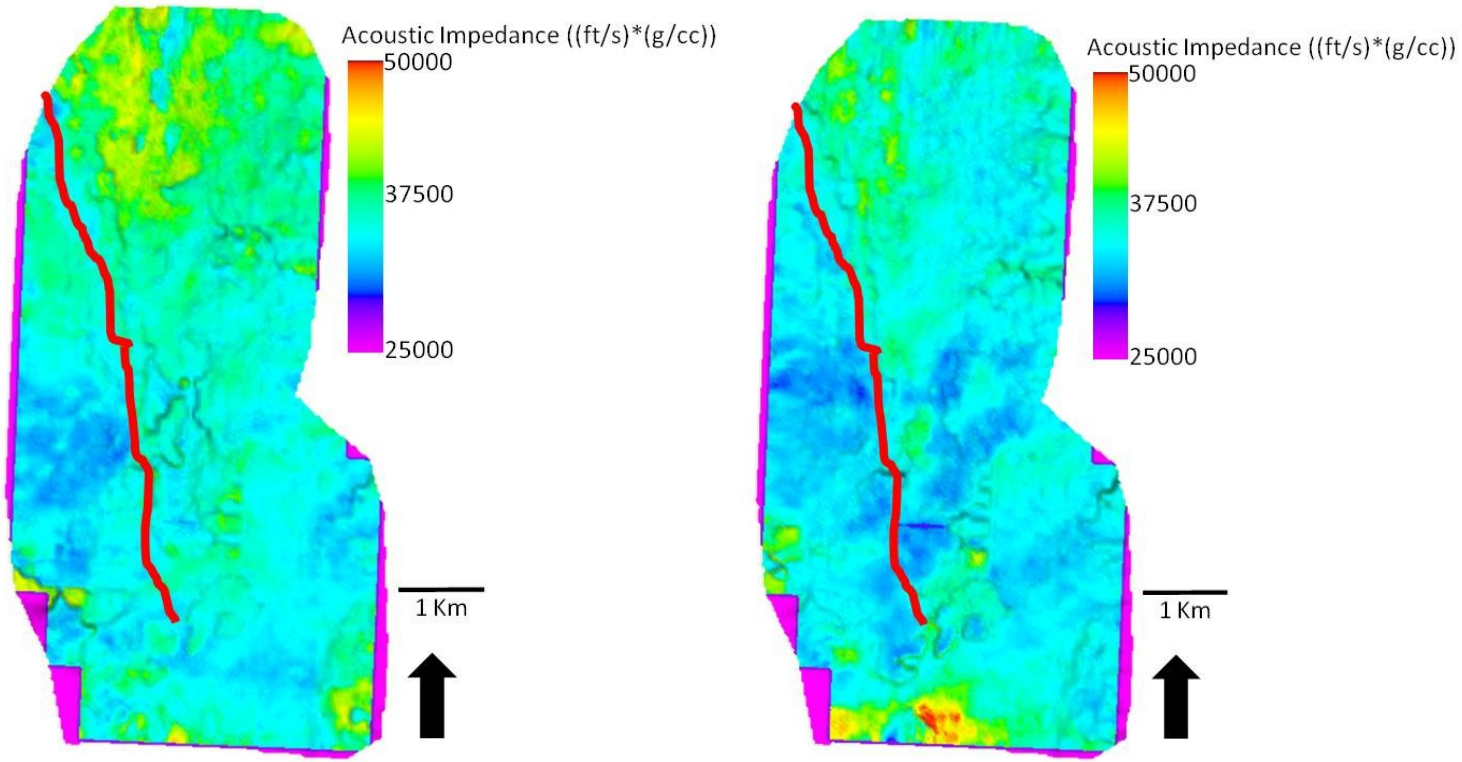

Figure 5.3 Stratal slice through to the acoustic impedance at (a) 60 % and (b) 20% of the time thickness between the top and the bottom of the Granite Wash horizons.

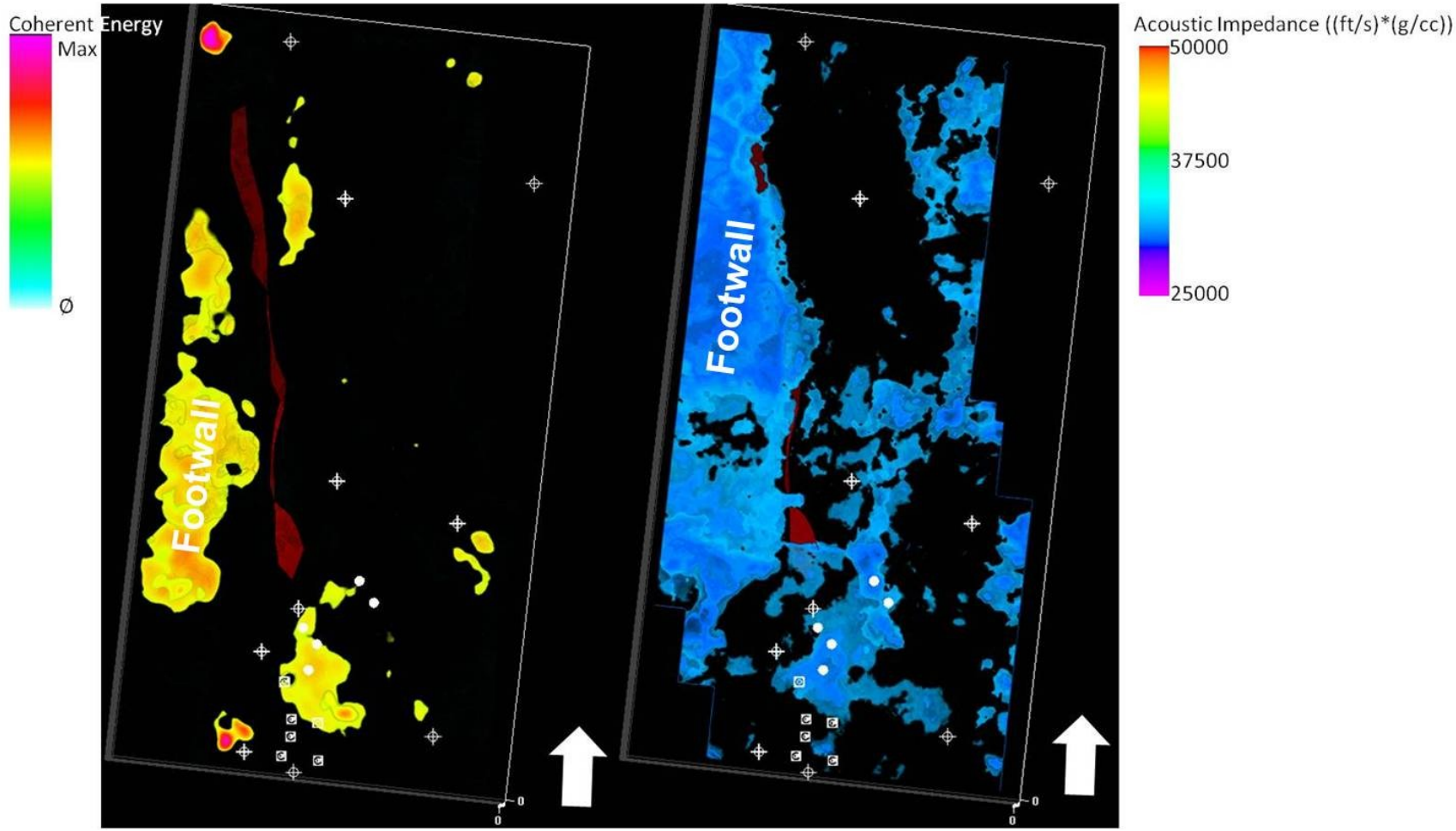

Figure 5.4 Geobodies through (a) coherent energy volume, (b) acoustic impedance volume.

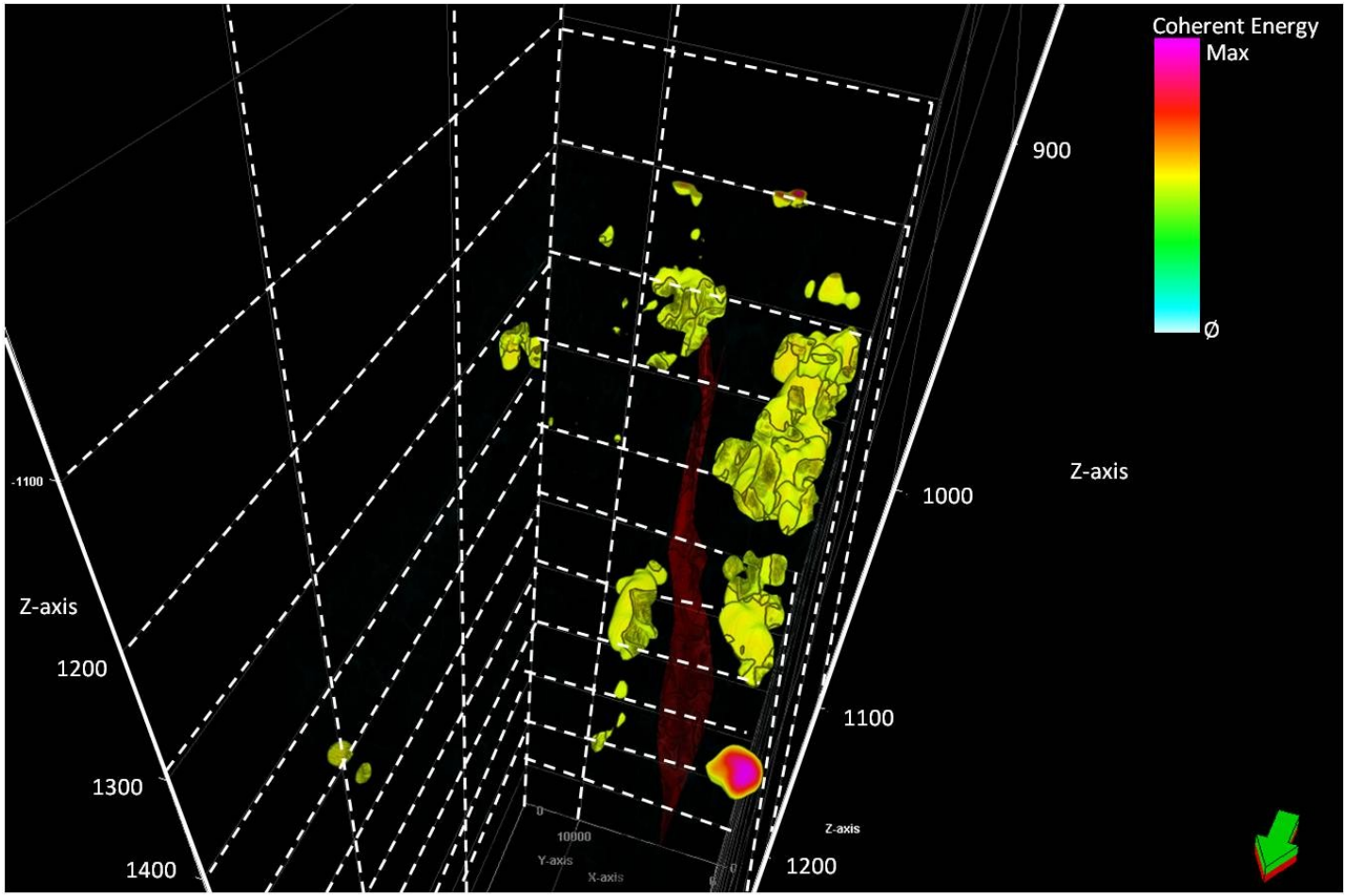

Figure 5.5 Geobodies through the coherent energy volume

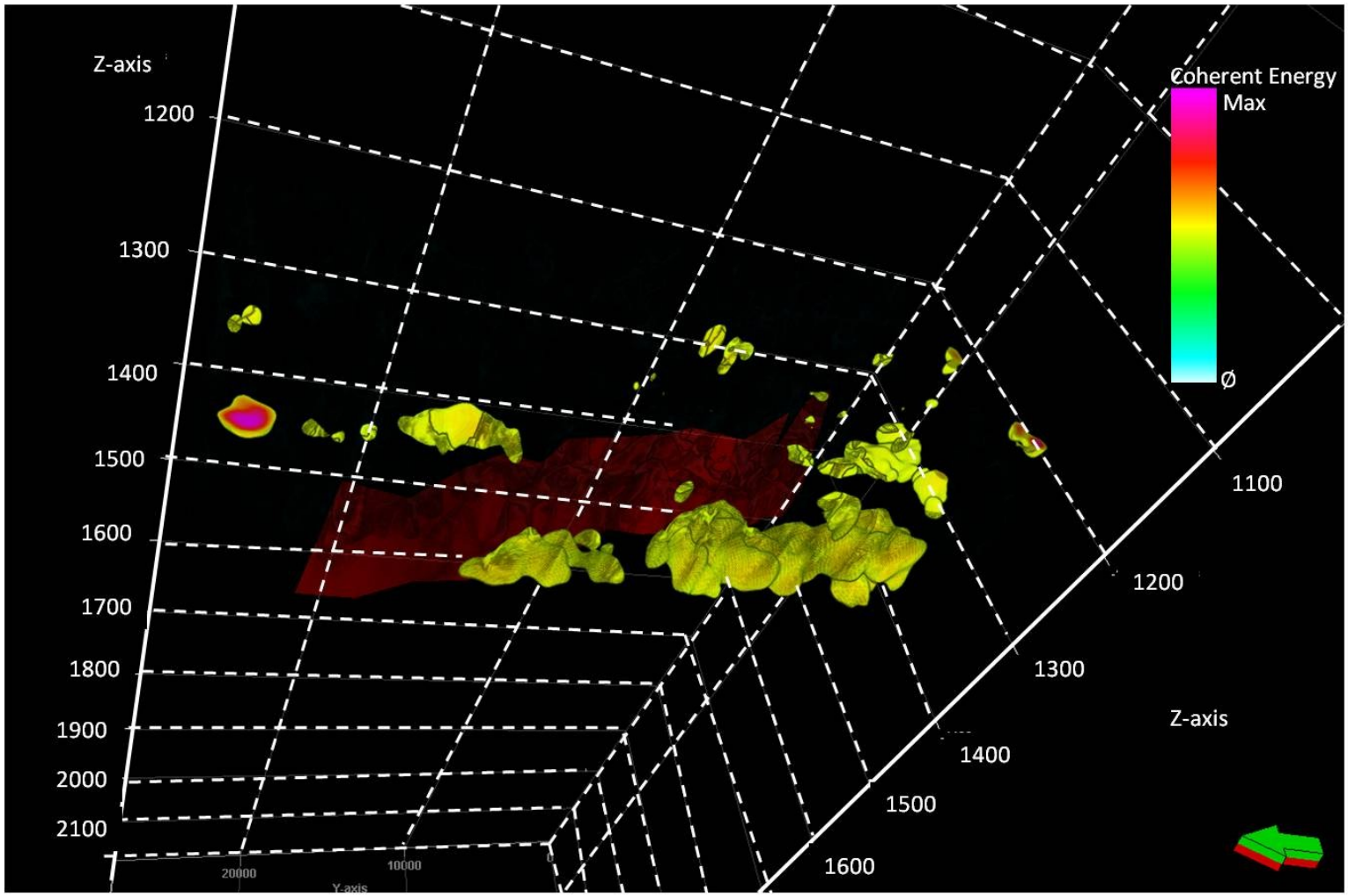

Figure 5.6 Geobodies through the coherent energy volume

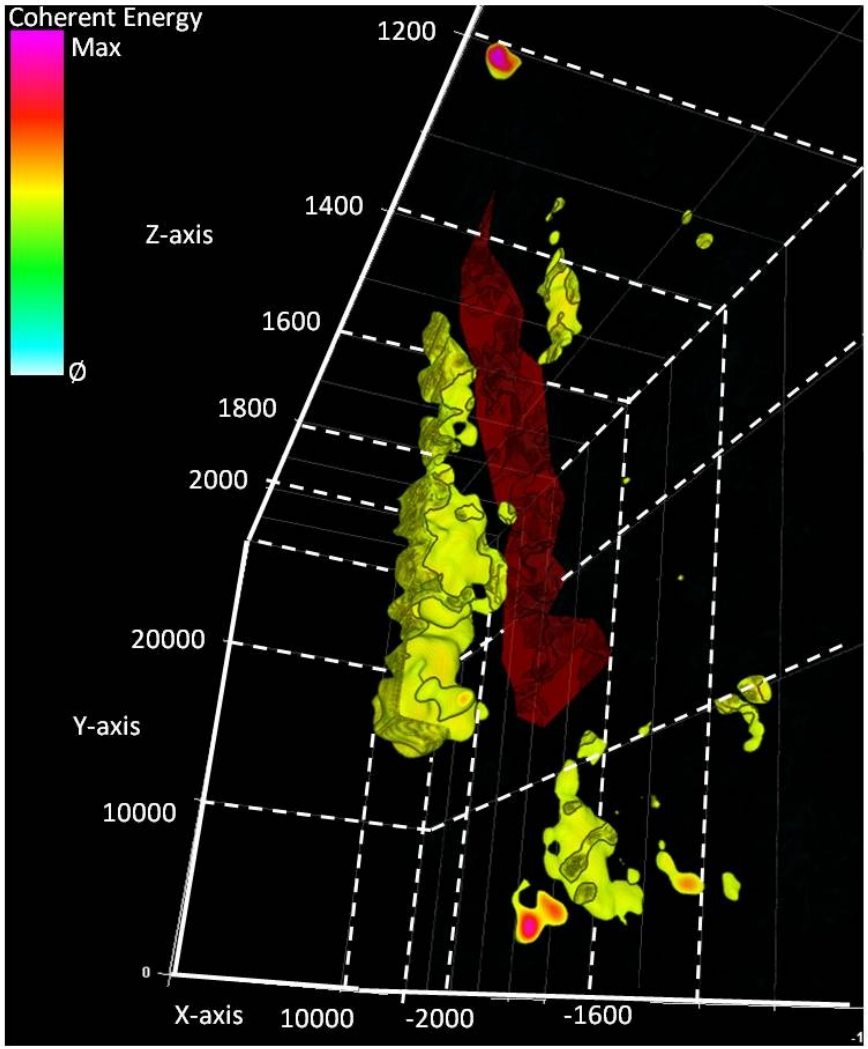

Figure 5.7 Geobodies through the coherent energy volume

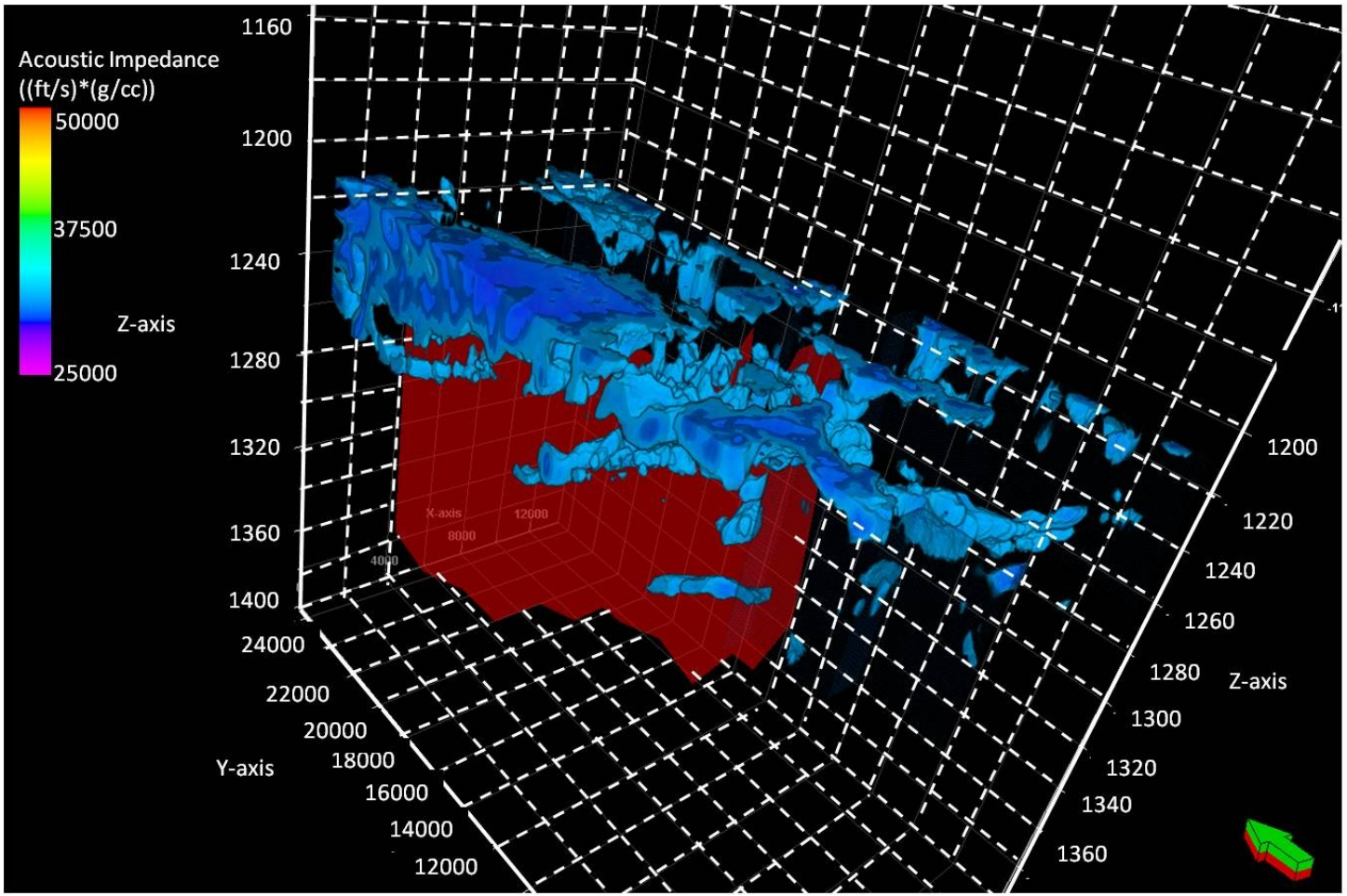

Figure 5.8 Geobodies through the acoustic impedance

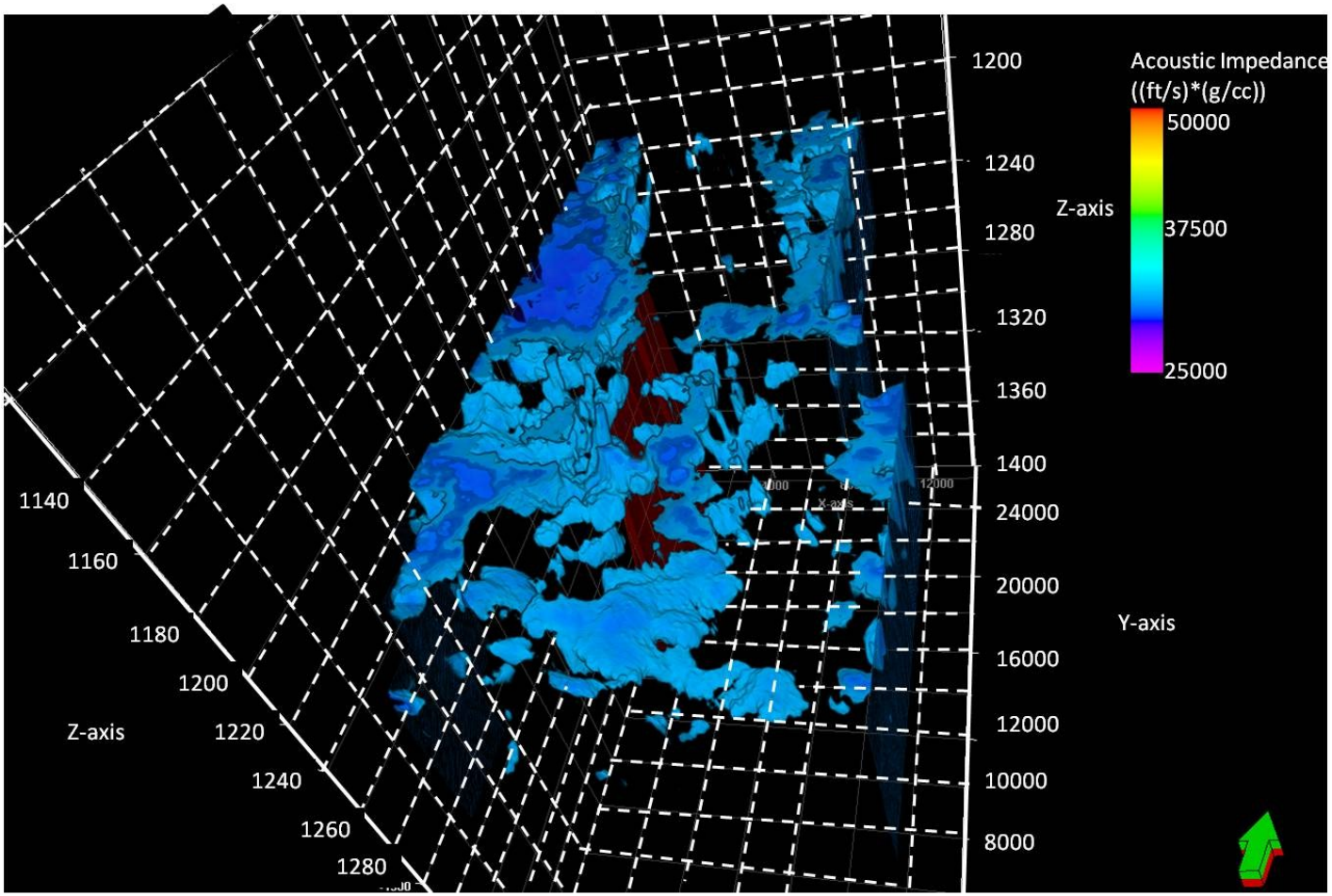

Figure 5.9 Geobodies through the acoustic impedance

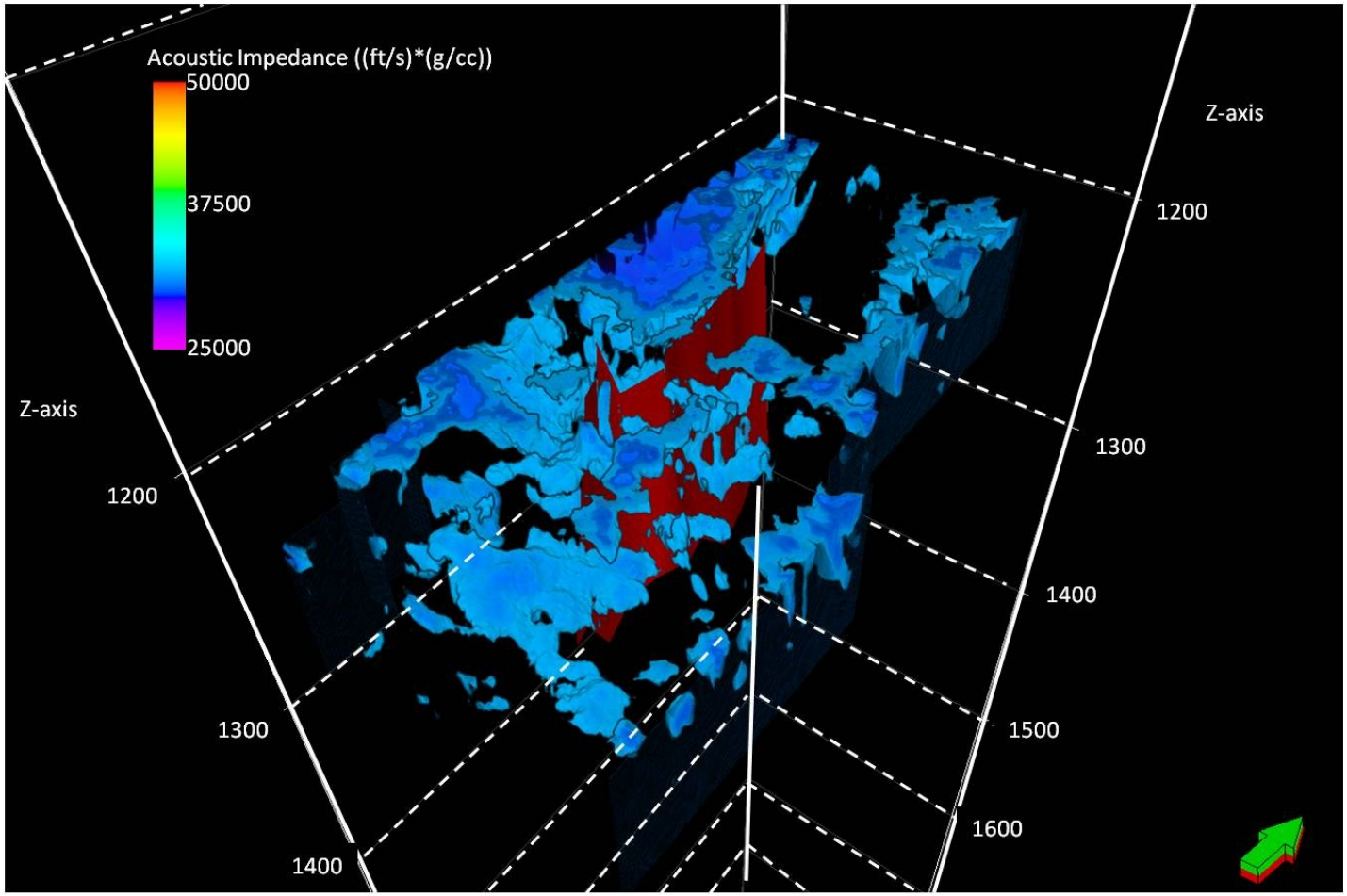

Figure 5.10 Geobodies through the acoustic impedance

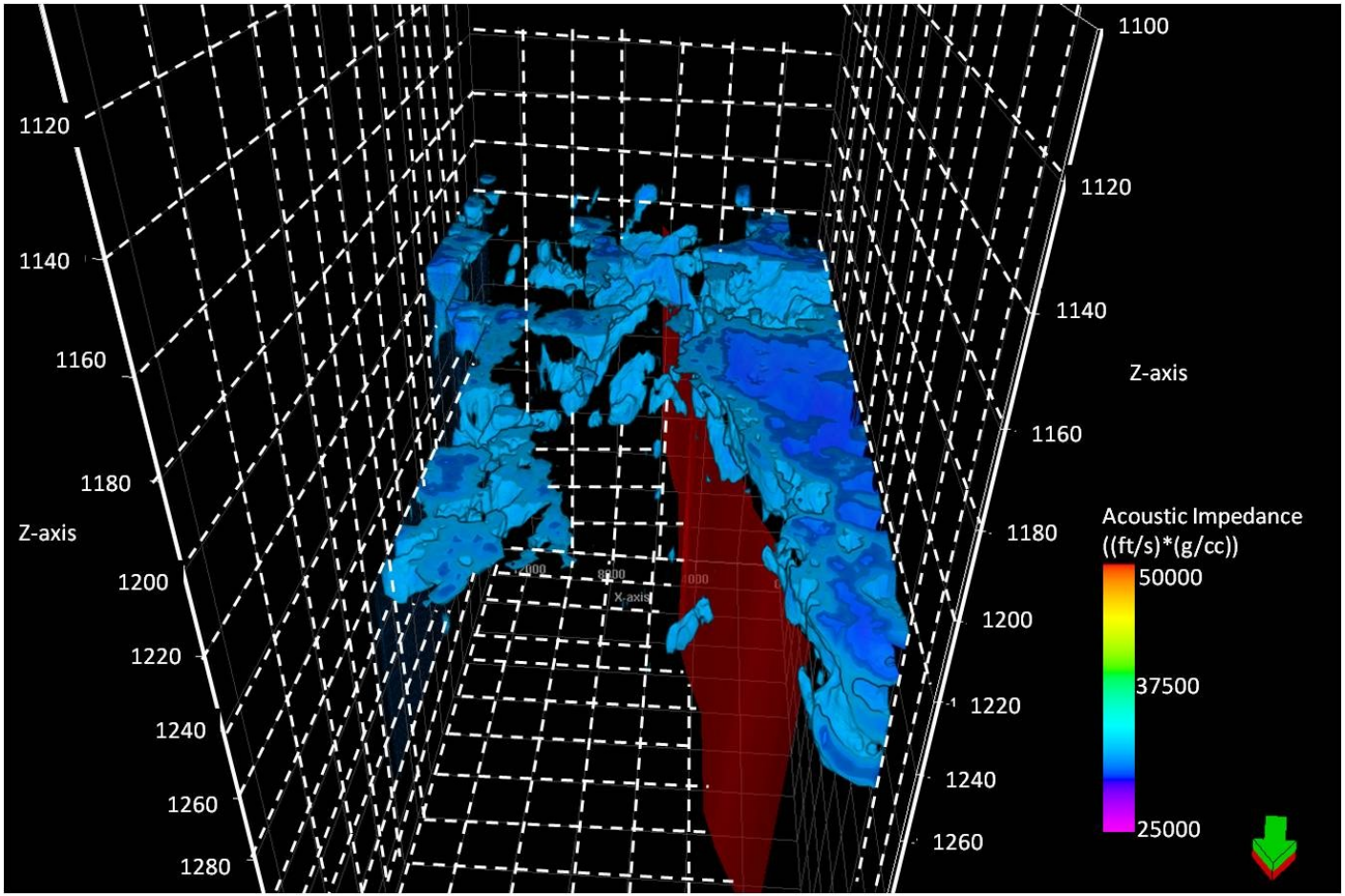

Figure 5.11 Geobodies through the acoustic impedance

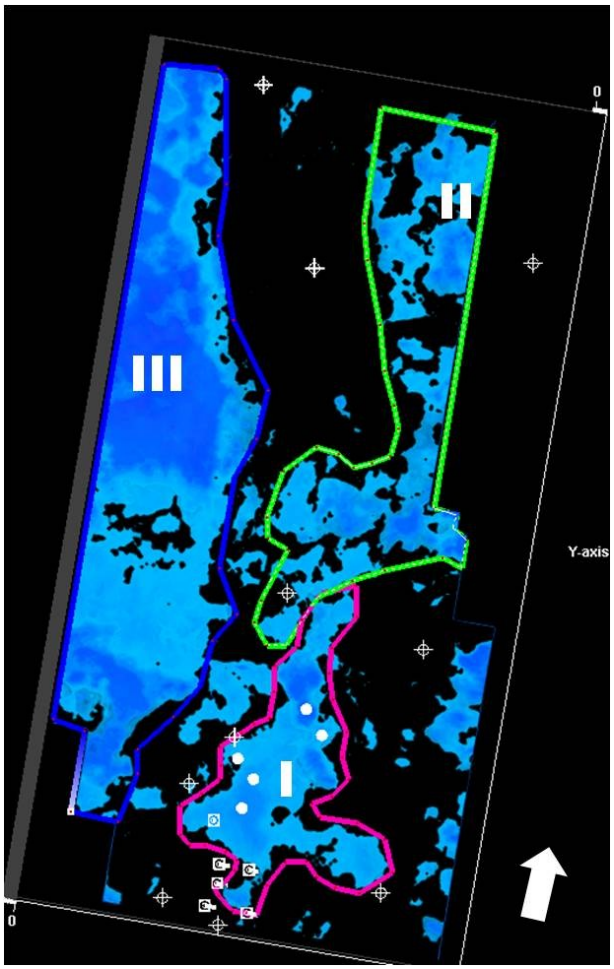

Figure 5.12 Prospect in the study area base on the geobodies through the acoustic impedance

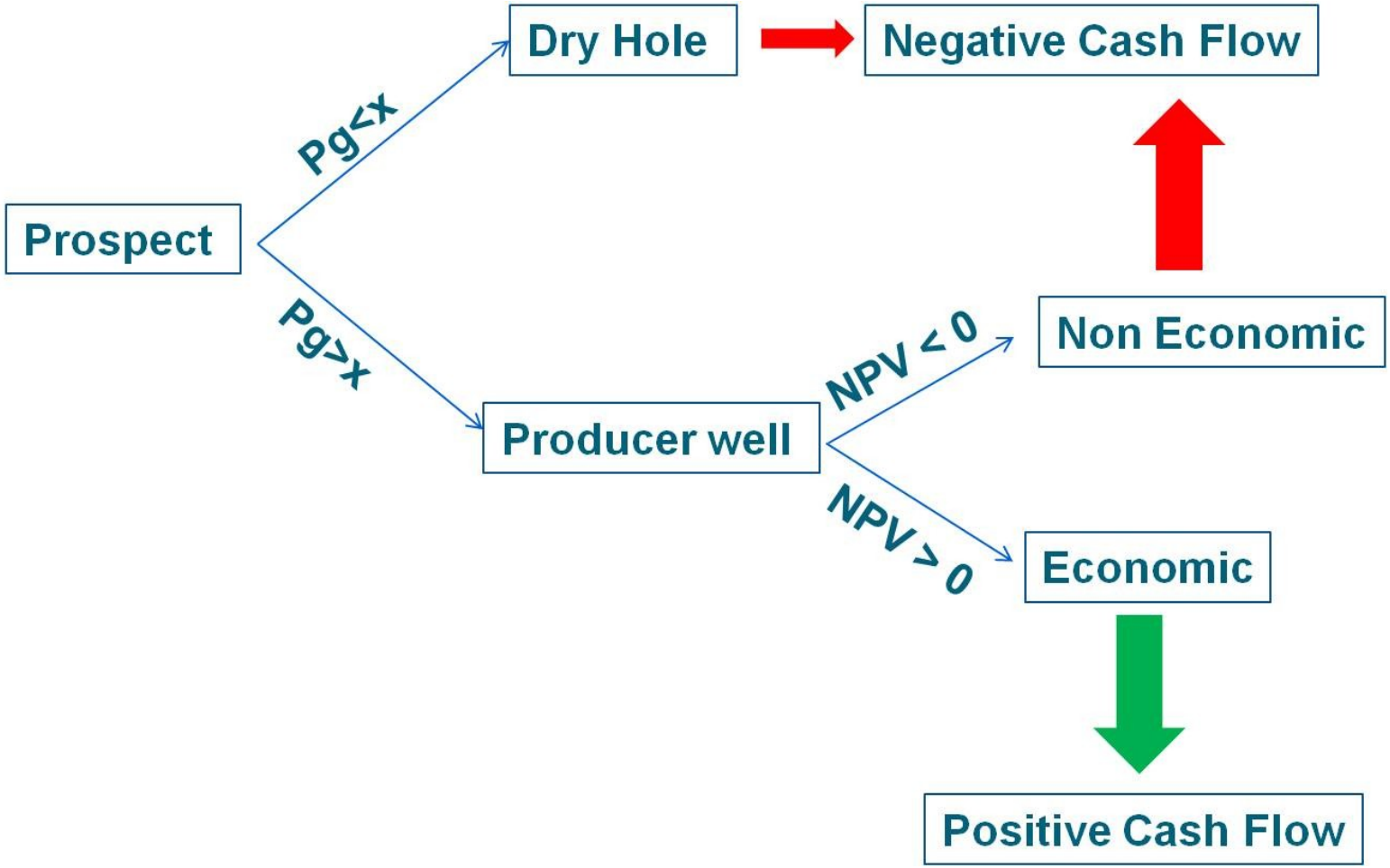

Figure 5.13. Workflow of risk analysis

CHAPTER VI

CONCLUSIONS

Data quality is the base of seismic interpretation; footprint removal is the first step in any seismic interpretation project. The resulting data set is improved and based on this new data set, the seismic attributes can be run. My time-structure map shows a structural high trending north-south, which represents the nose with separates the Dalhart basin from the Whittenburg Trough. In this area, some Granite Wash sediments are present which were transported from the south-west to the north-east and deposited as fan deltas.

At the top of the Brown Dolomite no faults are evident, but there are two structural highs located north and south of the study area. Also a sinuous channel with a south to north deposition direction can be recognized in this time-structure map. The use of a variety of attributes over the Boomer Sooner survey makes it possible to better define the main thrust fault, which is cuts both the Granite Wash interval and the basement. The fan deposit present in the Granite Wash interval was better identified with multi-attributes.

The producer wells are located in the low acoustic impedance areas and the dry wells are located in the high acoustic impedance zones. Based on this analysis, the low acoustic impedance can be associated with either higher porosity or hydrocarbon vs water saturation.

The acoustic impedance is low in the footwall of fault #1, indicating the possible presence of reservoir rock and the presence of oil.

REFERENCES

Asquith, G. and Cramer, S., 1975, Tranverse braid bars in the upper Triassic Trujillo sandstone in Texas panhandle: Jour. Geol., **83**. 657-651.

Bangrang, D., X. Xiucang and W. Jianxin, 2008, Wide/narrow azimuth acquisition footprints and their effects on seismic imaging: Petroleum Science, **5**, 308-313.

Birsa, D., 1977, Subsurface geology of the Palo Duro basin, Texas Panhandle: University of Texas PhD Thesis.

Burnett, M., 2002, Stratigraphic adventures in the Granite Wash of Hartley County, Texas: A case of study: AAPG Bulletin, **85,** 1689-1696.

Chopra, S., and K. Marfurt, 2008. Seismic attributes for prospect identification and reservoir characterization: SEG Geological developments series, **11**.

Chopra, S., and K. Marfurt, 2007. Seismic attributes-A historical perspective: Geophysics, **70**, 3SO-28SO

Cunningham, B., 1961, Stratigraphy, Oklahoma-Texas Panhandles in oil and gas fields of Texas and Oklahoma Panhandles: Amarillo, Texas, Panhandle Geol. Soc., 45-60.

Drummond, J., A. Budd, and J. Ryan, 2000, Adapting to noisy 3D data –Attenuating the acquisition footprint: 70th Annual International Meeting, SEG, Expanded Abstract, 9-12.

Duncan, R., 1980, Subsurface geology of the Dalhart basin, Texas Panhandle: Texas Tech University M.S Thesis.

Dutton, S., 1982, Pennsylvanian fan-delta and carbonates deposition Mobeetie Field Texas: AAPG Bulletin, **66**, 389-407.

Dutton, S., 1984, Fan-Delta Granite Wash of the Texas panhandle: Oklahoma City Geological Society, Short Course, 1-44.

Dutton, S and A. Goldstein, 1989, Palo Duro, Hardemen and Dalhart Basins: Geological Survey. Special publication, **89-2**. 35-40.

Eddleman, M., 1961, Tectonics and geologic history of the Texas and Oklahoma Panhandles, in oil and gas fields of the Texas and Oklahoma Panhandles: Amarillo, Texas, Panhandle Geol.Soc. 61-68.

Falconer, S. and K. Marfurt. 2008,Attribute-driven footprint suppresion: SEG Annual Meeting, 2667-2671.

Frost, E.,T. Allen and W.H. Fertl. 1982, Formation evaluation in Granite Wash Reservoirs: World Oil, 121-129.

Gerhard, L., 2004. A New Look at an Old Petroleum Province: Kansas Geological Survey, Earth Science, **250**, 1-27

Hendrickson, W.J., P.W Smith, and R.J Woods, 2001, Regional correlation of mountain front "washes" and relationship to marine sediments of Anadarko Basin and shelf: Oklahoma Geological Survey Circular **104**, 71-80.

Jain, S., 1986, Suitable environments for inversion techniques: A model study: Journal of the Canadian Society of Exploration Geophysicists, **22**, 7-18.

Kluth, C. F., 1986, Plate tectonics of the ancestral Rocky Mountains, in Paleotectonics and sedimentation in the Rocky Mountain region, United States, *in* James A. Peterson, ed., AAPG Memoir, vo1.41, pp.353-369.

Latimer, R., Davison, R., and Riel, P., 2000, An interpreter's guide to understanding and working with seismic-derived acoustic impedance data: The Leading Edge, 242-256.

Lyday, J., 1985, Atokan (Pennsylvanian) Berlin Field: Genesis of recycled detrital dolomite reservoir, deep Anadarko Basin, Oklahoma: AAPG Bulletin, **69**, 1931-1949.

Luo, Y., W. G. Higgs, and W. S. Kowalik, 1996, Edge detection and stratigraphic analysis using 3-D seismic data: 66th Annual International Meeting, SEG, Expanded Abstract, 324-327.

Mitra, S., 2009, Course Notes: Structural Geology I: University of Oklahoma.

McKee, E. D., and E. J. Crosby, 1975, Paleotectonic investigations of the Pennsylvanian System in the United States, U. S. Geological Survey Professional Paper, Report: **P 0853**, 349 pp.

Marfurt, K., 2010, Course Notes: Seismic Quantitative Interpretation: University of Oklahoma.

Marfurt, K., R. Scheet and J.Sharp, 1998, Suppression of the acquisition footprint for seismic sequence attribute mapping. Geophysics. **63,** 1024-1035.

Nicholson, J., 1960, Geology of the Texas panhandle in aspects of the geology of Texas: Symposium: The University of Texas at Austin. Bureau of Economic Geology Publication **6017**, 51-54.

Oldenburg, D.W., T. Scheuer, and S. Levy, 1983, Recovery of the acoustic impedance from reflection seismograms: Geophysics, **48**, 1318-1337.

Poole, M. 2005, Depositional modeling and characterization of the Granite Wash, Wheeler County, Texas and Beckham County, Oklahoma: University of Oklahoma M.S. Thesis.

Rascoe, B. and F. Adler, 1984, Permo-Carboniferous Hydrocarbon Accumulations, Mid-Continent, U.S.A: AAPG Bulletin, **6**, 979-1000.

Roberts, A., 2001, Curvature attributes and their application to 3D interpreted horizons, First break, **19**, 85-99.

Russell, B., 1988, Introduction to seismic inversion methods: Course notes series, **2**, 172.

Russell, B., D. Hampson and B. Bankhead, 2006, An inversion primer: CSEG Recorder, Special Edition, 96-103.

Schenewerk, P., D. Sethi, and W. Fertl, 1980, Natural gamma ray spectral logging aids Granite wash reservoir evaluation: SPWLA. **21**. 1-23.

Taner, M., 2001, Seismic attributes, CSEG recorded. September issue. 49-56.

Valerio, C., 2006, Evaluation of spectral inversion and spectral decomposition methods: Pennsylvanian Granite Wash reservoir characterization case study, Texas: University of Oklahoma M.S. Thesis.

Walper, J., 1977, Paleozoic tectonics of the southern margin of North America: GCAGS Transactions, **27**, 230-241.

Zeng, H., M. M. Backus, K. T. Barrow and N. Tyler, 1998a, Stratal Slicing part I: Realistic 3-D seismic model: Geophysics, **63**, 502-513.

Zeng, H., S. C. Henry, and J. P. Riola, 1998b, Stratal Slicing part II: Real seismic data: Geophysics, **63**, 514-522.

APPENDIX A

Volumetric Dip and Azimuth

The geological description of a planar interface such as a formation top or internal bedding surface can be defined by its apparent dips θ_x and θ_y, or more commonly, by the surface's true dip, θ, and its strike, ψ. (Figure A.1) Apparent dip θ_x is the angle measured in the vertical (x,z) plane from the horizontal x-axis to the interface. Similarly, apparent dip θ_y is the angle measured in the vertical (y,z) plane from the horizontal y-axis to the interface. The strike, ψ, is the angle between north (y-axis) and the intersection between the reflector and the horizontal (x,y) plane. The true dip, θ, is always greater than or equal to apparent dips θ_x and θ_y and is the angle measured in a vertical plane perpendicular to the strike between the horizontal plane and the interface.

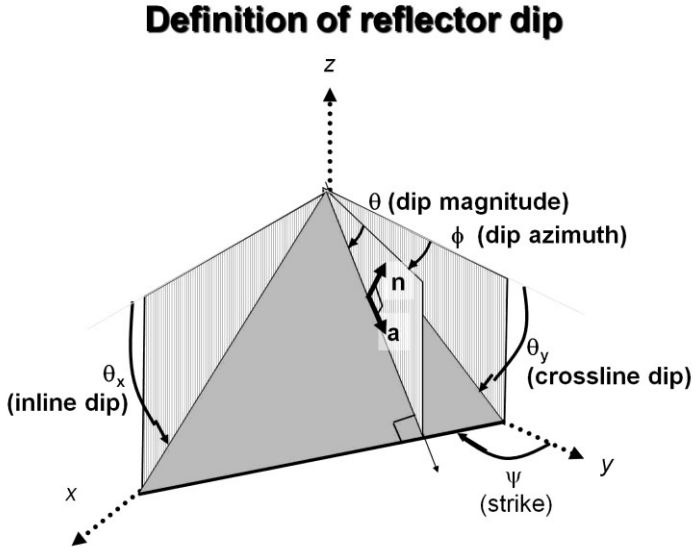

Figure A.1 Definition of reflector dip. (After Chopra and Marfurt, 2008)

In seismology, reflector dip is normally defined by dip magnitude, θ. Azimuth, ϕ, is measured from the north. Azimuth is perpendicular to the geologic strike and is measured in the direction of maximum downward dip. There are three methods of estimating volumetric dip and azimuth from uniterpreted seismic data volumes:

- Aligning the phase derived from complex trace analysis,
- discretely scanning for the most coherent planar reflector, or
- crosscorrelating the gradient of the data forming a gradient structure tensor, and computing the first eigenvector. (Chopra and Marfurt, 2008)

Coherence

Coherence is a measure of similarity between waveforms or traces. When seen on a processed section, the seismic waveform approximates the seismic wavelet convolved with the reflection coefficients corresponding to the geology of the subsurface. The coherence is commonly used to identify faults that are difficult to interpret on conventional seismic data. Stratigraphic features such as channel morphology, carbonate reefs, and in general any abrupt lateral change in geology will give rise to a lateral change of the waveforms which can be identified in the coherence volume.

There are several algorithms available to calculate coherence, but the ones used for this thesis are variance-based coherence and energy ratio coherence. The variance-based coherence was generated using commercial software, and a non dip-searching algorithm.

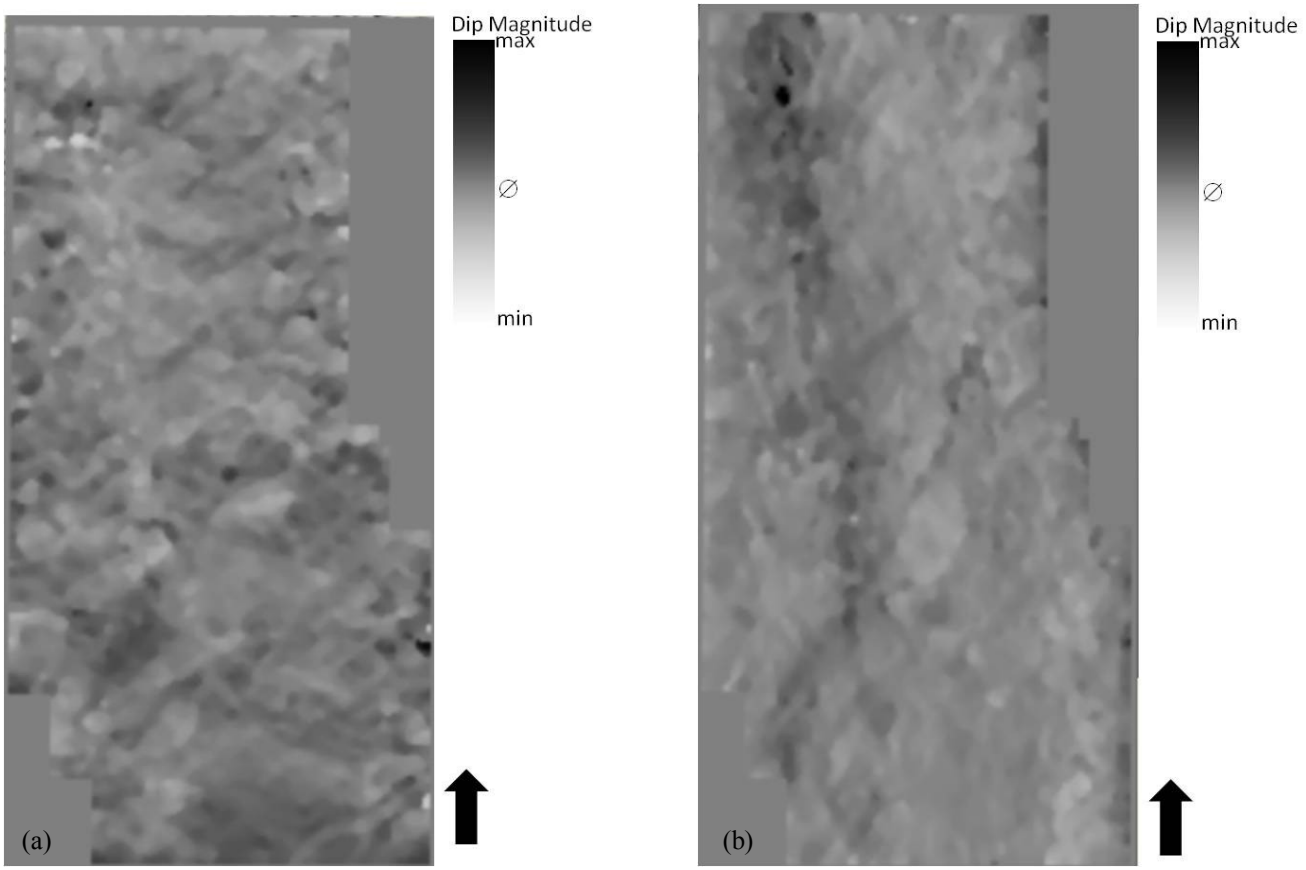

Figure A.2 (a) Crossline Dip and (b) Inline dip attributes at t=1200 ms.

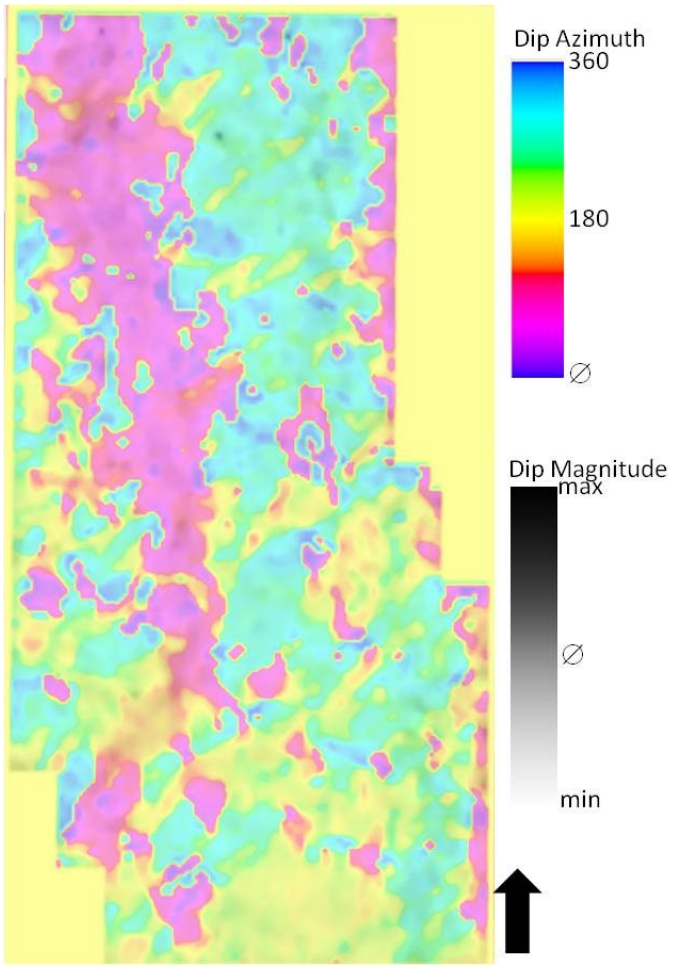

Figure A.3 Dip magnitude and dip azimuth attributes at t=1200 ms.

The energy ratio coherence was generated using an algorithm described by Marfurt, (2006). Variance- based coherence is closely related to the semblance-based coherence. The semblance-based coherence uses a calculation of a specific range of possible dips and azimuth. Amplitudes are collected from a trial horizon having a constant dip and azimuth. Semblance is calculated in a window for each trial horizon scanned within the user-specified range of dip and azimuth. In effect, semblance calculates the ratio of energy of the average trace to the average energy of all traces. The variance-based algorithm will numerically coincide with one minus the semblance estimate of coherence. Figure A.4 shows a schematic diagram showing the steps used in semblance estimation of coherence.

The variance estimate of coherence is numerically identical to one minus the semblance estimate of coherence ($C_{vo} = 1 - C_s$). The variance is a measure of how well each trace fits the mean trace. If all traces are equal, the variance estimate of coherence is C_v, = 0.0, and the semblance estimate of coherence, C_s, = 1.0 (Chopra and Marfurt, 2008).

Coherent energy

The eigenstructure method graphically analyzes a window of traces and determines which wavelet best represents the waveform variability (Figure A.3). Then this wavelet is scaled to fit each input trace, providing the coherent component of the data within the analysis window. (Chopra and Marfurt. 2008)

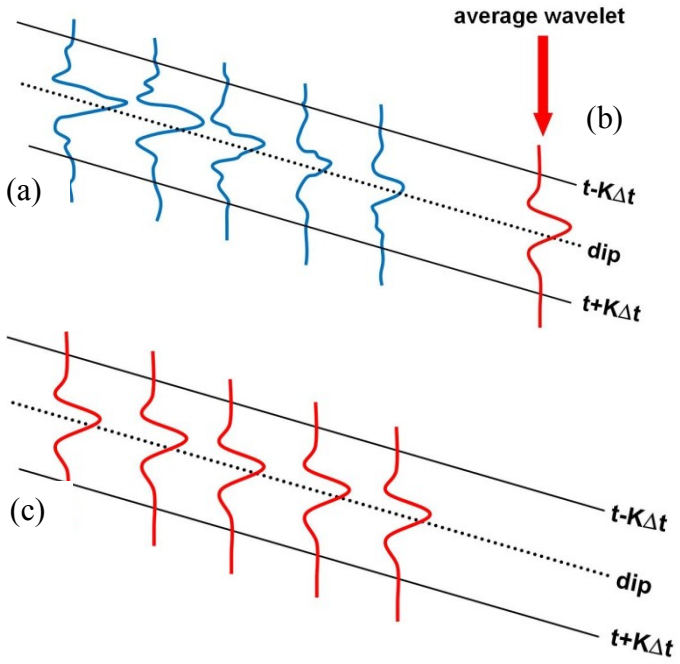

Figure A.4 Schematic diagram of semblance estimation of coherence. (a) Calculate the energy of the five input traces within an analysis window. (b) Compute the average trace. (c) Replace each trace by the average trace and calculate the energy of the five average traces. The semblance is the ratio of the energy of (c) to the energy of (a). (After Chopra and Marfurt, 2008)

The five points in Figure A.5 form the five elements of the principal component or eigenvector, $\mathbf{v}^{(1)}$. The coherent component of the data vector, $\mathbf{d}$, is the part correlated to $\mathbf{v}^{(1)}$: $\mathbf{d_{coh}} = (\mathbf{v}^{(1)} \bullet \mathbf{d})\, \mathbf{v}^{(1)}$. The coherent energy is then defined to be the sum of d^2_{coh} which is the Hilbert transform, $(d^4_{coh})^2$ within the analysis window. Mathematically, the coherent energy is equivalent to the first eigenvalue λ_1, corresponding to the first eigenvector, $\mathbf{v}^{(1)}$, representing the complex data within the analysis window.

In 3D each input trace falling within the analysis window gives rise to an element of the principal component vector, forming a small map v(x.y).

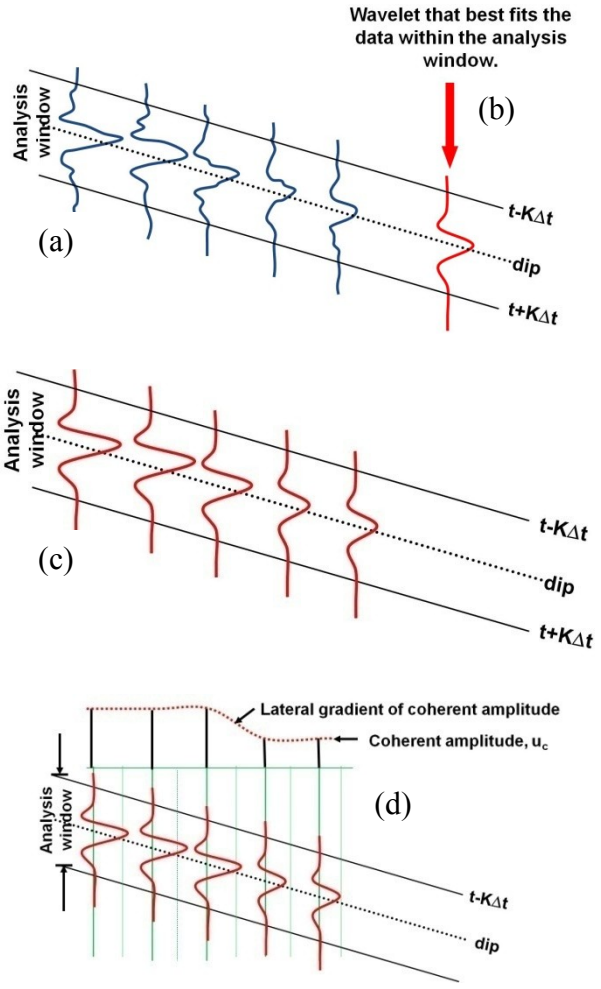

Figure A.5 Schematic diagram of eigenstructure estimation of coherence. (a) Compute the energy of the five input traces within an analysis window, $\mathbf{e_{tot}}$. (b) Estimate the coherent wavelet that when multipled by a constant, best fits the data within the analysis window. (c) Replace each trace with a scaled version of (b) that best fits the input trace. (d) Compute the energy of the coherent wavelet traces within the analysis window, giving rise to the coherent energy, $\mathbf{e_{coh}}$. The energy-ratio coherence is simply $c = \frac{e_{coh}}{e_{tot}}$ (Chopra and Marfurt, 2008)

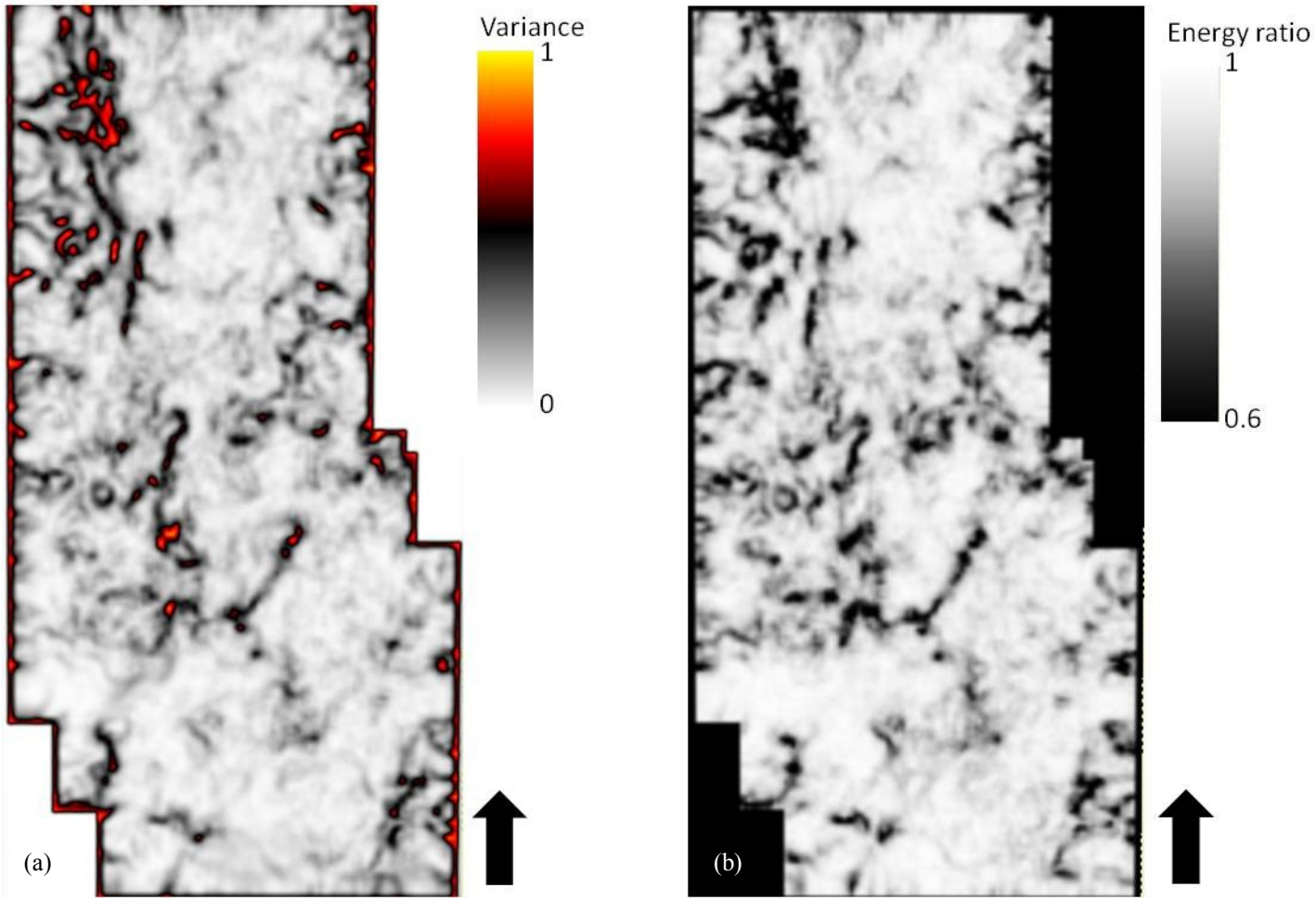

Figure A.6 (a) Variance and (b) Energy ratio coherence attributes at t=1200 ms.

Component Amplitude Gradient

The inline and crossline energy gradients are the horizontal derivatives along the structure of the coherent energy.

Figure A.7 shows the interpretation of the eigenvector, corresponding to a nine-trace analysis window, as the representation of a map of coherent amplitude, v(x,y). From this map the gradients $\frac{\partial v}{\partial x}(x,y)$ and $\frac{\partial v}{\partial y}(x,y)$, will indicate lateral changes in the coherent amplitude.

By construction, $\|v^{(1)}\| = 1$. If is therefore useful to weight these derivatives by the first eigenvalue, λ_1, giving rise to an energy-weighted amplitude gradient. (Chopra and Marfurt. 2008)

To minimize the effect of acquisition footprint, Marfurt (2006) use derivatives calculates along the x- and y-axes (inline and crossline directions) by using a derivative operator of the form

$$\frac{\partial v}{\partial x}(x,y) \approx \frac{2}{J-1}\sum_{j=2}^{J}\frac{x_j}{2r_j^2}v_j \qquad \frac{\partial v}{\partial y}(x,y) \approx \frac{2}{J-1}\sum_{j=2}^{J}\frac{x_j}{2r_j^2}v_j \qquad r_j = \left(x_j^2 + y_j^2\right)^{1/2} \quad \text{(A.1)}$$

where j is the number of traces in the analysis window.

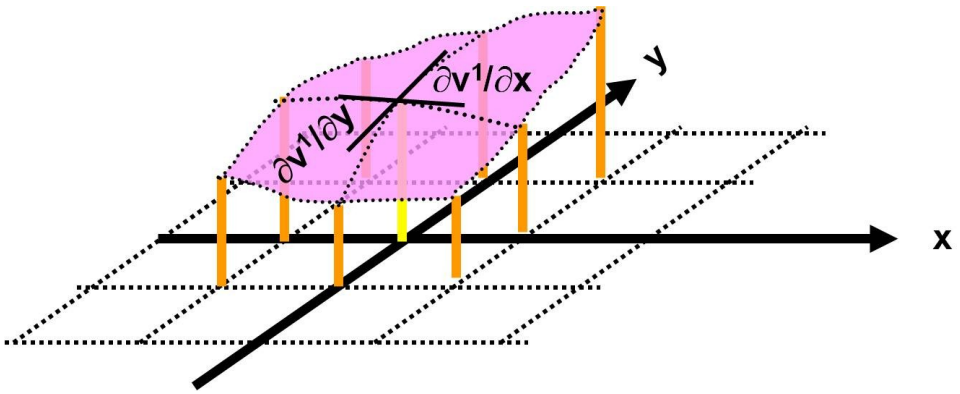

Figure A.7 Components of eigenvector, $\mathbf{v}^{(1)}$, describe the amplitude variation of the coherent wavelet along a local surface, *v(x,y)*. (After Chopra and Marfurt, 2008)

Curvature

The curvature in two dimensions is defined as the radius of a circle tangent to a curve. Anticlines have positive curvature and synclines have negative curvature. The linear portion of a curve has zero curvature. The curvature coefficient, *k*, is inversely proportional to the radius of curvature (Figure A.10).

Using least-square fitting or some other approximation method to fit a quadratic surface, z(x,y), to an interpreted horizon, the curvature can be determine from a grid of measurements:

$$z\,(x,y) = ax^2 + \ cxy + by^2 + dx + ey + f \qquad \text{(A.2)}$$

If the coefficient *c* in the equation A.2 is nonzero, the quadratic surface z(x,y) is rotated with respect to the principal axes. To find the maximum and minimum curvature,

k_{min} and k_{max}, the coordinates system need to be rotate to another frame, details of which can be found in Roberts (2001).

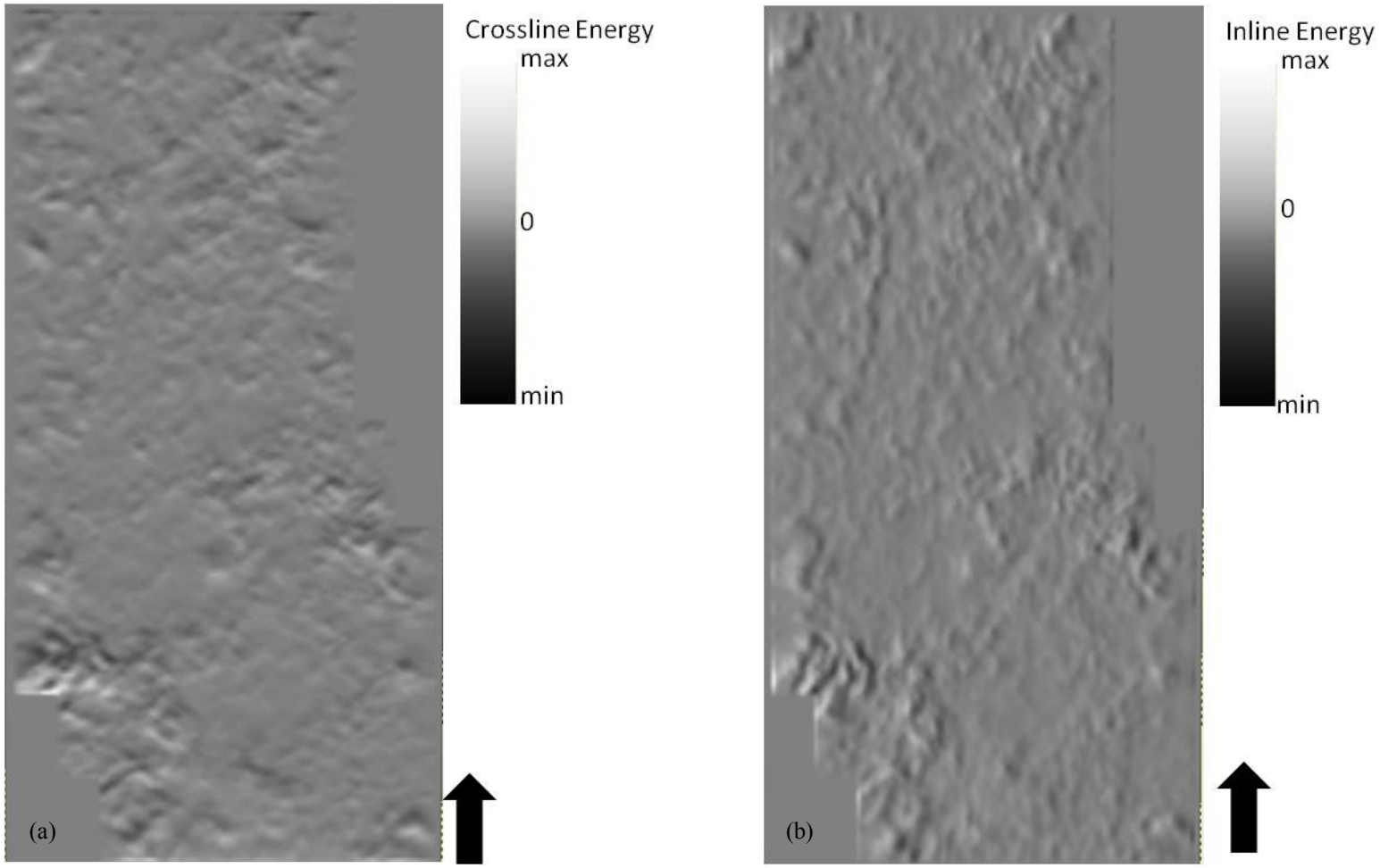

Figure A.8 (a) Crossline energy and (b) Inline energy attributes at t=1200 ms.

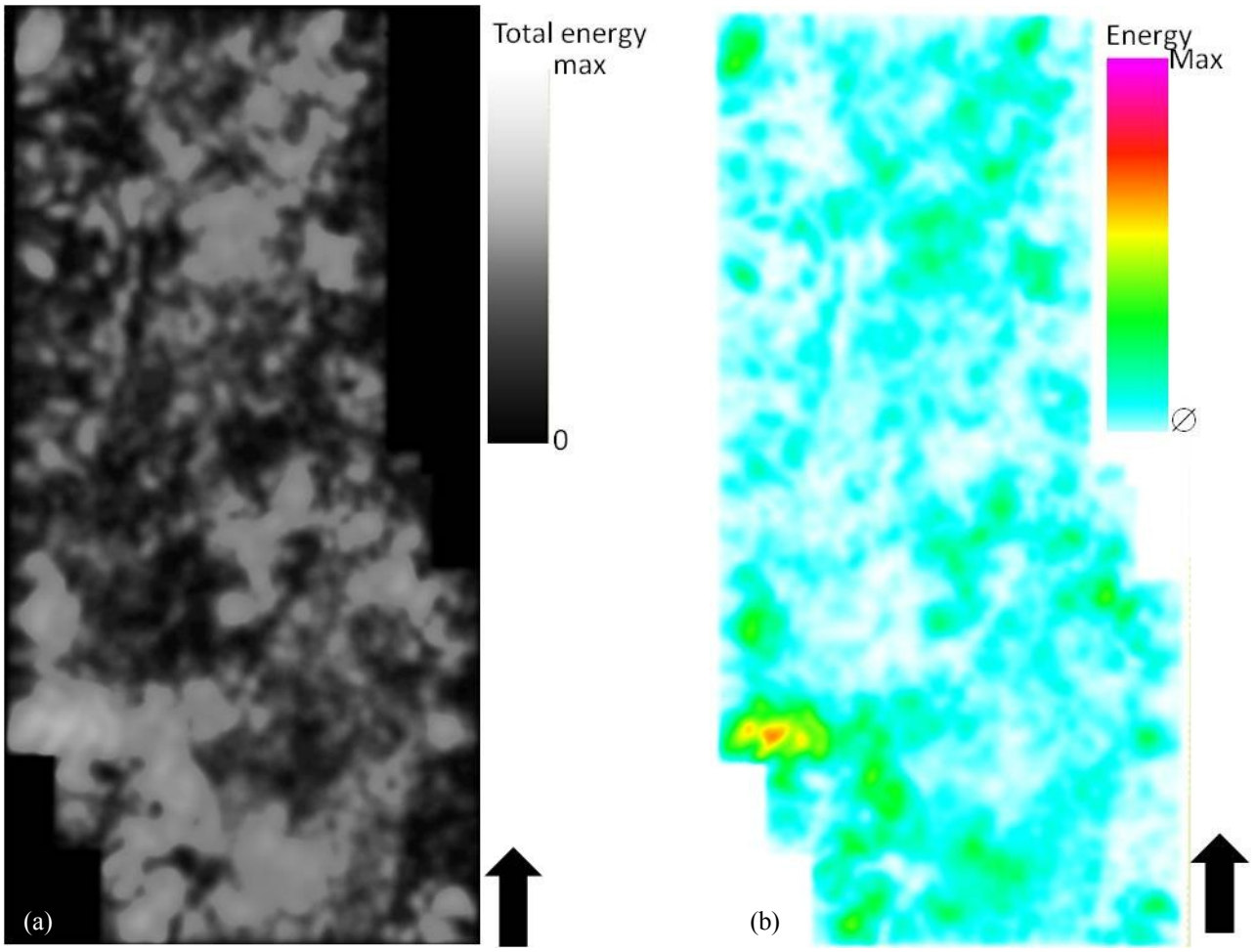

Figure A.9 (a) Total energy and (b) Coherent energy attributes at t=1200 ms.

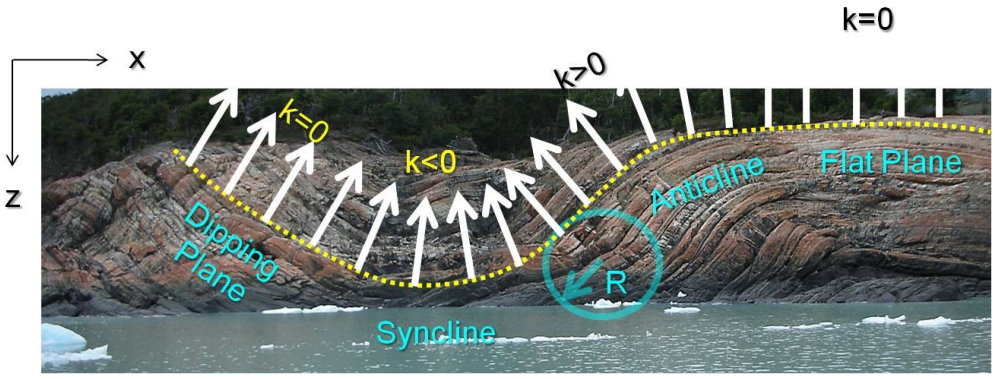

Figure A.10 Illustrated definition of 2D curvature. (Chopra and Marfurt, 2008)

Roberts (2001) defined that the mean curvature, k_{mean}, is:

$$k_{mean} = \frac{[a(1+e^2)+b(1+d^2)-cde]}{(1+e^2+d^2)^{3/2}} \qquad \text{(A.3)}$$

the Gaussian curvature, k_{Gauss}:

$$k_{Gauss} = \frac{(4ab-c^2)}{(1+d^2+e^2)^2} \qquad \text{(A.4)}$$

and the most-positive and most-negative principal curvatures:

$$k_1 = k_{mean} + (k_{mean}^2 - k_{Gauss})^{1/2} \qquad \text{(A.5a)}$$

$$k_2 = k_{mean} - (k_{mean}^2 - k_{Gauss})^{1/2} \qquad \text{(A.5b)}$$

The maximum and minimum curvatures, k_{max} and k_{min}, are related inversely proportional to the radius of curvature of the two orthogonal circles mentioned above and are related to the principal curvature by

$$k_{max} = \begin{cases} k_1 \; if \; |k_1| \geq |k_2| \\ k_2 \; if \; |k_1| < |k_2| \end{cases} \quad \text{(A.6a) and}$$

$$k_{min} = \begin{cases} k_2 \; if \; |k_1| \geq |k_2| \\ k_1 \; if \; |k_1| < |k_2| \end{cases} \quad \text{(A.6b)}$$

The maximum curvature is the principal curvature that has the larger absolute value, whereas the minimum curvature has the smaller absolute value. For this reason, the minimum curvature typically would define the variation in elevation along the long axis of a valley or ridge. The most-positive principal curvature can be a negative number and the most-negative principal curvature can be a positive number. (Chopra and Marfurt, 2008)

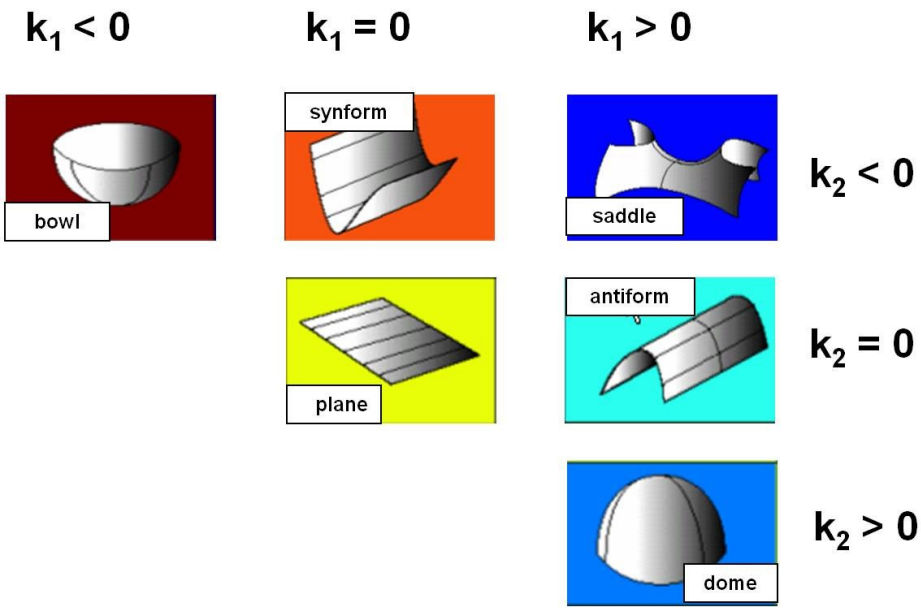

Figure A.11 Definition of 3D quadratic shapes expressed as a function of the most-positive and the most-negative principal curvatures, k_1 and k_2. (After Chopra and Marfurt, 2008)

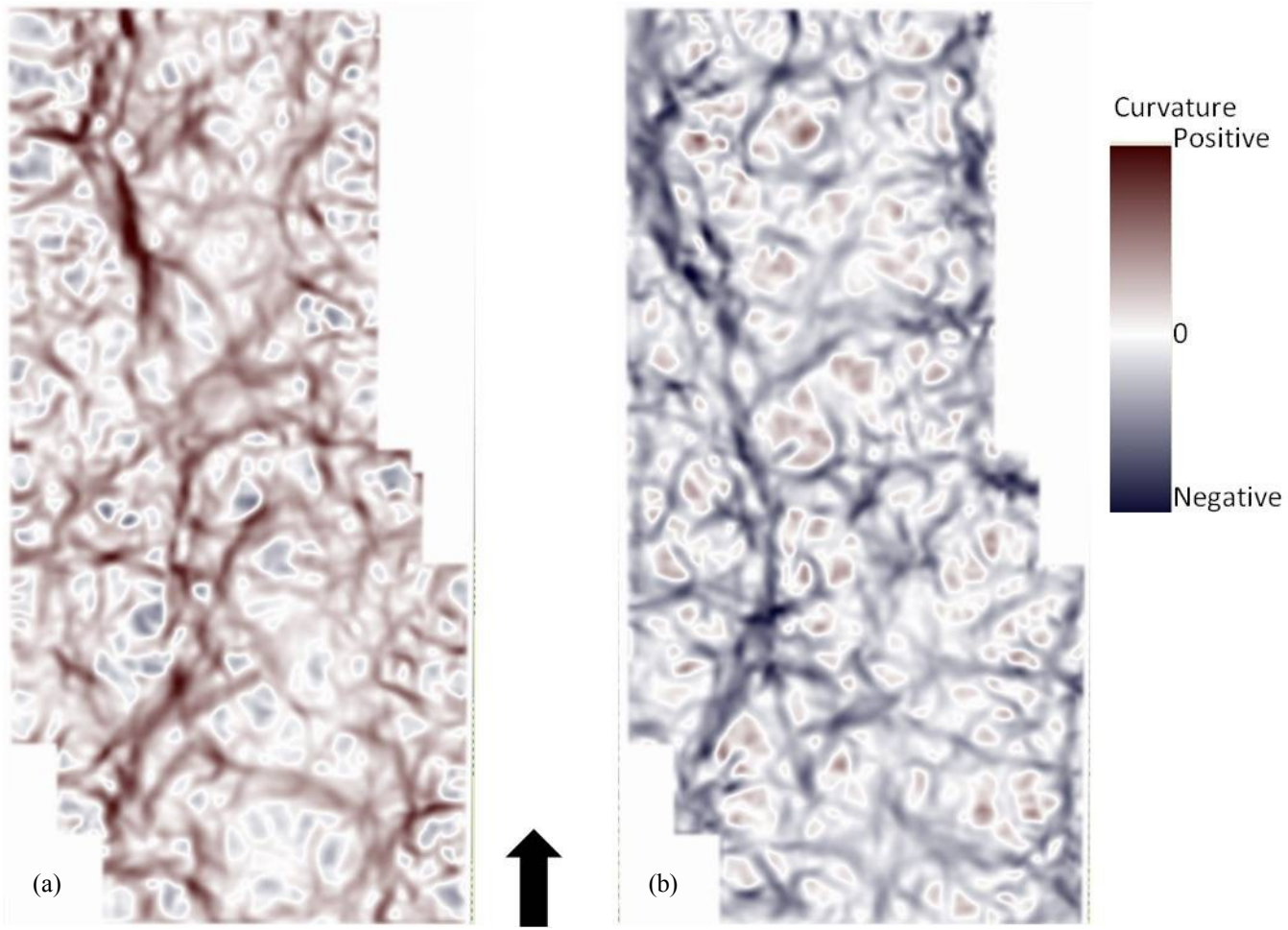

Figure A.12 (a) k_1 and (b) k_2 attributes at t=1200 ms.

Sobel Filter

The Sobel filter or L^2 norm of the spatial first-derivative operator, in a seismic time slice has the form: (Chopra and Marfurt, 2008)

$$e = \left\{\left[\frac{\partial u(t)}{\partial x}\right]^2 + \left[\frac{\partial u(t)}{\partial y}\right]^2\right\}^{\frac{1}{2}} = \left\{\left[\frac{u(t,x+\Delta x,y)-u(t,x-\Delta x,y)}{2\Delta x}\right]^2 + \left[\frac{u(t,x,y+\Delta y)-u(t,x,y-\Delta y)}{2\Delta y}\right]^2\right\}^{\frac{1}{2}} \quad (3.9)$$

The application of Sobel filter to seismic data was modified by Luo et al. (1996) converting it in a three steps process.

- Computes derivatives along a plane defined by the reflector dip and azimuth
- Stack those derivatives along a vertical analysis window to improve the signal-to-noise ratio, and
- Normalize the result, dividing the differences by the energy of the input traces, such that we measure relative changes in amplitude rather than absolute changes

The original edge-detection algorithm of Luo et al. (1996) is:

$$e(t,\tau_x,\tau_y) = \frac{\left(\sum_{k=-K}^{+K}\left\{[u_0(t+k\Delta t)-u_1(t+k\Delta t-\tau_x)]^2+[u_0(t+k\Delta t)-u_2(t+k\Delta t-\tau_y)]^2\right\}\right)^{1/2}}{\left(\sum_{k=-K}^{+K}\left\{2[u_0(t+k\Delta t)]^2+[u_1(t+k\Delta t-\tau_x)]^2+[u_2(t+k\Delta t-\tau_y)]^2\right\}\right)^{1/2}} \quad (3.10)$$

where:

- τ_x and τ_y are the delays associated with the reflector dip in the inline direction, x, and the crossline direction, y, and

- u_o is the analysis trace, the next adjacent inline trace is u_1, and the next adjacent crossline trace is u_2

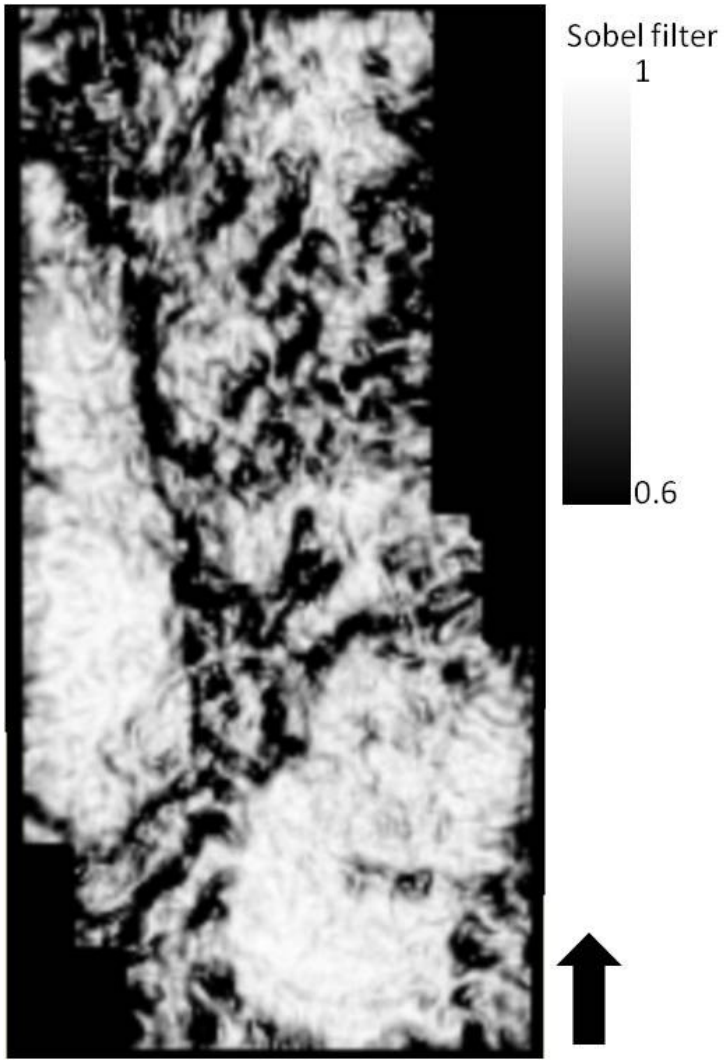

Figure A.13 Sobel filter attributes at t=1200 ms.

APPENDIX B

Post Stack Seismic inversion

The post stacks seismic inversion methods are based on the assumption that the seismic trace can be modeled with the convolutional equation, which can be written

$$S_t = [r_t * w_t + n_t] \cdot a_t \quad \text{(B.1)}$$

where S_t = the seismic trace

r_t = the earth's reflectivity

w_t = the seismic wavelet

n_t = additive noise

a_t = amplitude scaling

* denotes convolution

· denotes multiplication

Equation (B.1) suggests that if we are able to remove or reduce the noise component, deconvolve the wavelet, and restore the original amplitudes, we would be left with the earth's normal incidence reflectivity, which is related to acoustic impedance by the equation (Russell, 1988)

$$Z_{t+1} = Z_t \left[\frac{1+r_t}{1-r_t}\right] \quad \text{(B.2)}$$

$$r_t = \left[\frac{Z_{t+1}-Z_t}{Z_{t+1}+Z_t}\right] \quad \text{(B.3)}$$

where $Z_t = \rho_t V_t$ = acoustic impedance of layer t,

ρ_t = density

V_t = compressional wave velocity,

r_t = reflection coefficient

and layer t overlies layer t+1

Acoustic impedance (AI) is the product of the rock density and P-wave velocity. This means that AI is a rock property and not an interface property. Acoustic impedance inversion is simply the transformation of seismic data into pseudo-acoustic impedance logs at every trace. Latimer et al. (2000) described some advantages of impedance data:

- A impedance model contains all the information in the seismic data without the complicating factors caused by wavelets and adds essential information from the log data;
- Acoustic impedance is closely related to lithology, porosity, pore fill, and others factors. It is common to find strong empirical relationships between AI and one or more of these properties;
- As a layer property, AI can make sequence stratigraphic analysis more straight forward;
- AI data support fast and accurate volume-based interpretation techniques, allowing for rapid delineation of target bodies; and
- Elastic Impedance captures AVO information and, in conjunction with AI, improves interpretation power and the ability to discriminate lithology and fluids.

There are several inversion methods available, including: recursive inversion, model-based inversion, sparse-spike inversion, as well as AVO-type inversion methods including Lambda-Mu-Rho (LMR), joint inversion, and elastic inversion.

Recursive Inversion Method

The basic equation used in the recursive inversion method is given by equation B.2, the reflection coefficient may be thought of as the response of the seismic wavelet to an acoustic impedance change within the earth, where acoustic impedance is defined as the product of compressional velocity and density. In the equation B.3 converting from acoustic impedance to reflectivity involves dividing the differences in the acoustic impedance by the sum of the acoustic impedance.

Also the reflectivity series can be obtained from depth to time conversion, by integrating the sonic log transit time, as is show in the figure B.3. (Russell, 1988)

Russell (1988) said that the one of the key problems in the recursive inversion methods of seismic data is the lost of low-frequency component. This component can be found in three different ways:

- From filtered sonic log,
- From seismic velocity analysis, and
- From a geological model.

The low-frequency component can be added to the high-frequency component by either adding reflectivity stage or the impedance stage. The interpreter is interesting in the seismic velocity rather than the acoustic impedance, using a relationship between acoustic impedance and velocity. (Russell, 2006)

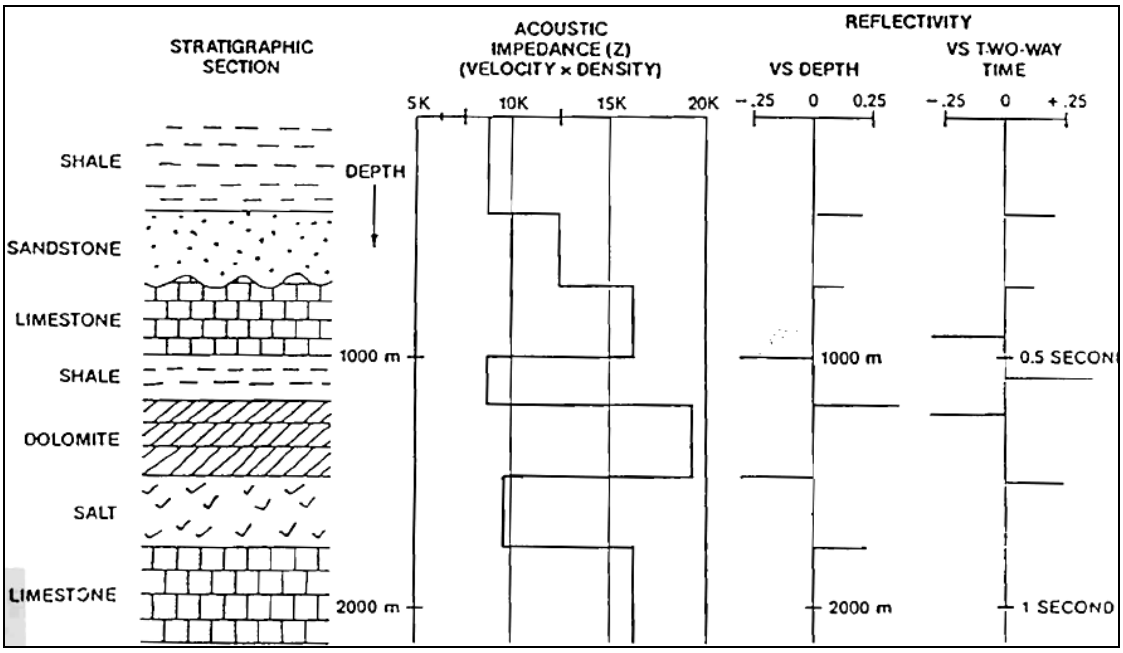

Figure B.1 Creation of reflectivity sequence. (Russell, 1988)

In summary, the recursive method of seismic inversion may be given by the following flowchart (Russell, 1988):

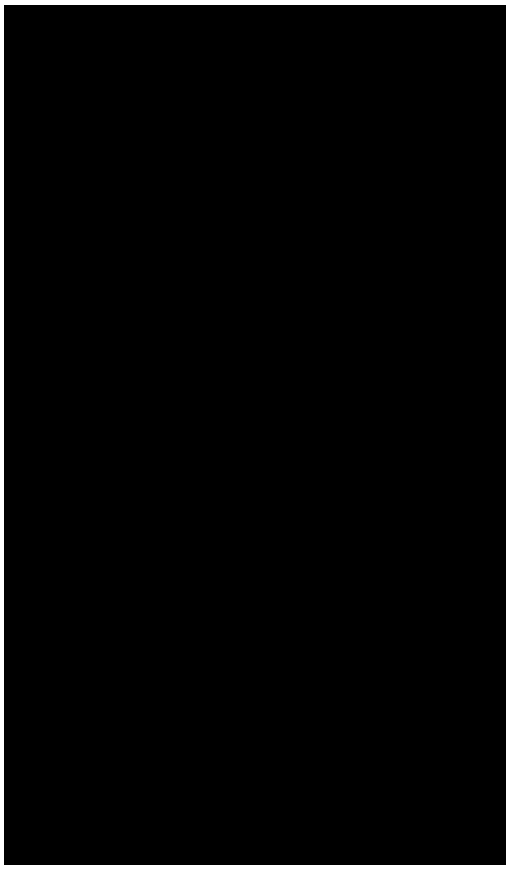

Figure B.2 Recursive inversion procedures. (Russell, 1988)

Sparse-Spike Inversion Method

The Sparse-Spike seismic inversion method is based in the equation B.1, normally the recursive method of seismic inversion is based on classical deconvolution techniques, which assume a random reflectivity and a minimum or zero-phase wavelet. This method produces a higher frequency wavelet on output, but never recovers reflection coefficients completely. (Russell, 1988)

In the Sparse-Spike method assume a certain model of the reflectivity and make a wavelet estimate based on this assumption. This technique includes:

- Maximum-Likelihood deconvolution and inversion
- L1 norm deconvolution and inversion

Maximum-Likelihood deconvolution and inversion

The fundamental assumption of Maximum-Likelihood deconvolution is that the Earth's reflectivity is composed of a series of large events superimposed on a Gaussian background of smaller events (Russell, 1988). We can derive an objective function which may be minimized to yield the "optimum" or most likely reflectivity and wavelet combination consistent with the statistical assumption.

With this objective function we are looking for the solution with the minimum number of spikes in its reflectivity and the lowest noise component. Essentially, we start with an initial wavelet estimate, estimate the sparse reflectivity, improve the wavelet and iterate through this sequence of steps until an acceptably low objective function is reached (Russell, 1988).

L1 norm deconvolution and inversion

Oldenburg et al. (1983) proposed using the L^1 norm criterion for minimization of the objective function instead of the least-squares or L^2 norm. The problem is solved using the frequency domain constraints and creating a sparse spike reflectivity estimate.

Simple constraints are usually provided in order to obtain a more accurate (and quicker) solution to the inversion. One such constraint is a range of values in which the impedance can vary laterally away from the well locations. A second constraint is the

location of the major horizons on the input data to provide solutions consistent with the conventionally picked horizon interpretation which form an a priori model. For this reason, the method is also referred to as constrained sparse-spike inversion. (Marfurt, 2010) The processing flow for the linear programming inversion method is show below.

Model-based Inversion Method

The model-based inversion method is based in the comparison between a geological model and the seismic data, then the results of this comparison between real and modeled data has to be used to iteratively update the model in such a way of the better match the seismic data. The basic idea of this approach is show in the figure B.3

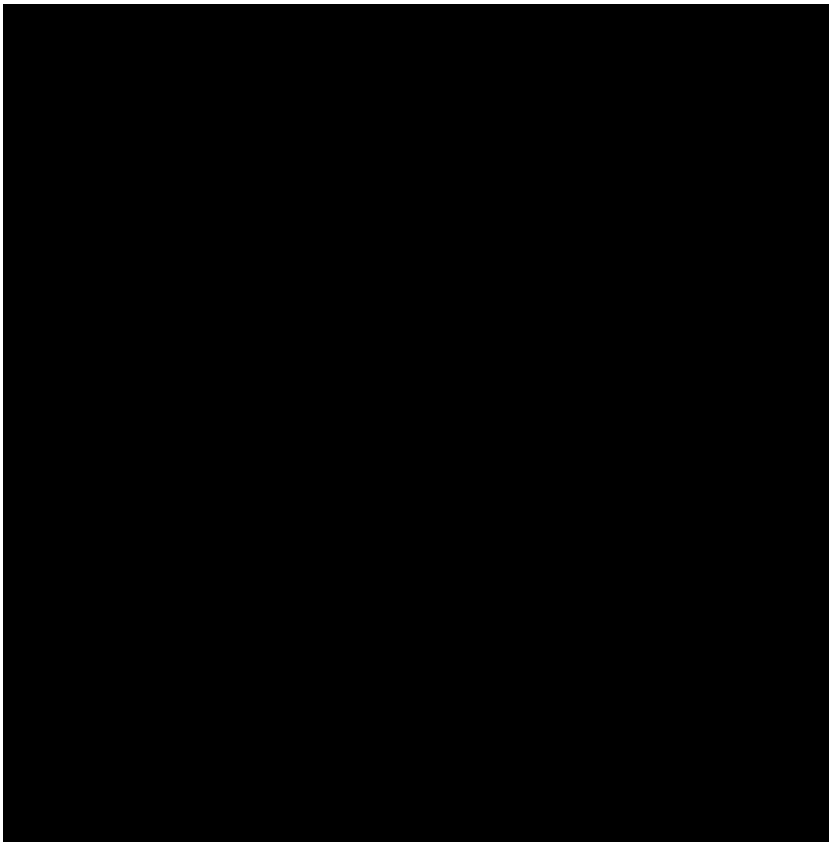

Figure B.3 Flowchart for the model based inversion technique. (Russell, 1988)